

# An exciting approach to theoretical spectroscopy

Martí Raya-Moreno<sup>1</sup>, Noah Alexy Dasch<sup>1</sup>, Nasrin Farahani<sup>1</sup>, Ignacio Gonzalez Oliva<sup>1</sup>, Andris Gulans<sup>2</sup>, Manoar Hossain<sup>3</sup>, Hannah Kleine<sup>1</sup>, Martin Kuban<sup>1</sup>, Sven Lubeck<sup>1</sup>, Benedikt Maurer<sup>1</sup>, Pasquale Pavone<sup>1</sup>, Fabian Peschel<sup>1</sup>, Daria Popova-Gorelova<sup>4</sup>, Lu Qiao<sup>1</sup>, Elias Richter<sup>1</sup>, Santiago Rigamonti<sup>1</sup>, Ronaldo Rodrigues Pela<sup>5</sup>, Kshitij Sinha<sup>1</sup>, Daniel T. Speckhard<sup>1</sup>, Sebastian Tillack<sup>1</sup>, Dmitry Tumakov<sup>1</sup>, Seokhyun Hong<sup>1</sup>, Jānis Užulis<sup>2</sup>, Mara Voiculescu<sup>1</sup>, Cecilia Vona<sup>1</sup>, Mao Yang<sup>1</sup>, and Claudia Draxl<sup>1,\*</sup>

<sup>1</sup> Department of Physics and CSMB, Humboldt-Universität zu Berlin, Zum Großen Windkanal 2, 12489 Berlin, Germany

<sup>2</sup> Department of Physics, University of Latvia, Jelgavas iela 3, Riga, LV-1004, Latvia

<sup>3</sup> Paderborn Center for Parallel Computing, Paderborn University, Warburger Str. 100, 33098 Paderborn, Germany

<sup>4</sup> Institute of Physics, Brandenburg University of Technology Cottbus–Senftenberg, Erich-Weinert-Straße 1, 03046 Cottbus, Germany

<sup>5</sup> Supercomputing Department, Zuse Institute Berlin (ZIB), Takustraße 7, 14195 Berlin, Germany

**Keywords:** *Density-functional theory, density-functional perturbation theory, theoretical spectroscopy, excited states, many-body perturbation theory, exciting code*

Theoretical spectroscopy, and more generally, electronic-structure theory, are powerful concepts for describing the complex many-body interactions in materials. They comprise a variety of methods that can capture all aspects, from ground-state properties to lattice excitations to different types of light-matter interaction, including time-resolved variants. Modern electronic-structure codes implement either a few or several of these methods. Among them, **exciting** is an all-electron full-potential package that has a very rich portfolio of all levels of theory, with a particular focus on excitations. It implements the linearized augmented planewave plus local orbital (LAPW+LO) basis, which is known as the gold standard for solving the Kohn-Sham equations of density-functional theory (DFT). Based on this, it also offers benchmark-quality results for a wide range of excited-state methods. In this review, we provide a comprehensive overview of the features implemented in **exciting** in recent years, accompanied by short summaries on the state of the art of the underlying methodologies. They comprise density-functional theory (DFT) and time-dependent density-functional theory (TDDFT), density-functional perturbation theory (DFPT) for phonons and electron-phonon coupling, many-body perturbation theory in terms of the *GW* approach and the Bethe-Salpeter equation (BSE). Moreover, we capture resonant inelastic x-ray scattering (RIXS), pump-probe spectroscopy as well as exciton-phonon coupling (EXPC). Finally, we cover workflows and a view on data and machine learning (ML). All aspects are demonstrated with examples for scientific relevant materials.

# 1 Introduction

Electronic and lattice excitations play a central role in a wide range of scientific and technological fields, from fundamental physics to applications in optoelectronics, energy harvesting, medical devices, and others. Understanding, predicting, and modeling these excitations are crucial not only for the discovery of new materials and the development of novel systems but also for enhancing the performance and functionality of existing ones. In this context, *ab initio* calculations are invaluable, offering a parameter-free and predictive framework to explore materials at the atomic scale. Among such approaches, DFT [1, 2] is the most widely used method, offering a good compromise between accuracy and computational cost. However, conventional DFT is intrinsically limited to ground-state properties. To describe excited-state properties, one can choose two different routes. The first, staying in the realm of DFT, is its time-dependent variant, time-dependent density-functional theory (TDDFT) [3–7]. The other is many-body perturbation theory (MBPT) with its Green-function-based methods [8–13]. Here, DFT typically serves as a starting point [14, 15]. For lattice excitations, density-functional perturbation theory (DFPT) is an efficient approach to provide phonon states and electron-phonon coupling parameters [16]. All these concepts together represent a rich portfolio that allows one to explore the huge space of materials and their properties and functions.

In this work, we review the current state of the field and discuss the implementation of the aforementioned methods using the full-potential code **exciting** as an illustrative example. The **exciting** code relies on the linearized augmented planewave plus local orbital (LAPW+LO) method, which is widely recognized as the gold standard in electronic-structure theory [17, 18]. Due to its all-electron nature, the code can be applied to all kinds of materials, irrespective of the atomic species involved and allows for exploring the physics of core electrons. Notably, we emphasize **exciting**'s high numerical precision, reaching the  $5 \mu E_h$  level [19]. As the name suggests, **exciting** has a particular focus on excitations. It implements all of the aforementioned formalisms, *i.e.*, DFT and TDDFT as well as MBPT in terms of variants of the *GW* approximations and the Bethe-Salpeter equation (BSE) [20–22]. For lattice excitations, it offers phonon calculations by means of DFPT and both the finite-displacement method and the frozen-phonon method use supercells. These methods can be used to tackle all kinds of spectroscopies, from optical to x-ray absorption, from infrared to Raman spectroscopy, from phonon to exciton dispersion, from electron-loss to pump-probe spectroscopy, and more. Overall, **exciting** has established itself as a benchmark tool for high-fidelity calculations and a source of reference data as well as the package with the widest portfolio of theoretical spectroscopy features.

The paper is organized into sections dedicated to the different methodologies. In each section, we first provide an overview of the current state of the art to contextualize the **exciting** developments within the international landscape. Subsequent subsections describe the latest developments and provide examples. Additional sections cover workflows and tools, data handling and machine learning, and more.

## 2 The exciting package

### 2.1 The linearized augmented planewave + local-orbital method

The **exciting** code is designed for the computation of excited-state properties of solids [20]. At its core, it is a highly precise all-electron ground-state framework based on the LAPW+LO method [17, 18]. It provides systematically controllable numerical solutions of the Kohn-Sham (KS) or generalized KS equations for periodic systems. The quality of the KS eigenvalues and wavefunctions obtained at this stage is critical, as they form the starting point for higher-level methods discussed later in this review. In the LAPW+LO method, the KS equations are solved without shape approximations to the KS potential, *i.e.*, without the use of pseudopotentials. The method combines a systematic path to basis-set completeness with an efficient all-electron representation of the KS wavefunctions, allowing for high precision at manageable computational cost. This balance is essential for large-scale high-throughput and excited-state calculations.

The central concept of the augmented planewave (APW) framework is the spatial partitioning of the unit cell into non-overlapping muffin-tin (MT) spheres, centered at the atomic positions  $\mathbf{R}_\alpha$  with radius  $R_{\text{MT}}^\alpha$ , and an interstitial region  $I$  [23]. This partitioning reflects the distinct physical character of the electronic states, which are rapidly varying close to atomic nuclei and smooth in the interstitial region, and it enables the construction of basis functions tailored to each region. The basis for the KS wavefunctions  $\psi_{n\mathbf{k}}(\mathbf{r})$ , labeled by band index  $n$  and Bloch wave vector  $\mathbf{k}$ , consists of APWs, which extend throughout the unit cell, and local orbitals (LOs), which are strictly confined to individual MT spheres,

$$\psi_{n\mathbf{k}}(\mathbf{r}) = \sum_{\mathbf{G}} c_{n\mathbf{G}}^{\mathbf{k}} \phi_{\mathbf{G}}^{\mathbf{k}}(\mathbf{r}) + \sum_{\mu} c_{n\mu}^{\mathbf{k}} \phi_{\mu}(\mathbf{r}). \quad (1)$$

Here,  $\mathbf{G}$  runs over reciprocal lattice vectors,  $\mu$  labels local orbitals, and  $c_{n\mathbf{G}}^{\mathbf{k}}$  and  $c_{n\mu}^{\mathbf{k}}$  denote the corresponding expansion coefficients of the KS wavefunction in the APW and LO basis, respectively.

#### Augmented planewaves and linearization

The basis functions used in the linearized augmented planewave (LAPW) framework are defined piecewise according to the spatial partitioning of the unit cell,

$$\phi_{\mathbf{G}}^{\mathbf{k}}(\mathbf{r}) = \begin{cases} \frac{1}{\sqrt{\Omega}} e^{i(\mathbf{G}+\mathbf{k}) \cdot \mathbf{r}}, & \mathbf{r} \in I, \\ \sum_{\ell m \xi} \mathcal{A}_{\ell m \alpha \xi}^{\mathbf{G}+\mathbf{k}} u_{\ell \alpha \xi}(r_\alpha; \epsilon_{\ell \alpha}) Y_{\ell m}(\hat{\mathbf{r}}_\alpha), & \mathbf{r} \in \text{MT}_\alpha, \end{cases} \quad (2)$$

where  $\Omega$  denotes the unit-cell volume and  $\mathbf{r}_\alpha = \mathbf{r} - \mathbf{R}_\alpha$  defines local coordinates with respect to the position of atom  $\alpha$  inside  $\text{MT}_\alpha$ . For valence electrons, the radial functions  $u_{\ell \alpha \xi}(r_\alpha; \epsilon_{\ell \alpha})$  are obtained by solving an effective one-electron radial problem in the spherically averaged KS potential  $v_0^\alpha(r)$ . The resulting solutions depend on the KS energy, which implies that the radial functions entering the basis are explicitly energy dependent. This explicit energy dependence of the radial functions, already present in the original APW formulation [23], renders the KS eigenvalue problem nonlinear. Within the LAPW framework, this difficulty is avoided by fixing reference energies  $\epsilon_{\ell \alpha}$ , resulting in a generalized linear eigenvalue problem. This approximation introduces a linearization error that increases with the deviation of the true eigenvalues from the chosen reference energies, making a fixed-energy APW basis insufficient for an accurate description over a wide energy range. This problem is fixed by enriching the radial part of the basis inside the MT spheres with energy derivatives of the radial functions (captured in Eq. (2) by the index  $\xi$ ) evaluated at the reference energies, such that each basis function satisfies the required matching conditions at the sphere boundary, which fix the coefficients  $\mathcal{A}_{\ell m \alpha \xi}^{\mathbf{G}+\mathbf{k}}$ . In the standard LAPW method, only a single additional radial component, corresponding to the first energy derivative, is used, together with two matching conditions that enforce continuity of the basis function and its radial derivative at

the sphere boundary. In `exciting`, the reference energies  $\epsilon_{\ell\alpha}$  are determined automatically from the initial potential following the Wigner-Seitz prescription [24], *i.e.*, placing them near the center of the energy window spanned by the corresponding states and avoiding material-specific tuning. This linearization strategy defines the variational basis used for the description of valence states within the LAPW framework.

For completeness, we note that core states are treated separately within the all-electron framework. Owing to their strong localization and energetic separation from the valence manifold, core states are obtained by solving the radial Dirac equation inside the MT spheres, using the respective spherically averaged KS potential. These states do not have contributions in the interstitial region and thus do not enter the variational basis expansion in Eq. (1), although they fully contribute to the self-consistent density and potential. Nevertheless, they are obtained from the same all-electron KS Hamiltonian as the valence states and are updated self-consistently in every iteration. They are also essential for core-level spectroscopies implemented in `exciting`.

### Local orbitals

LOs are basis functions that are strictly confined to a single MT sphere and vanish identically in the interstitial region [25, 26],

$$\phi_\mu(\mathbf{r}) = \begin{cases} \sum_\xi a_{\mu\xi} u_{\mu\xi}(r_\alpha; \epsilon_{\mu\xi}) Y_{\ell m}(\hat{\mathbf{r}}_\alpha), & \mathbf{r} \in \text{MT}_\alpha, \\ 0, & \mathbf{r} \in I. \end{cases} \quad (3)$$

They can be used for an alternative way of linearizing the eigenvalue problem, as realized in the augmented planewave plus local orbital (APW+LO) method. By adding LOs as additional basis functions, energy derivatives as introduced in the LAPW approach can be avoided, providing overall a more flexible basis. Moreover, this explicit construction of additional radial solutions at selected energies enables an accurate treatment of semi-core states as well as the systematic improvement of the description of high-energy and high-angular-momentum components that are essential for excited-state calculations. A sufficiently rich LO basis also permits the use of larger MT radii, which reduces the number of APWs required and thus improves computational efficiency. Since all of these variants can be realized within a single calculation, we use the generic expression LAPW+LO for the basis throughout this review unless explicitly addressing a particular aspect.

### Basis-set completeness

The LAPW+LO basis offers two technically distinct routes to systematic convergence. Increasing the number of APWs controls completeness in the interstitial region, while enriching the set of LOs improves completeness inside the MT spheres. This separation enables an internal consistency check of basis-set completeness. While the completeness of the APW basis can be assessed straightforwardly by increasing the planewave cutoff, the convergence of the LO basis is less transparent. LOs do not form a naturally ordered hierarchy, and their completeness cannot be inferred from a single scalar cutoff parameter. To assess the quality of the MT basis in a controlled manner, the LAPW+LO framework therefore employs a dual basis self-validation (DBSV) procedure.

The central idea of DBSV is to use a well-converged interstitial planewave basis as an internal reference. This procedure involves two otherwise identical calculations that differ only in the choice of MT radii. The resulting difference in the total energy per atom isolates the ability of the MT basis to reproduce the physics of a spatial region that is otherwise accurately described by planewaves. A small energy difference indicates that the MT basis is sufficiently complete and consistent with the converged interstitial reference. More details on the DBSV methodology and its use for basis assessment and construction will be published elsewhere [27].

## Automated and transferable basis-set selection

While the LAPW+LO basis provides a systematic route to numerical convergence, the practical construction of a basis set is often guided by user experience. In **exciting**, recent developments aim to replace these heuristic choices by a transferable and largely automated procedure. Users specify a desired numerical precision, and **exciting** determines consistent planewave cutoffs, MT radii, and compact LO sets automatically.

**Hierarchies of local orbitals from dual basis self-validation.** In Ref. [27], DBSV is used to construct hierarchies of local orbitals by quantifying their contribution to the completeness of the MT basis. This makes it possible to identify near-redundant functions and to build the smallest LO set required to reach a target precision without extensive manual convergence testing.

**Control of the APW completeness.** To control the number of APWs for a desired precision in a material-independent way, **exciting** introduces a numerical quality parameter derived from the conventional cut-off  $R_{\text{MT}}|\mathbf{G} + \mathbf{k}|_{\max}$ . Reference values of this parameter were tabulated for elemental solids, corresponding to a ground-state total-energy error of approximately 0.1 meV/atom with respect to an extrapolated complete-basis limit [28]. These values are used as species-dependent scaling factors, yielding a single parameter that controls APW basis precision in a transferable manner across different materials.

**Automatic and balanced choice of muffin-tin radii.** The same reference data are further exploited to automate the choice of MT sphere radii. For a given global planewave cutoff, individual radii are scaled such that different atomic species contribute to the overall basis-set error comparably. Combined with the DBSV-based LO hierarchies, this strategy provides a consistent, precision-driven basis specification suited for both ground-state calculations and the excited-state methods built on top of them.

## 2.2 **exciting's** portfolio

**Features.** As mentioned in the Introduction, **exciting** offers a rich variety of features, from KS DFT and gKS DFT and DFPT to TDDFT and to Green-function based approaches to obtain the quasiparticle (QP) bands all kinds of spectra. The most important features are summarized in Table 1, including the developments and implementations of the last years, which will be described in the following sections. These new developments concern all levels of methodology. On the DFT level, these are mGGA (Section 3.3), DFT-1/2 (Section 3.4), and hybrid functionals (Section 3.5). spin-orbit coupling (SOC) can be treated very efficiently, by a method, called second variation with local orbitals (SVLO) [29] (Section 3.6). This is not restricted to the ground state (GS), but has been extended to optical spectra (Section 6.4). Moreover, **exciting** covers implementations of constrained density-functional theory (cDFT) (Section 3.7), the newest version of Libxc [30, 31], and an interface to the SIRIUS library [32] (Section 9.4). Lattice vibrations and electron-phonon coupling (EPC) effects have been introduced to the code in many aspects. **exciting** now features an implementation of DFPT (Section 4.3), providing phonon properties, EPC coupling constants, and related self-energies that renormalize the electronic properties and give rise to temperature effects. Obtaining also Born effective charges, allows for treating vibrations of polar materials reliably. The *GW* module (Section 5) contains a rich variety of new features, which are the direct computation of the polarizability, improvements in the calculation of the correlation self-energy, a precise treatment of long-range interactions in anisotropic and/or low-dimensional systems, a task-based *GW* workflow with GPU porting, and an efficient evaluation of the screening of weakly-bound interfaces (Section 5.7). All above mentioned functionals are available as a starting point. Also, a QP self-consistent version has been implemented [33] (Section 5.6). On the spectroscopy side, **exciting** now covers besides linear response (LR)-TDDFT (Section 7.3) also real-time (RT)-TDDFT (Section 7.4), including Ehrenfest dynamics [34]. With a low-scaling implementation, the BSE code has experienced a dramatic speed-up [35] (Section 6.3) and can be used also for non-equilibrium cases. Based on this, resonant inelastic x-ray scattering (RIXS) [36, 37] (Section 6.6) and pump-probe spectra (Sections 8.2 and 8.3) can

Table 1: Overview of the methods implemented in *exciting*. The features marked with an asterisk are currently in development. The acronyms are explained in Section 3.

Property	Method/module	Approximation	SOC	Comment
KS electrons	DFT	LDA, GGA, DFT-1/2,	SV, SVLO, core: Dirac	direct or via Libxc
		meta-GGA (mGGA), OEP	SV, SVLO, core: Dirac	
gKS electrons		HF, PBE0, HSE	SV, SVLO*	parameters adjustable
QPs	<i>GW</i>	$G_0W_0$	SV	various starting points
		QSGW	—	various starting points
	EPC	MBPT	—	temperature effects, various starting points
Phonon spectra	DFPT	LDA, GGA	—	
	supercells	various	—	
Optical spectra	LR-TDDFT	IPA, RPA, various kernels	—	
	BSE	IPA, RPA; TDA, full BSE	SV, SVLO	
Core spectra	BSE	IPA, RPA; TDA, full BSE	core: Dirac, cond. SV	
Pump-probe spectra	BSE & TDDFT	same as its components	—	
RIXS	BRIXS	IPA, RPA, BSE	—	
Pumped RIXS	BRIXS	IPA, RPA, BSE	—	analogous to pump-probe
Raman spectra		as optical spectra	as optical spectra	
IR spectra		as optical spectra	as optical spectra	
Exciton-polarons	DFPT & BSE	as DFPT / optical spectra		

be computed, including even pumped RIXS. The latest version of the code is accompanied by a number of tools, workflows, and interfaces, which all make *exciting* calculations convenient to handle. Besides the *exciting*-specific workflow tools (Section 9.2) *excitingworkflow*, *excitingtools*, and *excitingscripts*, we present our new version of *ElaStic* (Section 9.3) that also supports input from other codes. In addition to the above-mentioned interface to SIRIUS [32] (Section 9.4), there is an interface to the coupled cluster (CC) code Cc4s [38] (Section 9.5) and an interface to elphbolt [39] (Section 9.6), which computes transport properties. The stand-alone code *CELL* [40], a Python-based cluster expansion (CE) package, developed in the group, naturally works with *ab initio* input from *exciting*. *CELL* also reminds on machine learning (ML), since the CE technique itself can be viewed as a ML problem, *i.e.*, linear regression. One of the latest developments goes beyond by incorporating non-linearities [40] in the CE models. A novel workflow combines *CELL* and *exciting* in using the NOMAD infrastructure for building CE models for disordered systems. This has been implemented in the NOMAD Oasis, which is organized by the *exciting* developers from Berlin in collaboration with NOMAD. We report on this Oasis (Section 10.3), on ML tools for error quantification (Section 10.2), and on *FSvisual*, a package for viewing Fermi surfaces (Section 10.5).

**Tutorials.** Almost all of *exciting*'s features are covered by comprehensive, user-friendly tutorials, which not only teach new users the necessary know-how for running calculations with *exciting*, but have also proven to be a valuable guidebook for experienced users. In their latest version, every tutorial is implemented in a Jupyter notebook [41]. The users can follow the instructions and execute accompanying commands in their web browsers, avoiding the need to switch between the command line and the tutorial. The tutorials can also be executed in a continuous integration (CI) pipeline (see the test suites below), complementing the test suite with further applications of the code. This rigorous regression testing has unveiled a number of bugs before users could have been affected. Finally, the Jupyter framework allows direct conversion to an HyperText Markup Language (HTML) file, which is embedded into the *exciting* website (<https://exciting-code.org/home/tutorials-jupyter>). Thus, users can still view

the tutorials and follow along without running a Jupyter notebook on their machine. The relevant functionality is implemented in Python and distributed as part of the `exciting` source code.

**Test suite and continuous integration.** To ensure the high quality of `exciting` results, the code undergoes extensive testing. We distinguish three tiers of tests. The first tier consists of *unit tests* to verify that isolated functions and subroutines—the fundamental building blocks of `exciting`—produce the expected results. The second tier involves *regression tests*, where `exciting` calculations are executed and their outputs are checked against reference results to ensure numerical consistency. The third tier comprises *workflow tests*, which automatically run the `exciting` tutorials to verify that complex workflows involving multiple sequential runs function reliably. All tests are executed regularly within the development workflow through CI. The CI system builds the code and runs the entire test suite across different environments and build configurations, ensuring robustness and reproducibility.

## 2.3 Code summary and availability

`exciting` is developed as an open-source package and is publicly available for download at: <https://exciting-code.org/> and <https://github.com/exciting/>. The code is primarily written in Fortran 2018, with performance-critical components optimized for use on high-performance computers. The code requires a fast Fourier transform library that supports the FFTW3 interface and BLAS/LAPACK implementation, *e.g.*, OpenBLAS, Intel MKL, Cray LibSci, etc. Also MPI and an OpenMP-capable Fortran compiler are required. The software is bundled with Libxc, FoX, and BSPLINE-FORTRAN, while also allowing the use of an externally provided Libxc installation. The build can optionally interface with HDF5 to enable scalable, platform-independent I/O. To accelerate performance, the code can interface with ELPA, ScaLAPACK and SIRIUS. GPU-aware builds rely on vendor-specific accelerator libraries, such as Intel oneAPI, CUDA/cuBLAS, or ROCm, depending on the target platform. Moreover, an optimized binary is available for physically unified-memory systems, representing cutting-edge hardware where the CPU and GPU share the memory space.

Based on CMake, the build system supports a wide range of contemporary platforms and toolchains. Currently supported Fortran compilers include GNU Fortran (GCC  $\geq 11$ ), Intel oneAPI Fortran (IFX)—excluding the BSE module—Cray, and the new AMD compiler Flang. Support for legacy compilers, including Intel IFORT, is currently being deprecated in favor of standards-compliant, actively maintained compiler toolchains. GPU support requires a performant compiler capable of OpenMP offloading, for which currently, Cray, AMD Flang, and IFX are supported.

The code is distributed under the GNU General Public License, ensuring free use, modification, and redistribution in accordance with open-source principles. The release series follows a naming convention based on elements of the periodic table, with the current version being `exciting-sodium`. All development within the core developer group follows a thorough peer-review prior to integration, using an in-house git repository, hosted on the gitlab servers of the Humboldt-Universität zu Berlin. External developments and co-developments are welcome. If you are interested in contributing, please contact us.

### 3 Ground state

#### 3.1 State of the art

The accurate description of the electronic GS constitutes the conceptual and numerical basis for all excited-state methodologies discussed in this review. KS theory [1, 2] is the method of choice on which most GS calculations for extended systems are based. Solving the KS equations provides the KS eigenvalues and wavefunctions, which are used not only to obtain the GS total energy and electronic density, but also to establish a well-defined GS starting reference for MBPT, linear-response approaches, and spectroscopic simulations.

The accuracy and efficiency of KS-DFT depend critically on the level of approximation adopted for the exchange-correlation (xc) functional. Considerable efforts are being made to implement and use better functionals beyond the most widely used semilocal ones. Higher levels of sophistication can be reached by climbing up John Perdew's Jacob's ladder [42]. The approximations that have attracted the most attention in recent years are mGGA and hybrid functionals. mGGA functionals [43, 44] are the rung between generalized gradient approximation (GGA) and hybrid xc functionals. They often yield improved accuracy at only a moderate increase in computational complexity, sometimes even matching the accuracy of computationally much more demanding hybrid xc functionals [45]. A rather complete list of mGGA functionals is available in the Libxc library [30, 31]. Libxc has also been recently extended to include widely used treatments of van der Waals interactions [46].

Modifications of the standard KS framework lead to the generalized Kohn-Sham (gKS) formalism, in which the effective single-particle Hamiltonian contains explicit non-local operators [47]. The most prominent examples are hybrid xc functionals, which incorporate a fraction of exact (Fock) exchange [48, 49], as well as related approaches employing screened or range-separated exchange [50]. These non-local contributions render the effective single-particle potential explicitly orbital dependent and go beyond the purely multiplicative KS potential of semilocal functionals. By incorporating a fraction of exact exchange, hybrid and local-hybrid functionals reduce self-interaction errors and improve the description of localized electronic states, band gaps, and weakly screened systems [48, 51].

Compared to conventional KS-DFT, gKS methods often yield significantly improved orbital energies, including band gaps and ionization potentials, and provide a more reliable single-particle electronic structure as a starting point for excited-state theories [52]. Spin polarization and spin-orbit coupling can be consistently incorporated within both KS and gKS frameworks and are essential for magnetic materials and systems containing heavy elements.

By explicitly incorporating information from unoccupied KS orbitals, the xc functionals on the fifth (top) rung of Jacob's ladder enable the description of non-local electron correlation effects. The two representative classes of fifth-rung functionals that have been actively developed in recent years are the random phase approximation (RPA) and double-hybrid approximations (DHAs). Both approximation types can be derived within the framework of the adiabatic coupling (AC) approach to DFT [53, 54] and are reviewed in detail in Ref. [55].

Beyond the choice of xc functional, the numerical realization of the KS or gKS equations plays a decisive role in the reliability of GS results, including the representation of wavefunctions and potentials and the treatment of core and valence electrons. All-electron methods avoid pseudization and treat core and valence electrons on the same footing, thereby ensuring transferability across the periodic table and enabling direct access to core-level properties. Full-potential approaches further eliminate shape approximations to the effective potential and charge density, which is essential for low-symmetry systems, complex bonding environments, and accurate response properties.

Within this class, the LAPW+LO method is commonly employed as a reference all-electron framework, combining near variational completeness with systematic convergence control [56–58]. In this context, community-wide benchmarks have shown that independently developed KS-DFT implementations, when carefully converged, produce essentially identical GS properties despite their differing numerical approaches [59].

### 3.2 Methodology

In the following, we sketch the DFT formalism only to the extent needed to follow the remainder of this work. For more general considerations and details, we refer to the ample literature on this topic. The practical realization of the KS-DFT formalism relies on the numerical solution of the KS equations, a set of Schrödinger-like single-electron equations:

$$\hat{h}_{\text{KS}} \psi_{i\mathbf{k}}(\mathbf{r}) = \left( -\frac{\nabla^2}{2} + \hat{v}_{\text{KS}} \right) \psi_{i\mathbf{k}}(\mathbf{r}) = \epsilon_{i\mathbf{k}} \psi_{i\mathbf{k}}(\mathbf{r}) . \quad (4)$$

Many body (MB) effects are treated by considering an effective mean-field potential, the KS potential,

$$\hat{v}_{\text{KS}} = \hat{v}_{\text{ext}} + \hat{v}_{\text{H}} + \hat{v}_{\text{xc}} \quad \text{with} \quad \hat{v}_{\text{xc}} = \frac{\delta E_{\text{xc}}[n]}{\delta n(\mathbf{r})} , \quad (5)$$

which includes the interaction with the nuclei,  $\hat{v}_{\text{ext}}$ , the classical Hartree contribution,  $\hat{v}_{\text{H}}$ , and the xc potential,  $\hat{v}_{\text{xc}}$ . The formally unknown xc energy functional  $E_{\text{xc}}[n]$  needs to be approximated. The lowest level approximations are (semi)local functionals. The local density approximation (LDA) depends on the GS electron density only,

$$n_{\text{GS}}(\mathbf{r}) = \sum_{i,\mathbf{k}}^{\text{occ}} |\psi_{i\mathbf{k}}(\mathbf{r})|^2 , \quad (6)$$

the GGAs involve also the density gradient. By climbing up a further step of Jacob's ladder [42], we arrive at the mGGA functionals that include the second derivative of the electron density in the form of the Laplacian  $\nabla^2 n_{\text{GS}}(\mathbf{r})$  and/or the kinetic-energy density (KED)

$$\tau(\mathbf{r}) = \frac{1}{2} \frac{1}{N_{\mathbf{k}}} \sum_{i,\mathbf{k}}^{\text{occ}} |\nabla \psi_{i\mathbf{k}}(\mathbf{r})|^2 . \quad (7)$$

Since the KED is not an explicit functional of the density, functional derivatives with respect to the KS orbitals are used. This gives rise to an additional non-multiplicative contribution to the xc potential

$$\hat{v}_{\text{xc}}^{\text{mGGA}}(\mathbf{r}) \psi_{i\mathbf{k}}(\mathbf{r}) = \hat{v}_{\text{xc}}^{\text{mult}}(\mathbf{r}) \psi_{i\mathbf{k}}(\mathbf{r}) - \frac{1}{2} \nabla \cdot \left[ \frac{\partial \varepsilon_{\text{xc}}^{\text{mGGA}}}{\partial \tau(\mathbf{r})} \nabla \psi_{i\mathbf{k}}(\mathbf{r}) \right] . \quad (8)$$

The next rung of Jacob's ladder incorporates also the unoccupied orbitals into the xc functional. Treating the exchange interactions exactly can be implemented in two ways. In the optimized effective potential (OEP) method [60], a local potential is constructed, while the incorporation of Hartree-Fock (HF) exchange leads to a nonlocal potential, giving rise to the gKS equations,

$$\left( -\frac{\nabla^2}{2} + \hat{v}_{\text{ext}} + \hat{v}_{\text{H}} + \hat{v}_{\text{NL}}[\{\psi_{i\mathbf{k}}\}] + v_{\text{s}}[n_{\text{GS}}] \right) \psi_{i\mathbf{k}}(\mathbf{r}) = \epsilon_{i\mathbf{k}} \psi_{i\mathbf{k}}(\mathbf{r}) , \quad (9)$$

where non-local operator  $\hat{v}_{\text{NL}}[\{\psi_{i\mathbf{k}}\}]$  depends on all occupied orbitals. In hybrid functionals, the Fock operator is only used to a certain fraction  $\alpha$ , while the remaining exchange effects are treated on the semilocal level,

$$E_{\text{xc}}^{\text{hyb}} = \alpha E_{\text{x}}^{\text{HF}} + (1 - \alpha) E_{\text{x}}^{\text{GGA}} + E_{\text{c}}^{\text{GGA}} , \quad (10)$$

where  $E_{\text{x}}^{\text{HF}}$  and  $E_{\text{x}}^{\text{GGA}}$  are the Fock and GGA exchange energies. A prominent example of such global hybrid functionals is PBE0 [47], with the mixing parameter  $\alpha=0.25$ . The most prominent example of range-separated hybrid functionals is HSE06 [48, 49],

$$E_{\text{xc}}^{\text{HSE06}} = E_{\text{xc}}^{\text{PBE}} + \alpha \left( E_{\text{x}}^{\text{HF},\text{sr}}(\omega) - E_{\text{x}}^{\text{PBE},\text{sr}}(\omega) \right) , \quad (11)$$

where  $E_{\text{xc}}^{\text{PBE}}$  is the PBE functional [61] and  $\omega$  an adjustable parameter that triggers the separation between long-range and short-range (sr) contributions.

### 3.3 Meta-GGAs in **exciting**

**exciting** implements mGGA functionals using the Libxc library [30, 31], thus providing all functionals implemented therein. mGGA can improve over the LDA or GGAs in the prediction of band gaps at only a slight increase in computational cost, yielding results similar to hybrid functionals. For this purpose, the TASK functional proves favorable as shown in Fig. 1, while SCAN or r2SCAN yield lattice constants closest to experiment.

Concerning the implementation, complications arise when solving the radial Schrödinger and Dirac equations for obtaining the radial parts of the APW basis functions and the core states, respectively. The standard integration approach does not work because the action of the (spherical) potential on the radial functions is unknown prior to integration but depends on the yet unknown radial functions due to the presence of a non-multiplicative contribution to the potential. Therefore, **exciting** follows Refs. [62, 63] and circumvents this issue by computing a GGA potential in each iteration and using its spherical part for the update of core states and radial basis functions. As a consequence, a mGGA calculation in **exciting** starts with a GGA iteration to produce an initial set of wavefunctions, from which the KED is computed. From then onward, the mGGA potential is used to compute the Hamiltonian, the wavefunctions, and the electron density, which is then used to update both the mGGA and GGA potentials. In principle, there is an optimal type of GGA functional best suited for each type of mGGA functional [63]. In practice, however, it turns out that PBE performs well for all flavors of mGGA.

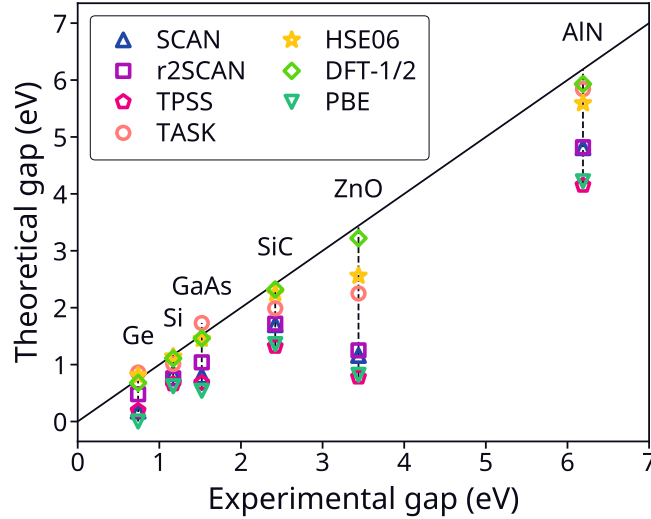


Figure 1: Band gaps obtained with different metaGGA functionals. For comparison, PBE [64], HSE06 [64], and DFT-1/2 results are shown. All calculations were carried out with **exciting**.

### 3.4 DFT-1/2

While methods such as *GW* or hybrid functionals produce significantly improved band gaps compared to semilocal DFT, they are computationally much more demanding and may become impractical for large or complex systems. The DFT-1/2 approach [65] offers a compelling compromise: band gaps, ionization potentials, and defect levels can be obtained with accuracy close to that of higher-level methods while retaining the low computational cost of semilocal functionals [65–73]. This makes DFT-1/2 a highly efficient alternative when more demanding methods are not feasible.

The DFT-1/2 method resembles Slater’s transition-state technique, in which the ionization energy of a given single-particle state is approximated by enforcing its half-occupation. In DFT-1/2, however, half-occupations are not treated explicitly. Instead, a modified set of KS equations is solved:

$$\left( -\frac{\nabla^2}{2} + \hat{v}_{\text{KS}} - \hat{v}_{\text{s}} \right) \psi_{i\mathbf{k}}(\mathbf{r}) = \epsilon_{i\mathbf{k}} \psi_{i\mathbf{k}}(\mathbf{r}), \quad (12)$$

where  $\hat{v}_s$  is the so-called “self-energy potential” named for its analogy with the classical self-energy. The potential  $\hat{v}_s$  is constructed in such a way to incorporate the effect of half-occupation. For a compound, it is typically derived from KS calculations of the isolated constituent atoms and subsequently trimmed to remove the  $1/r$  divergence [65]. As evident from Eq. (12), DFT-1/2 retains the simplicity of semilocal functionals. At the same time, it can yield electronic properties with an accuracy comparable to that of mGGAs, hybrid functionals, or even  $GW$ . This is illustrated in Fig. 1 for the band gaps of a variety of materials. Therefore, DFT-1/2 also provides an appealing starting point for  $G_0W_0$ . In this case, the resulting QP shifts are expected to be small, so the perturbative treatment is therefore well justified [72]. Accordingly, the DFT-1/2 method is available as starting-point for  $G_0W_0$  [72] in **exciting**. A detailed description of the implementation can be found in Ref. [69].

### 3.5 Hybrid functionals in **exciting**

As another solution to the band-gap problem in DFT, **exciting** implements the hybrid functionals PBE0 [47] and HSE06 [48, 49]. It requires the non-local exchange defined as

$$\hat{v}_x^{\text{HF}} \psi_{n\mathbf{k}}(\mathbf{r}) = -\frac{1}{N_{\mathbf{k}}} \sum_{n'\mathbf{k}'} \psi_{n'\mathbf{k}'}(\mathbf{r}) \int \psi_{n'\mathbf{k}'}^*(\mathbf{r}') \psi_{n\mathbf{k}}(\mathbf{r}') v(|\mathbf{r} - \mathbf{r}'|) d\mathbf{r}', \quad (13)$$

where  $v(r) = 1/r$  is the Coulomb kernel that becomes  $v(r) = \text{erfc}(\omega r)/r$  in the screened case needed for HSE06. Including this term in a calculation requires evaluation of the matrix elements  $\langle \phi_{\mathbf{G}}^{\mathbf{k}} | \hat{v}_x^{\text{HF}} | \phi_{\mathbf{G}'}^{\mathbf{k}'} \rangle$ , which is implemented in **exciting** in two ways [74, 75]. The first one follows the approach introduced in Ref. [76] and approximates the exchange operator as

$$\hat{v}_x^{\text{MB}} = \sum_{nn'\mathbf{k}} |\psi_{n\mathbf{k}}\rangle \langle \psi_{n\mathbf{k}}| \hat{v}_x^{\text{HF}} |\psi_{n'\mathbf{k}}\rangle \langle \psi_{n'\mathbf{k}}|. \quad (14)$$

To obtain the matrix elements  $\langle \psi_{n\mathbf{k}} | \hat{v}_x^{\text{HF}} | \psi_{n'\mathbf{k}} \rangle$ , products of wavefunctions are expressed in terms of the mixed product basis functions that are discussed in more detail in Section 5.3 (hence the label MB in  $\hat{v}_x^{\text{MB}}$ ). The projection of the Fock exchange on wavefunctions in Eq. (14) introduces a dependence of the total energy and the band energies on the number of empty bands used in the calculation. We overcome this issue and gain control over the precision of hybrid calculations in the alternative implementation that adopts the adaptively compressed exchange (ACE) [77]. It introduces a different low-rank approximation:

$$\hat{v}_x^{\text{ACE}} = \sum_{nn'\mathbf{k}} |W_{n\mathbf{k}}\rangle (M_{\mathbf{k}}^{-1})_{nn'} \langle W_{n'\mathbf{k}}|, \quad (15)$$

with  $W_{n\mathbf{k}}(\mathbf{r}) = \hat{v}_x^{\text{HF}} \psi_{n\mathbf{k}}(\mathbf{r})$  that converges to the exact result for the given basis once self-consistency is reached. Note that the radial functions are generated using a local potential,  $v_0^{\alpha}(r)$ , even though the potential in hybrids has a non-local contribution. The usual approach in LAPW is to precompute the radial basis as well as core orbitals with GGA and employ them unmodified in hybrids [76, 78]. We addressed this deficiency by implementing a radial solver that generates radial functions and core orbitals consistent with hybrids [79, 80]. This approach employed together with ACE recovers the micro-Ha precision for absolute total energies in calculations with hybrid functionals.

In the ACE code, we follow Eq. (13) directly and evaluate the convolution integral for every pair of wavefunctions using the pseudocharge method [81] and its modifications [64] for the bare and screened Coulomb kernels, respectively. With  $N_{\text{at}}$  being the number of atoms, the computational effort scales as  $O(N_{\text{at}}^4)$  as in the other implementation. In the ACE code, this scaling derives from calculating the convolution integral that has to be evaluated for all  $O(N_{\text{at}}^2)$  pairs of wavefunctions, requiring  $O(N_{\text{at}}^2)$  floating-point operations for periodic systems. Ref. [64] discusses modifications of the pseudocharge method that allowed us to reduce the scaling of its most time-consuming steps and thus make first steps towards the overall  $O(N_{\text{at}}^3 \log N_{\text{at}})$  effort in ACE calculations.

### 3.6 SVLO: An efficient basis for spin-orbit coupling

In materials with sizeable SOC, the conventional second-variational (SV) treatment may require a prohibitively large number of unoccupied scalar-relativistic (SR) states to converge SOC-induced splittings and derived properties. To overcome this limitation, `exciting` implements the SVLO approach, which accelerates SOC calculations by explicitly enriching the SV basis in the vicinity of the atomic nuclei, where relativistic effects are strongest. A detailed description and benchmarks can be found in Ref. [29]. Starting from the SR KS eigenstates  $\psi_{jk}^{\text{SR}}(\mathbf{r})$ , the conventional SV spinors are written as

$$\Psi_{n\mathbf{k}}^{\text{SV}}(\mathbf{r}) = \sum_{\sigma} \sum_{j=1}^{N_b^{\text{SV}}} C_{nj\sigma}^{\text{SV}}(\mathbf{k}) \psi_{jk}^{\text{SR}}(\mathbf{r}) |\sigma\rangle, \quad (16)$$

where the SV subspace size  $N_b^{\text{SV}} = N_{\text{occ}} + N_{\text{unocc}}$  denotes the number of SR states entering the SV step. For systems with strong SOC, the required number of unoccupied states  $N_{\text{unocc}}$  can become prohibitively large. The SVLO scheme addresses this bottleneck by augmenting the SV basis with explicit LOs, including Dirac-type LOs that accurately capture the near-nuclear behavior of relativistic states. In particular, when heavy-element  $p$  states dominate the band edges,  $p_{1/2}$ -type LOs become essential [82]. To avoid linear dependencies, SVLO constructs modified SR basis functions with the LO components removed. Introducing the combined SVLO basis  $\{\chi_{m\mathbf{k}}\} = \{\bar{\psi}_{jk}^{\text{SR}}\} \cup \{\phi_{\mu}\}$ , the SOC spinors are expanded as

$$\Psi_{n\mathbf{k}}^{\text{SVLO}}(\mathbf{r}) = \sum_{\sigma} \sum_{m=1}^{N_b^{\text{SVLO}}} C_{nm\sigma}^{\text{SVLO}}(\mathbf{k}) \chi_{m\mathbf{k}}(\mathbf{r}) |\sigma\rangle, \quad (17)$$

with  $N_b^{\text{SVLO}} = N_{\text{occ}} + N_{\text{unocc}} + N_{\text{LO}}$ .

In practice, SVLO enables a substantial reduction of the SV subspace, allowing for highly precise calculations. For example, Fig. 2 shows for  $\gamma\text{-CsPbI}_3$  that the SVLO basis with  $N_{\text{occ}} = 228$  and  $N_{\text{LO}} = 496$  reaches convergence of the band gap already with about 500 unoccupied states, while the conventional SV basis requires several thousand to achieve the same value. This reduction of the SV subspace shows a sizable speedup by a factor of 3.6 at comparable precision [29].

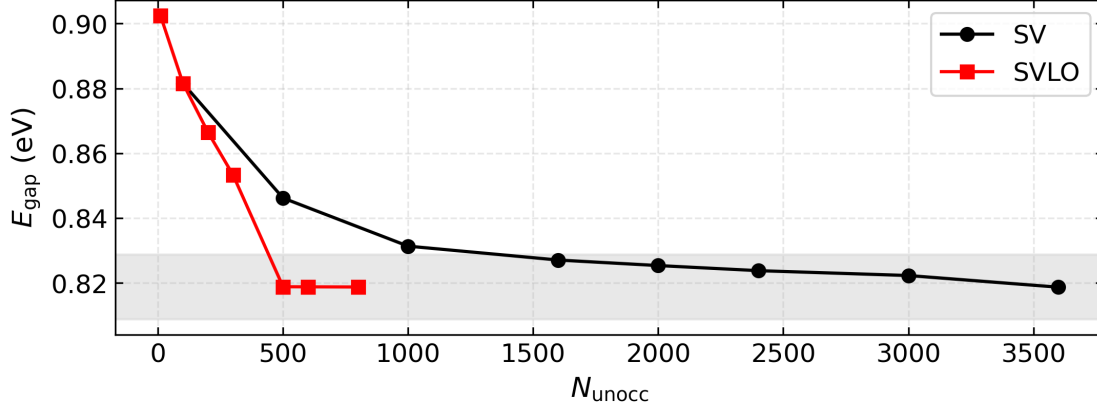


Figure 2: Convergence of the band gap  $E_{\text{gap}}$  of  $\gamma\text{-CsPbI}_3$  with respect to the number of unoccupied states  $N_{\text{unocc}}$ , comparing SV and SVLO. The gray shaded area indicates a tolerance window of  $\pm 0.01$  eV around the converged value

The same formalism has also been employed to accelerate BSE calculations in the presence of SOC (see Section 6.4).

### 3.7 Constrained DFT

The BSE is considered the state-of-the-art method for modeling neutral excitations, as it explicitly addresses electron–hole interactions. However, its high computational cost and unfavorable scaling with

system size hampers its use for complex materials. In such cases, cDFT offers an attractive alternative. By imposing occupation constraints to mimic excited-state configurations, it can capture essential excitation characteristics with an accuracy comparable to BSE at a fraction of the computational expense, in particular if the electron-hole pairs are confined, *i.e.*, don't require large supercells. This approach has already proven rather successful in the so-called supercell corehole approach, but is not limited to core excitations. It has been applied to a variety of systems, including molecules, organic dyes, and perovskites [83–88], making it a practical and scalable option when full BSE calculations are not feasible. In exciting, cDFT serves as an efficient approach for modeling excitations following picosecond time delays in pump-probe experiments (see Section 8.3). The core idea in cDFT is to solve the KS equations while keeping the electronic occupations fixed in a non-equilibrium configuration. Initially, a standard GS calculation is performed to determine the equilibrium occupation numbers  $f_{n\mathbf{k}}$  and the corresponding electronic density:

$$n_{\text{KS}}(\mathbf{r}) = \sum_{n\mathbf{k}} w_{\mathbf{k}} f_{n\mathbf{k}} |\psi_{n\mathbf{k}}(\mathbf{r})|^2. \quad (18)$$

The occupation factors are then constrained based on physical considerations, such as mimicking a specific excitonic state identified with higher-order theories (*e.g.*, BSE) or simulating the electron-hole pairs generated in a pump-probe experiment. For a given number of excited carriers per unit cell,  $N_{\text{exc}}$ , the changes in the carrier distribution,  $\Delta f_{n\mathbf{k}}$ , must satisfy:

$$\sum_{n\mathbf{k}}^{\text{val}} w_{\mathbf{k}} \Delta f_{n\mathbf{k}} = \sum_{n\mathbf{k}}^{\text{cond}} w_{\mathbf{k}} \Delta f_{n\mathbf{k}} = N_{\text{exc}}, \quad (19)$$

where the summations are performed over valence and conduction states, respectively, to model excited holes and electrons. The electron density  $n'_{\text{KS}}$  under the presence of excitations is constructed as:

$$n'_{\text{KS}}(\mathbf{r}) = \sum_{\mathbf{k}} w_{\mathbf{k}} \left[ \sum_n f_{n\mathbf{k}} |\psi'_{n\mathbf{k}}(\mathbf{r})|^2 + \sum_n^{\text{cond}} \Delta f_{n\mathbf{k}} |\psi'_{n\mathbf{k}}(\mathbf{r})|^2 - \sum_n^{\text{val}} \Delta f_{n\mathbf{k}} |\psi'_{n\mathbf{k}}(\mathbf{r})|^2 \right], \quad (20)$$

where  $\psi'_{n\mathbf{k}}$  denotes the non-equilibrium KS states. This excited-state density is subsequently used to build the KS hamiltonian. Following the usual procedure, the KS equations are solved iteratively until self-consistency is achieved. Further details regarding implementation and applications can be found in Refs. [89, 90].

### 3.8 Wannier interpolation

Wannier functions  $w_{n\mathbf{T}}(\mathbf{r})$  provide an alternative to the representation of a subspace of bands by Bloch states  $\psi_{n\mathbf{k}}(\mathbf{r})$  and are labeled by band-like index  $n$  and a unit-cell  $\mathbf{T}$  within the Born-von Karman (BvK) super cell. They can be defined by a Fourier-like transform of rotated Bloch states

$$w_{n\mathbf{T}}(\mathbf{r}) = \frac{1}{N_{\mathbf{k}}} \sum_{\mathbf{k}} e^{-i\mathbf{k}\cdot\mathbf{T}} \sum_m U_{mn}(\mathbf{k}) \psi_{m\mathbf{k}}(\mathbf{r}), \quad (21)$$

and the unitary rotations  $U(\mathbf{k})$  can be tuned in order to find maximally localized Wannier functions (MLWFs). The inversion of Eq. (21) for any arbitrary point  $\tilde{\mathbf{k}}$  allows for the interpolation of the KS wave functions in reciprocal space. The corresponding unitary matrices  $U(\tilde{\mathbf{k}})$  can be found as the eigenvectors of the interpolated Hamiltonian

$$H_{mn}(\tilde{\mathbf{k}}) = \sum_{\mathbf{T}} e^{i\tilde{\mathbf{k}}\cdot\mathbf{T}} \langle w_{m0} | \hat{h}_{\text{KS}} | w_{n\mathbf{T}} \rangle, \quad (22)$$

whose eigenvalues give the corresponding interpolated electron energies  $\epsilon_{n\tilde{\mathbf{k}}}$ . The reasons for the efficiency of this interpolation approach are: (i) the MLWFs  $w_{n\mathbf{T}}(\mathbf{r})$  and hence the real space Hamiltonian in the Wannier representation  $H(\mathbf{T}) = \langle w_0 | \hat{h}_{\text{KS}} | w_{\mathbf{T}} \rangle$  are  $\mathbf{k}$ -independent and thus only need to be calculated once

prior to the interpolation, (ii) the interpolation to arbitrary points  $\tilde{\mathbf{k}}$  is obtained by a simple Fourier transform, (iii) the diagonalization of the interpolated Hamiltonian  $H(\tilde{\mathbf{k}})$  is quick since the MLWFs provide a minimal basis, *i.e.*, there is only one basis function for each band  $n$  inside the subspace of interest (*e.g.*, a few bands around the Fermi level), and thus the Hamiltonian in Wannier representation is typically much smaller than the Hamiltonian in the original basis, and (iv) due to the strong localization of the MLWFs, the real space Hamiltonian  $H(\mathbf{T})$  typically decays rapidly (often exponentially) and thus the sum over lattice vectors  $\mathbf{T}$  converges quickly within the BvK super cell.

**exciting** allows for the calculation of MLWFs representing both isolated [91] (*e.g.*, valence bands in insulators) and entangled Souza *et al.* [92] (*e.g.*, conduction bands or bands in metals) subspaces of bands. In addition of the two step procedure for entangled subspaces described in [92], **exciting** also implements the variational formalism described by Damle *et al.* [93]. A special feature of **exciting** is that there is no need to manually provide a set of projection functions in order to obtain an initial guess for the gradient based optimization of  $U(\mathbf{k})$ . We automatically generate such an initial guess by finding optimized projection functions as a linear combination of automatically generated LOs. The only input required by the user is the subspace of bands for which MLWFs are aimed to be computed. This can either be a range of band indices or a given energy window. For a detailed description of the implementation within **exciting** we refer to previous publications [94, 95]. MLWFs can be calculated from both DFT, generalized DFT (gDFT), and  $GW$  input and hence allow for the interpolation of wavefunctions and eigenenergies from KS-DFT, DFT with hybrid xc functionals, and  $GW$  calculations thereby enabling the calculation of accurate band structures and density of states (DOS) on different levels of sophistication (see Fig. 3). Further, MLWFs might be used to compute energy band derivatives, *i.e.*, electron group velocities and effective masses, and for the automatic search of band extrema away from high-symmetry points. Beyond the interpolation of wavefunctions and energies, Wannier interpolation can also be used to interpolate matrix elements as we do for the electron–phonon matrix  $g(\mathbf{k}, \mathbf{q})$  for the calculation of electron renormalization due to electron–phonon interaction (see Section 4).

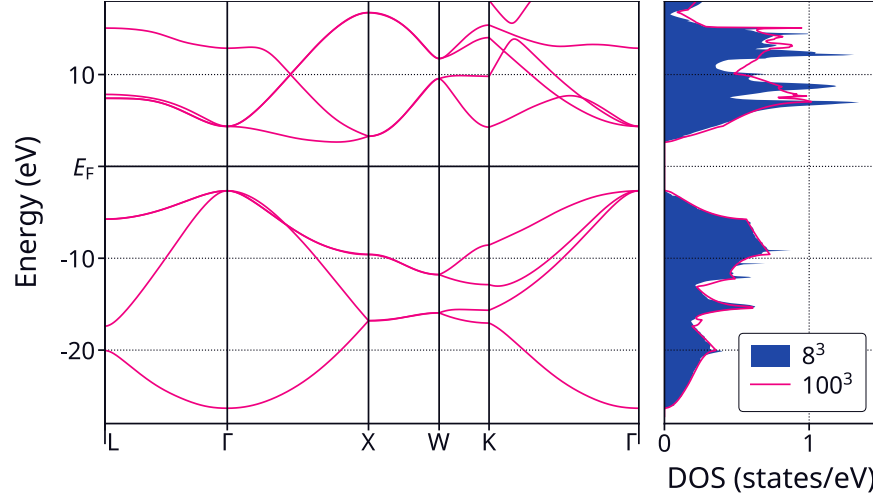


Figure 3: Left: Band structure of diamond obtained using Wannier interpolation of eigenvalues from an  $8^3$   $\mathbf{k}$ -grid using gDFT with the HSE functional. Right: DOS as obtained from the original coarse grid (blue) and converged result obtained using Wannier interpolation on a grid of  $100^3$  points (red).

### 3.9 Exploiting symmetry

The exploitation of crystal symmetry is essential for achieving high efficiency at fixed precision. Their systematic implementation in **exciting** significantly reduces computational cost and memory consumption, particularly for large unit cells and dense Brillouin-zone samplings. Inside the MT spheres, the KS potential is expanded in symmetry-adapted angular functions (lattice harmonics). This enforces the crystal symmetry by construction and reduces the number of independent expansion coefficients. As a result,

both the generation of the effective potential and the subsequent setup of the KS eigenvalue problem are accelerated. For inversion-symmetric systems, the KS eigenvalue problem can be formulated in terms of real symmetric matrices, requiring a real solver only. This substantially reduces the computational effort required for diagonalization. In practice, `exciting` achieves a speedup of roughly a factor of four compared to the complex formulation, consistent with results reported for other LAPW+LO codes [96].

## 4 Lattice dynamics

### 4.1 State of the art

DFPT is nowadays the method of choice for most phonon calculations, being implemented in many electronic-structure codes. Since it does not involve supercells, it is not restricted to certain high-symmetry  $\mathbf{q}$ -points and is typically computationally more efficient. It naturally provides also access to the response to perturbations other than atomic displacements such as electric fields or mechanical strain. However, the finite difference approach to phonons is still appealing due to its conceptual simplicity and it proves advantageous for systems with large unit cells, reduced symmetry or defects, or in highly anharmonic materials. The self-consistent phonon method combines inherently harmonic DFPT with a series of special finite displacements [97] in order to capture anharmonic effects such as temperature dependent phonon softening and phase stabilization. Abandoning the Born-Oppenheimer approximation, recent work [98] has studied the phonon contribution to the total energy, which is essential for the correct description of phase diagrams of materials with different polymorphs that differ little in total energy.

The calculation of electron and phonon lifetimes and band structure renormalization due to electron-phonon coupling (EPC) as described within MBPT is nowadays routinely carried out using different codes such as Abinit, VASP, or Quantum ESPRESSO + EPW. All-electron full-potential results are still scarce, though, and `exciting` is now filling this gap. The reproducibility of the zero-point renormalization (ZPR) within different methods and implementations has been verified recently [99]. Current developments in the calculation of electron self-energies target the partially self-consistent calculation of spectral functions including vertex corrections for the more accurate description of EPC-induced features like kinks and satellites [100]. Attempts to treat electron-phonon and electron-electron interaction simultaneously in a self-consistent fashion have been made by combining the perturbative description of EPC with the  $GW$  method (see also Section 5). One phenomenon where the established perturbative approach breaks down, is the formation of localized electron or hole states caused by local lattice distortions, called polarons. Theories and practical implementations for the calculation of polaron formation energies, self-trapping, their spatial distribution and their effect on the ZPR have been developed [101–104]. Increasing attention has also been drawn on the interaction of phonons with other quasi-particles like magnon-phonon interaction [104] or exciton-phonon interaction. For the latter we refer to Section 6. Finally, phonons and EPC also play a crucial role in the description of charge and heat transport as well as superconductivity within the Migdal-Eliashberg formalism. Several codes utilize phonons, EPC constants and other results from various first-principle codes as input for the calculation of transport-properties, *e.g.*, in the framework of the Boltzmann transport equations (BTEs). Examples are EPW, Perturbo, and elphbolt. Converged transport calculations typically require ultra-fine Brillouin zone (BZ) samplings to accurately capture small energy differences around the Fermi surface. Significant performance gains in this area have been achieved by the use of compressed representations of electron-phonon and phonon-phonon coupling constants [105, 106].

### 4.2 Methodology

The calculation of the linear response of the electronic system to an external perturbation lies at the heart of DFPT. The KS equations are replaced by their first order counterpart, the so-called Sternheimer equation

$$\left[ \hat{h}_{\text{KS}}^{(0)} - \epsilon_{n\mathbf{k}}^{(0)} \right] \psi_{n\mathbf{k}}^{(1)}(\mathbf{r}) = - \left[ \hat{h}_{\text{KS}}^{(1)} - \epsilon_{n\mathbf{k}}^{(1)} \right] \psi_{n\mathbf{k}}^{(0)}(\mathbf{r}) , \quad (23)$$

which, for a given first-order response of the KS Hamiltonian  $\hat{h}_{\text{KS}}^{(1)}$ , can be solved for the first-order response of the wavefunctions  $\psi_{n\mathbf{k}}^{(1)}(\mathbf{r})$  and eigenenergies  $\epsilon_{n\mathbf{k}}^{(1)}$ . Similar to the KS equations, Eq. (23) has to be solved self-consistently for the first-order response of the density  $n_{\text{KS}}^{(1)}(\mathbf{r})$  and the potential  $\hat{v}_{\text{KS}}^{(1)}(\mathbf{r})$ . For the specific case of lattice dynamics, the considered external perturbation is a collective coherent displacement of the nuclei out of their equilibrium positions,

$$\mathbf{R}_{L\alpha} = \mathbf{R}_{L\alpha}^{(0)} + e^{i\mathbf{q}\cdot\mathbf{T}_L} \boldsymbol{\tau}_\alpha , \quad (24)$$

and Eq. (23) is solved for the corresponding first-order responses  $\psi^{(\mathbf{q}\alpha i)}$ ,  $\epsilon^{(\mathbf{q}\alpha i)}$ ,  $n_{\text{KS}}^{(\mathbf{q}\alpha i)}$ , and  $\hat{v}_{\text{KS}}^{(\mathbf{q}\alpha i)}$ , where  $\mathbf{q}$  is the phonon wavevector. Eventually, the dynamical matrix  $\mathcal{D}$  is obtained from the first-order response of the atomic forces

$$\sqrt{M_\alpha M_{\alpha'}} \mathcal{D}_{\alpha i, \alpha' j}(\mathbf{q}) = - \sum_L e^{i\mathbf{q} \cdot \mathbf{T}_L} \frac{\partial F_{\alpha' j}}{\partial \mathbf{R}_{\alpha i L}} = -F_{\alpha' j}^{(\mathbf{q}\alpha i)}, \quad (25)$$

and the vibrational eigenmodes are given by its eigenvalues and eigenvectors:

$$\mathcal{D}(\mathbf{q}) \cdot \mathbf{w}_\nu = \omega_\nu^2 \mathbf{w}_\nu. \quad (26)$$

A complete description of lattice dynamics must also take into account the long-range dipole interactions that may be induced in polar materials by the atomic displacements. They lead to an additional non-analytic contribution to the dynamical matrix, which allows for the correct description of the splitting of longitudinal and transverse optical phonon modes. The key ingredients needed to fully capture this potentially anisotropic effects are the Born effective charge tensors  $\mathbf{Z}_\alpha^*$ , which describe the macroscopic polarization induced by the displacement of atom  $\alpha$ , and the dielectric constant  $\epsilon$ , which describes the connection between the macroscopic displacement field and an external electric field  $\mathbf{E}$  [107, 108]. The Born effective charges are computed as the derivatives of the macroscopic polarization with respect to nuclear displacements,

$$\mathbf{Z}_\alpha^* = \Omega \frac{\partial \mathbf{P}}{\partial \mathbf{S}_\alpha}, \quad (27)$$

the dielectric constant is computed from the derivatives of the electronic contribution to the polarization with respect to a static electric field

$$\epsilon^\infty = 1 + 4\pi \frac{\partial \mathbf{P}^{\text{el}}}{\partial \mathbf{E}}. \quad (28)$$

All necessary derivatives are obtained within DFPT.

The interaction of electrons with the vibrational modes may renormalize the electronic structure. To capture this effect, Green-function based methods from MBPT are employed. The key ingredient are the EPC constants

$$g_{mn,\nu}(\mathbf{k}, \mathbf{q}) = \sum_{\alpha, i} \frac{1}{\sqrt{2M_\alpha \omega_\nu}} \mathbf{w}_{\alpha i, \nu} \langle \psi_{m\mathbf{k}+\mathbf{q}} | \hat{v}_{\text{KS}}^{(\mathbf{q}\alpha i)} | \psi_{n\mathbf{k}} \rangle, \quad (29)$$

describing the transition probability for the scattering of the electron from the initial state  $\psi_{n\mathbf{k}}$  into the final state  $\psi_{m\mathbf{k}+\mathbf{q}}$  by the interaction with a phonon in mode  $\nu\mathbf{q}$ . The electron self-energy contribution due to EPC mainly consists of two parts, the Fan-Migdal self-energy,

$$\Sigma_{nn'}^{\text{FM}}(\omega, \mathbf{k}, T) = \sum_{\nu, m} \int_{\text{BZ}} \frac{d\mathbf{q}}{\Omega_{\text{BZ}}} g_{mn,\nu}^*(\mathbf{k}, \mathbf{q}) g_{mn',\nu}(\mathbf{k}, \mathbf{q}) \left[ \frac{f_{m\mathbf{k}+\mathbf{q}}(T) + n_{\nu\mathbf{q}}(T)}{\omega - \epsilon_{m\mathbf{k}+\mathbf{q}} + \omega_{\nu\mathbf{q}} + i\eta} + \frac{1 - f_{m\mathbf{k}+\mathbf{q}}(T) + n_{\nu\mathbf{q}}(T)}{\omega - \epsilon_{m\mathbf{k}+\mathbf{q}} - \omega_{\nu\mathbf{q}} + i\eta} \right], \quad (30)$$

and the static Debye-Waller self-energy,

$$\Sigma_{nn'}^{\text{DW}}(\mathbf{k}, T) = \sum_{\nu} \int_{\text{BZ}} \frac{d\mathbf{q}}{\Omega_{\text{BZ}}} g_{nn',\nu}^{\text{DW}}(\mathbf{k}, \mathbf{q}) \left( n_{\nu\mathbf{q}}(T) + \frac{1}{2} \right), \quad (31)$$

where  $f(T)$  ( $n(T)$ ) is the temperature dependent fermionic (bosonic) occupation of the electrons (phonons). The Debye-Waller matrix elements are given by

$$g_{nn',\nu}^{\text{DW}}(\mathbf{k}, \mathbf{q}) = \sum_{\alpha, i, \alpha', j} \frac{1}{\sqrt{2M_\alpha \omega_{\nu\mathbf{q}}}} \mathbf{w}_{\alpha i, \nu}^* \langle \psi_{n\mathbf{k}} | \hat{v}_{\text{KS}}^{(-\mathbf{q}\alpha i, \mathbf{q}\alpha' j)} | \psi_{n'\mathbf{k}} \rangle \mathbf{w}_{\alpha' j, \nu} \frac{1}{\sqrt{2M_{\alpha'} \omega_{\nu\mathbf{q}}}}, \quad (32)$$

with the second-order potential response  $\hat{v}_{\text{KS}}^{(-\mathbf{q}\alpha i, \mathbf{q}\alpha' j)}$ . The knowledge of the self-energy allows for the calculation of temperature dependent renormalized quasi-particle energies via the solution of the Dyson equation,

$$\epsilon_{n\mathbf{k}}^{\text{QP}}(T) = \epsilon_{n\mathbf{k}} + \Sigma_{nn}(\epsilon_{n\mathbf{k}}^{\text{QP}}, \mathbf{k}, T). \quad (33)$$

EPC is also the driving mechanism behind conventional phonon-mediated superconductivity. A commonly used parameter is the dimensionless electron-phonon coupling strength,

$$\lambda(\epsilon) = 2 \int_0^\infty \frac{d\omega}{\omega} \alpha^2 F(\epsilon, \omega) , \quad (34)$$

which is used to estimate the critical transition temperature using empirical formulas. The Eliashberg spectral function  $\alpha^2 F(\epsilon, \omega)$  can be viewed as a weighted phonon DOS,

$$\alpha^2 F(\epsilon, \omega) = \sum_\nu \int_{BZ} \frac{d\mathbf{q}}{\Omega_{BZ}} \omega_{\nu\mathbf{q}} \lambda_{\nu\mathbf{q}}(\epsilon) \delta(\omega - \omega_{\nu\mathbf{q}}) , \quad (35)$$

where the weights are given by the phonon-mode resolved coupling strength,

$$\lambda_{\nu\mathbf{q}}(\epsilon) = \frac{1}{N(\epsilon) \omega_{\nu\mathbf{q}}} \sum_{mn} \int_{BZ} \frac{d\mathbf{k}}{\Omega_{BZ}} |g_{mn,\nu}(\mathbf{k}, \mathbf{q})|^2 \delta(\epsilon - \epsilon_{n\mathbf{k}}) \delta(\epsilon_{n\mathbf{k}} - \epsilon_{m\mathbf{k}+\mathbf{q}}) , \quad (36)$$

and  $N(\epsilon)$  is the electron DOS at energy  $\epsilon$ . While  $\lambda_{\nu\mathbf{q}}(\epsilon)$  provides a measure for how strong a specific phonon mode couples to electrons with a given energy  $\epsilon$ , it is also possible to define an equivalent electron-band resolved coupling parameter

$$\lambda_{n\mathbf{k}} = 2 \int_0^\infty \frac{d\omega}{\omega} \sum_{m,\nu} \int_{BZ} \frac{d\mathbf{q}}{\Omega_{BZ}} |g_{mn,\nu}(\mathbf{k}, \mathbf{q})|^2 \delta(\omega - \omega_{\nu\mathbf{q}}) \delta(\epsilon_{n\mathbf{k}} - \epsilon_{m\mathbf{k}+\mathbf{q}}) , \quad (37)$$

which describes the coupling of a specific electronic state to any phonon mode and is also called the mass-enhancement parameter, because the effective mass of a quasi-particle in that state is enhanced by a factor  $(1 + \lambda_{n\mathbf{k}})$ . Even though Eqs. (34) to (36) are commonly used in the context of superconductivity where the electron energy of interest is typically the Fermi level, *i.e.*,  $\epsilon = \epsilon_F$ , they can also be used to study the coupling to electronic states around any energy, even in insulating materials.

### 4.3 Phonons and electron-phonon coupling effects in **exciting**

**exciting** allows for the calculation of phonons using both DFPT and finite differences. The DFPT implementation fully exploits crystal symmetries by the use of special symmetry-adopted displacement patterns (irreducible representations). DFPT calculations are highly parallelized over both symmetry reduced  $\mathbf{k}$ - and  $\mathbf{q}$ -points as well as displacement patterns. DFPT currently supports all LDA and GGA functionals provided by LibXC. Spin-polarized calculations have not yet been implemented. For further details on the finite differences and DFPT implementations we refer to Refs. [20] and [109], respectively. The electron-phonon part of **exciting** can capture the impact of EPC on the electronic structure, *i.e.*, the phonon-renormalized quasi-particle energies. In order to converge BZ integrals such as in Eqs. (30) and (31), **exciting** employs Wannier-Fourier interpolation of electron energies, the dynamical matrices, and the electron-phonon matrix elements [110], including the long-range coupling in polar materials [111] onto a dense integration grid. Furthermore, tetrahedron integration is used, which is free of the smearing parameter  $\eta$  and allows for faster convergence with respect to the integration grid. The Debye-Waller matrix elements are computed within the rigid-ion approximation, which avoids the evaluation of the second-order potential response. Self-energy calculations are MPI parallelized over both electron ( $m$ ) and phonon ( $\nu$ ) bands and  $\mathbf{k}$ -points. Thanks to the Wannier-Fourier interpolation, the electron wavevector  $\mathbf{k}$  is not restricted to the grid used in the underlying calculation of the electronic structure. In particular,  $\mathbf{k}$  can be set to be a high-symmetry path or the locations of band extrema. The single-particle energies  $\epsilon$  can come from either KS, hybrid functional, or *GW* calculations. In Eqs. (36) and (37) the quasi-elastic approximation is considered for the coupling parameters  $\lambda_{\nu\mathbf{q}}$  and  $\lambda_{n\mathbf{k}}$ , *i.e.*, the phonon energies are assumed to be much smaller than the typical electron energies, and the difference between phonon absorption and emission is neglected. **exciting**, however, also implements the coupling parameters for either absorption or emission processes.

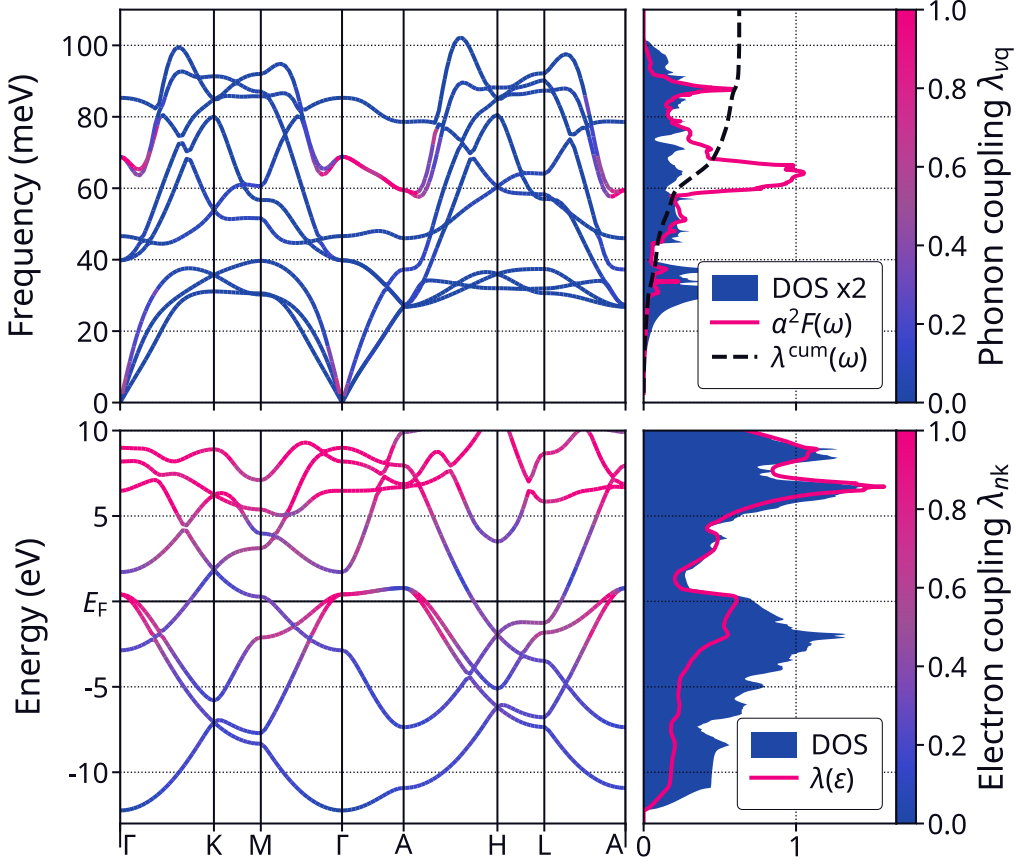


Figure 4: Electron-phonon coupling in MgB<sub>2</sub>. Top: Phonon dispersion and mode resolved coupling strength  $\lambda_{\nu\mathbf{q}}$  together with the phonon DOS (blue), the Eliashberg function  $\alpha^2F$  (magenta), and the cumulative coupling strength  $\lambda^{\text{cum}}$  (dashed line). Bottom: Electron dispersion and band-resolved coupling strength  $\lambda_{n\mathbf{k}}$  together with the electron DOS (blue) and coupling strength  $\lambda$  (magenta).

We demonstrate our implementations by calculating phonons and EPC for the high- $T_c$  superconductor MgB<sub>2</sub>, an intensively studied material. In the left panel of Fig. 4, we show the phonon dispersion as obtained with DFPT and the mode-resolved coupling strength  $\lambda_{\nu\mathbf{q}}$ . Mainly the  $E_{2g}$  modes along the  $\Gamma$ -A line show a strong coupling strength, which results in a clear peak between 60 meV to 70 meV in the Eliashberg function, which does not appear in the phonon DOS. The cumulative coupling strength

$$\lambda^{\text{cum}}(\omega) = 2 \int_0^\omega \frac{d\omega'}{\omega'} \alpha^2 F(\omega') \quad (38)$$

reaches a maximum value of  $\lambda = 0.63$ . The right panel of Fig. 4 shows the electron dispersion with the band-resolved coupling strength  $\lambda_{n\mathbf{k}}$  as well as the electron DOS, and the integrated energy-dependent EPC strength  $\lambda(\epsilon)$ . At the Fermi level, its value is 0.63, the same as obtained from the Eliashberg function. The band-resolved coupling strength near the Fermi level shows that the mass-enhancement parameter for the  $\sigma$ -bonding bands reaches values between 0.8 and 1.1, *i.e.*, more than twice as big as the values between 0.3 and 0.4 for the  $\pi$ -bonding bands. All these findings are consistent previously published results [112].

As a second example, we calculate for diamond the temperature-dependent QP energies from the electron self-energy. Phonons and the potential response are computed with PBE, electron eigenvalues and wavefunctions with the hybrid functional HSE, demonstrating the possibility to use different starting points such as gDFT or *GW* for the energy renormalization due to EPC. In Fig. 5 we present the resulting direct and indirect band gap and its EPC-based renormalization as a function of temperature as well as the electron spectral function at room temperature. The base HSE results for the direct (indirect) band gap are 7.01 eV (5.32 eV) and a ZPR of  $-352$  meV ( $-295$  meV).

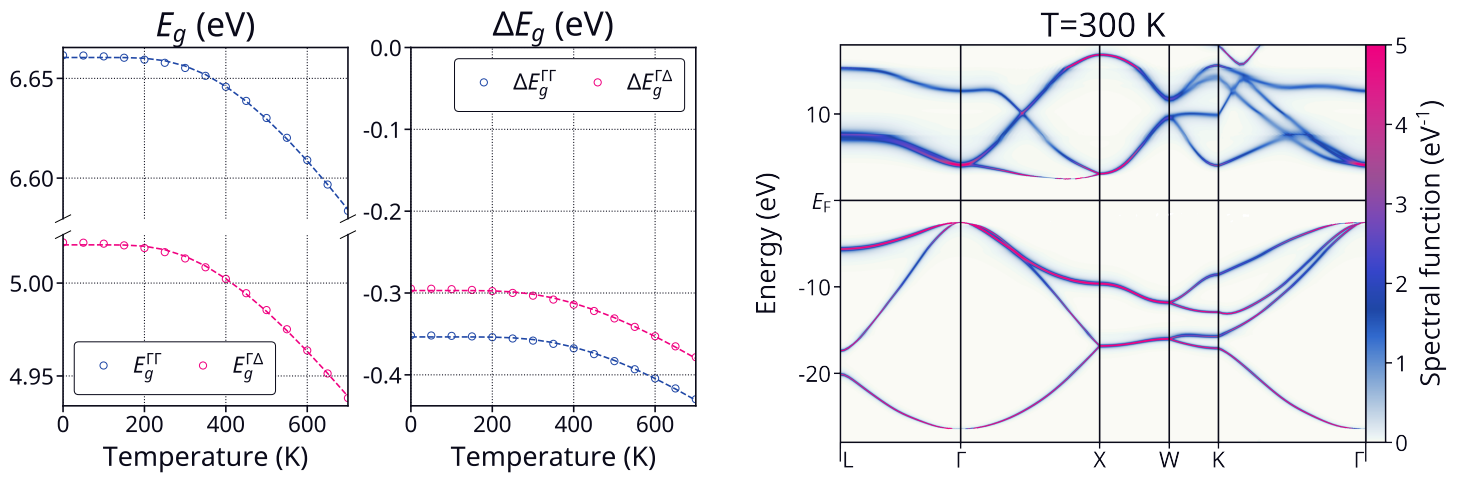


Figure 5: Electron-phonon coupling in diamond. Left: Direct (blue) and indirect (magenta) band gap  $E_g(T)$  and its renormalization  $\Delta E_g(T) = E_g(T) - E_g^{\text{DFT}}$  as a function of temperature. Right: Band structure with the color code indicating the electron spectral function at 300 K.

## 5 GW

### 5.1 State of the art

While KS-DFT is designed to exactly reproduce GS densities and energies, it is not designed to predict excited-state properties. In particular, the KS eigenvalues, which were introduced as Lagrange multipliers, cannot be interpreted as QP energies. Although they often provide a reasonable first approximation [13, 113], they can differ significantly from the true many-body spectrum [61, 114–117]. Hybrid functionals partially remedy these discrepancies, however, charged excitations cannot be captured by a single DFT calculation with a fixed particle number. An accurate description requires MBPT, and in particular, the self-consistent solution of Hedin’s equations [8]. They account for the non-local and dynamical screening effects induced by electron addition and removal, thereby providing a direct connection to experiments such as X-ray photoelectron spectroscopy (XPS) or angle-resolved photoemission spectroscopy (ARPES).

An approach to reduce this set of equations to a more tractable problem is the so-called *GW* approximation. The name comes from the form assumed by the self-energy operator,  $\Sigma = iGW$ , where  $G$  is the single-particle Green’s function and  $W$  is the screened Coulomb interaction. The *GW* approximation is obtained by approximating the vertex function as  $\Gamma \approx 1$ . The most common and computationally affordable implementation of the *GW* approximation is the *single-shot GW* or  $G_0W_0$  approach. In this scheme, the self-energy is computed perturbatively, starting from a preceding DFT, HF, or hybrid-functional calculation.  $G_0W_0$  has been widely implemented across a variety of codes, such as Abinit [118, 119], **exciting** [21], VASP [120–122], GPAW [123], FLAPWMBPT [124], Yambo [125, 126], BerkeleyGW [127], CP2K [128, 129], and FHI-aims [130]. The wide variety of existing implementations differ in the usage of basis functions, different frequency-integration schemes, etc. This makes cross-validation challenging. A recent study [131] has shown that for a selection of seven materials, the  $G_0W_0$  band gaps obtained from four different codes, *i.e.*, Abinit, **exciting**, FHI-aims, and GPAW agree within 0.1 eV, with the two all-electron codes showing the best agreement and consistency among each other.

The perturbative nature of the  $G_0W_0$  approximation introduces an undesirable dependence on the mean-field starting point [72, 132–138]. Addressing this limitation has driven intense research efforts towards self-consistent *GW* schemes [33, 139–144]. They often result in an overestimation of band gaps, due to the neglect of vertex corrections and thus under-screening. Vertex effects can be included to some extent via the cumulant approach, improving the description of plasmonic satellites [145–148], even if the full vertex is required for an accurate spectral representation [149]. While diagrammatic approaches can incorporate the vertex explicitly [150, 151], a more practical strategy is to include electron-hole interaction effects via an xc kernel into the polarizability and self-energy. The quality of this approach has been shown to depend critically on the kernel [152, 153], which must capture both the correct long-range behavior to describe exciton binding and energy gaps [152–159] and the proper short-range behavior to ensure accurate QP energies and ionization potentials [152, 153, 159, 160]. Notably, renormalization of the electronic structure by EPC, *i.e.*, zero-point vibrations and temperature effects [161, 162], is crucial for quantitative comparison with experiment. Also lattice screening plays a role in polar materials [163, 164].

Achieving reliable precision requires addressing critical numerical bottlenecks. A major problem here is the sensitivity of excited-state properties to the quality and completeness of the basis set, in particular in LAPW+LO methods [21, 165]. To mitigate this issue, an incomplete basis set correction (IBC) has been proposed [166]. Furthermore, the treatment of long-range interactions in the  $\mathbf{q} \rightarrow 0$  limit is critical, particularly for anisotropic or low-dimensional materials where standard expressions fail [136, 167, 168]. To ensure numerical accuracy across diverse systems, code-agnostic libraries such as **GreenX** [169, 170] have been developed to rigorously treat the  $\mathbf{q} \rightarrow 0$  limit [167, 168]. The practical application of advanced *GW* methods is often limited by the inherent quartic scaling with the number of atoms. This bottleneck has been addressed through algorithmic improvements like the space-time method, leading to cubic scaling [171–174] or linear-scaling stochastic *GW* [175, 176]. For weakly bound van der Waals heterostructures, the expansion addition screening (EAS) method [177–179] has been proven to be efficient.

By approximating the total polarizability of the heterostructure as a superposition of its individual components, the computing time for interfaces between organic molecular layers and 2D substrates has been reduced by over 50% [179].

## 5.2 Methodology

The essence of the  $GW$  method and the many variants has already been sketched in Section 5.1. Some aspects will be summarized when describing the implementation of  $GW$  into `exciting` in Section 5.3. Providing more details on the entire formalism would go beyond the scope of this article. Instead, we refer to review articles and books [13, 116] and the specialized literature.

## 5.3 Implementation in `exciting`

The current implementation of the  $GW$  method in the `exciting` code, to a large extent based on the approach of Ref. [180], is described in detail in Ref. [181]. Here, we briefly summarize the main aspects. Starting from a DFT or gDFT reference, the QP energies are obtained from the linearized QP equation:

$$\Re[\epsilon_{n\mathbf{k}}^{\text{QP}}] \approx \epsilon_{n\mathbf{k}} + Z_{n\mathbf{k}} \langle \psi_{n\mathbf{k}} | \Re[\Sigma(\mathbf{r}, \mathbf{r}', \epsilon_{n\mathbf{k}})] - v_{\text{XC}}(\mathbf{r}) \delta(\mathbf{r} - \mathbf{r}') | \psi_{n\mathbf{k}} \rangle, \quad (39)$$

where  $\epsilon_{n\mathbf{k}}$  and  $\psi_{n\mathbf{k}}$  are the KS eigenvalues and wavefunctions,  $v_{\text{XC}}(\mathbf{r})$  is the exchange-correlation potential of the reference calculation, and  $Z_{n\mathbf{k}}$  is the QPrenormalization factor.

Single-particle states are represented using the all-electron LAPW+LO basis, while two-particle quantities such as the polarizability and dielectric function are expanded in an auxiliary mixed-product basis [180, 182]. Products of KS states are expressed as

$$\psi_{n\mathbf{k}}(\mathbf{r}) \psi_{m\mathbf{k}-\mathbf{q}}^*(\mathbf{r}) = \sum_i M_{nm}^i(\mathbf{k}, \mathbf{q}) \mathcal{B}_i^{\mathbf{q}}(\mathbf{r}), \quad (40)$$

where  $\mathcal{B}_i^{\mathbf{q}}(\mathbf{r})$  are the mixed-product basis functions and  $M_{nm}^i(\mathbf{k}, \mathbf{q})$  are the corresponding expansion coefficients. Computing these coefficients represents one of the main computational bottlenecks of the method. Expanded within the mixed-product basis, the RPA dielectric matrix reads

$$\begin{aligned} \varepsilon_{ij}(\mathbf{q}, \omega) = 1 - \frac{2}{N_{\mathbf{k}}} \sum_{nm\mathbf{k}} f_{n\mathbf{k}} (1 - f_{m\mathbf{k}-\mathbf{q}}) \tilde{M}_{nm}^i(\mathbf{k}, \mathbf{q}) [\tilde{M}_{nm}^j(\mathbf{k}, \mathbf{q})]^* \\ \times \left[ \frac{1}{\omega - (\epsilon_{m\mathbf{k}-\mathbf{q}} - \epsilon_{n\mathbf{k}}) + i\eta} - \frac{1}{\omega + (\epsilon_{m\mathbf{k}-\mathbf{q}} - \epsilon_{n\mathbf{k}}) - i\eta} \right], \end{aligned} \quad (41)$$

where  $f_{n\mathbf{k}}$  are occupation numbers,  $\eta$  is a positive infinitesimal,  $N_{\mathbf{k}}$  denotes the number of  $\mathbf{k}$  points, and

$$\tilde{M}_{nm}^i(\mathbf{k}, \mathbf{q}) = \sum_l v_{il}^{\frac{1}{2}}(\mathbf{q}) M_{nm}^l(\mathbf{k}, \mathbf{q}); \quad (42)$$

with  $v_{ij}(\mathbf{q})$  being the bare Coulomb interaction expanded in the mixed-product basis. All quantities are transformed to the  $v_{ij}(\mathbf{q})$  eigenbasis to isolate the long-range  $\mathbf{q} \rightarrow 0$  behavior. This properly addresses the long-range limit while enabling an efficient truncation of the dielectric matrix to reduce computational cost.

The screened Coulomb interaction is then obtained as

$$\mathcal{W}(\mathbf{q}, \omega) = \varepsilon^{-1}(\mathbf{q}, \omega) v(\mathbf{q}). \quad (43)$$

Using  $\mathcal{W}$ , the correlation part of the self-energy is given by

$$\Sigma_{nl\mathbf{k}}^c(\omega) = \frac{1}{N_{\mathbf{q}}} \sum_{\mathbf{q}} \sum_m \frac{i}{2\pi} \int_{-\infty}^{\infty} d\omega' \frac{\sum_{ij} [M_{nm}^i(\mathbf{k}, \mathbf{q})]^* \mathcal{W}_{ij}^c(\mathbf{q}, \omega') M_{lm}^j(\mathbf{k}, \mathbf{q})}{\omega + \omega' - \varepsilon_{m\mathbf{k}-\mathbf{q}}}, \quad (44)$$

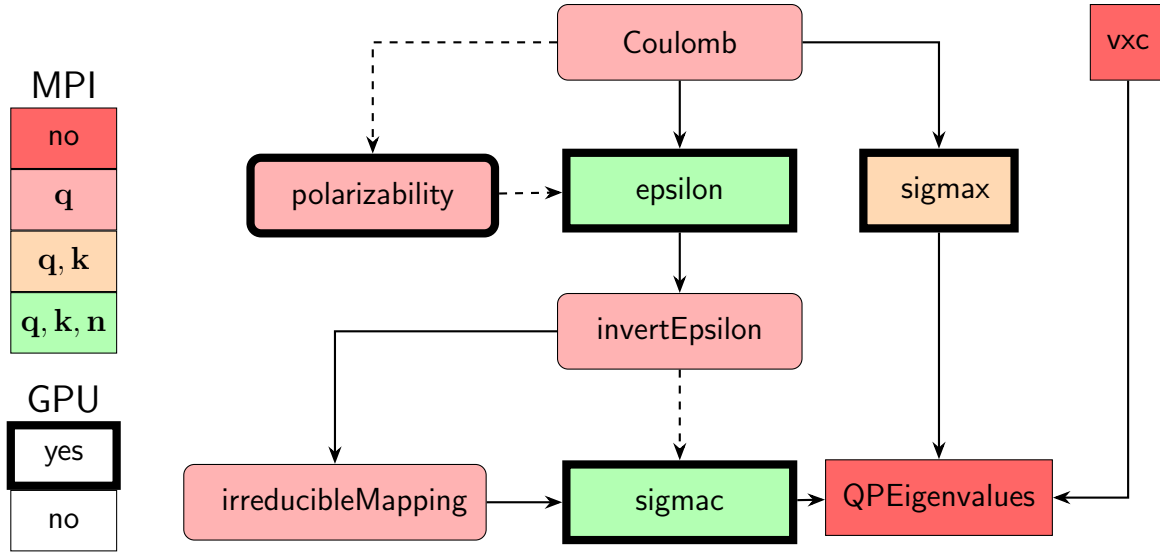


Figure 6: Workflow diagram illustrating the tasks required for a  $GW$  calculation. Color coding denotes MPI parallelization over  $\mathbf{q}$ points,  $\mathbf{k}$ points, and unoccupied states ( $n$ ). Tasks with thick outlines support GPU acceleration. Solid arrows represent the preferred workflow, whereas dashed arrows indicate non-recommended alternatives. The **Coulomb** task evaluates the bare Coulomb interaction, and **vxc** provides the diagonal matrix elements of the exchange-correlation potential. The **polarizability** task constructs the irreducible polarizability, which is then used by **epsilon** to form the dielectric matrix within the RPA. Its inversion is carried out by **invertEpsilon**, followed by **irreducibleMapping**, which exploits crystal symmetries to reconstruct the inverse dielectric matrix over the full BZ from the irreducible one in case crystal symmetry was used in **epsilon**. The self-energy is separated into exchange and correlation contributions, evaluated by **sigmax** and **sigmac**, respectively. Finally, **QPEigenvalues** combines these components to obtain the QP energies.

where  $\mathcal{W}_{ij}^c(\mathbf{q}, \omega) = \mathcal{W}_{ij}(\mathbf{q}, \omega) - v_{ij}(\mathbf{q})$ . The exchange contribution is evaluated as

$$\Sigma_{nlk}^x = -\frac{1}{N_{\mathbf{q}}} \sum_{\mathbf{q}} \sum_{i,j}^{\text{occ}} \sum_m \left[ \tilde{M}_{nm}^i(\mathbf{k}, \mathbf{q}) \right]^* \tilde{M}_{lm}^j(\mathbf{k}, \mathbf{q}). \quad (45)$$

The total self-energy,  $\Sigma = \Sigma^x + \Sigma^c$ , is then used in Eq. (39) to compute the QP energies.

The implementation follows a task-based workflow with symmetry reduction, multi-level MPI parallelism and GPU offloading (see Section 5.4 for further information). This approach allows for scalable all-electron  $G_0W_0$  calculations for both bulk and low-dimensional systems. Moreover, the task-based formalism naturally extends to several flavors of self-consistent  $GW$  schemes and enables seamless integration with the EAS for treating van-der-Waals (vdW) stackings. Further details of the current implementation are provided in Section 5.7.

## 5.4 Computational advancements: HPC-friendly $G_0W_0$

While the implementation based on Ref. [180] allowed for some parallelization, it offered limited scalability and lacked GPU support, hindering efficient use of modern supercomputers. The recent version introduced a new HPC-optimized  $GW$  implementation based on a task-based workflow in which each task allows for parallelism not only over  $\mathbf{k}/\mathbf{q}$ -points but also over bands and frequencies. This leads to substantial improvements in both strong and weak scaling. To further mitigate computational bottlenecks, GPU acceleration has been incorporated via a hybrid strategy: linear algebra operations are offloaded to vendor-optimized libraries, while compute-intensive loops are parallelized using portable, *i.e.*, OpenMP offload. This approach achieves 4–10 $\times$  speedups across a variety of systems and workloads, enabling large-scale, high-precision  $GW$  calculations that fully leverage modern HPC resources. In Fig. 6, we present a schematic overview of the general workflow of the new implementation. Details on this implementation are provided in Ref. [181].

## 5.5 Accurate treatment of long-range interactions

As previously noted, the computation of the self-energy operator  $\Sigma$  requires an integration over the BZ, which converges too slowly due to the long-range nature of the Coulomb interaction. Several techniques have been developed to mitigate this issue, including the use of auxiliary functions [183], Monte Carlo strategies [125, 184], Coulomb-truncation schemes [185, 186], among others. Most of these approaches—except for truncation-based methods—face the nontrivial challenge of assigning a well-defined value to the inverse dielectric matrix and/or the screened Coulomb potential at  $\mathbf{q} = 0$ . Methods that avoid this issue typically do so at the expense of introducing an additional external parameter, such as a truncation cutoff, which must be carefully chosen and converged [185]. This difficulty arises from the non-analytic behavior of these quantities, which are in general—except for cubic Bravais lattices—not properly defined at  $\mathbf{q} = 0$  but rather in the limit  $\mathbf{q} \rightarrow 0$  [187, 188].

This ambiguity complicates the application of convergence-acceleration techniques, particularly for 2D materials. To address this, Rasmussen *et al.* [168] employed Coulomb-cutoff methods to derive expressions with the proper 2D  $\mathbf{q} \rightarrow 0$  limit for the screened Coulomb potential and proposed a BZ integration scheme that combines numerical and isotropic analytical contributions. This approach ensures a physically consistent determination of the  $\mathbf{q} = 0$  limit and accelerates the convergence of the  $\mathbf{q}$ -mesh by roughly a factor of three [168, 189] (see Fig. 7). This methodology has been implemented in `exciting` [189], enabling efficient *GW* calculations for low-dimensional materials such as MoS<sub>2</sub> [136]. For anisotropic sys-

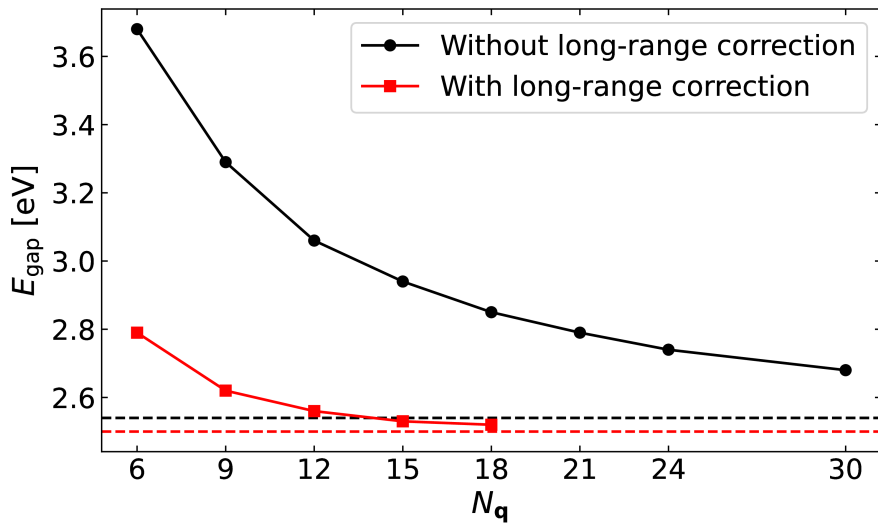


Figure 7: Direct band gap at the K point of MoS<sub>2</sub> for different  $\mathbf{q}$ -point grids,  $N_q \times N_q \times 1$ . The values are obtained with (red) and without (black) considering corrections for the long-range contribution. Dashed lines indicate extrapolation to the infinitely dense meshes.

tems, `exciting` is interfaced with the code-agnostic library `IDieL` [169, 170], which enables an accurate and parameter-free evaluation of the  $\mathbf{q} \rightarrow 0$  limit. This library implements the formalism suggested in Ref. [167], in which the dielectric matrix is averaged over a scaled-down  $\Gamma$ -centered BZ using a spherical expansion of the head and body, with Lebedev grids for angular integration.

For example, the inverse of the head element can be written as

$$\varepsilon_{00}^{-1}(\mathbf{0}) = \frac{1}{\Omega} \int_S d\hat{\mathbf{q}} \frac{1}{\hat{\mathbf{q}} \cdot \mathbf{L} \cdot \hat{\mathbf{q}}} \int_0^{q_{\max}(\hat{\mathbf{q}})} dq q^2, \quad (46)$$

where  $\mathbf{L}$  is the macroscopic dielectric matrix including local-field effects. The angular integral over  $\hat{\mathbf{q}}$  can be efficiently evaluated using a spherical harmonic expansion, which separates the expression into two terms to accelerate convergence:

$$\varepsilon_{00}^{-1}(0) \sim \sum_{l=0}^{41} [l \bmod 2 = 0] \sum_{m=-l}^l c_{lm} \underbrace{\frac{1}{\Omega_{\Gamma_{\text{BZ}}}} \int d\hat{\mathbf{q}} Y_{lm}(\hat{\mathbf{q}}) \int_0^{q_{\max}(\hat{\mathbf{q}})} dq q^2}_{\text{geometry term}}, \quad (47)$$

$$c_{lm} = \underbrace{\int d\hat{\mathbf{q}} [Y_{lm}(\hat{\mathbf{q}})]^* \frac{1}{\hat{\mathbf{q}} \cdot \mathbf{L} \cdot \hat{\mathbf{q}}}}_{\text{fast-converging term}}, \quad (48)$$

where  $\Omega_{\Gamma_{\text{BZ}}}$  is the volume of the scaled-down  $\Gamma$ -centered BZ.

The *geometry term* converges slowly because the integration domain is a parallelepiped, requiring a high  $l_{\max}$  (at least 131) for accurate results. However, it can be precomputed for all angles and contributions (head, wings, and body). The *fast-converging term*, which depends on the dielectric matrix, requires only a few terms. A similar approach, using circular expansions and cubic splines, generalizes the method by Rasmussen et al. [168] to fully anisotropic systems, ensuring an accurate and efficient evaluation of the  $\mathbf{q} \rightarrow 0$  limit.

The effect of this anisotropic treatment on QP energies is illustrated in Fig. 8, which compares the band gaps computed with and without the anisotropic  $\mathbf{q} \rightarrow 0$  approach. Including the full anisotropy removes the need to select specific directions, eliminating errors associated with free parameters. It can also be seen that for isotropic materials, the results reproduce those of the isotropic approach, as expected.

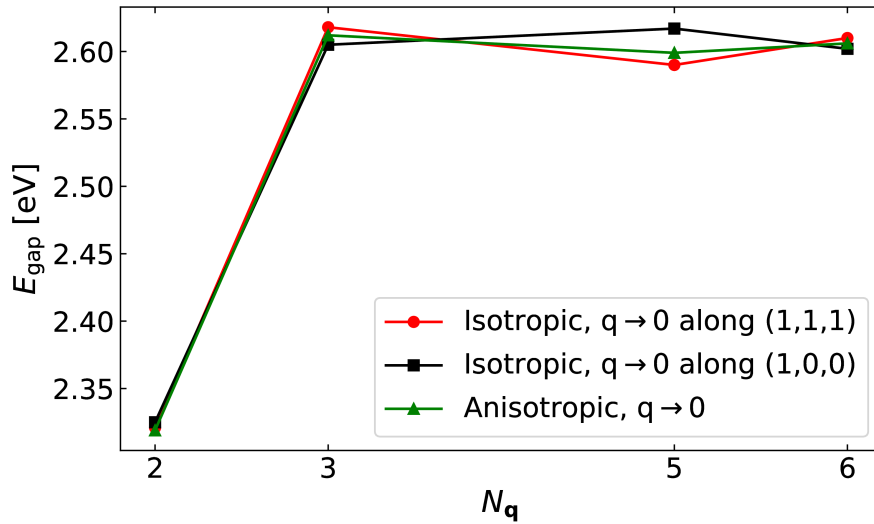


Figure 8: QP gap at  $\Gamma$  of black phosphorus for different  $\mathbf{q}$ -point grids ( $2 \times 2 \times 2$ ,  $3 \times 3 \times 4$ ,  $5 \times 5 \times 6$ , and  $6 \times 6 \times 8$ ), comparing the isotropic approach for different directions for the  $\mathbf{q} \rightarrow 0$  limit to the anisotropic formalism. All calculations performed with `exciting` and the `IDieL` library.

## 5.6 Beyond the One-Shot Approximation

As noted, one of the main drawbacks of the one-shot  $GW$  approach is its starting-point dependence. This limitation can be overcome by self-consistency. Among the various self-consistent  $GW$  schemes, one of the most widely used is the quasiparticle self-consistent  $GW$  (QSGW) method [33, 140, 141]. The central idea of QSGW is to replace the dynamical, energy-dependent self-energy  $\Sigma(\mathbf{r}, \mathbf{r}', \omega)$  with an optimal static, non-local xc potential  $v_{xc}^{\text{opt}}$  that best represents the quasiparticle excitations. This potential is constructed such that the independent-particle Green's function  $G_0$ , generated from  $v_{xc}^{\text{opt}}$ , approximates the fully interacting Green's function  $G$  as closely as possible at the QP level. Within this framework,

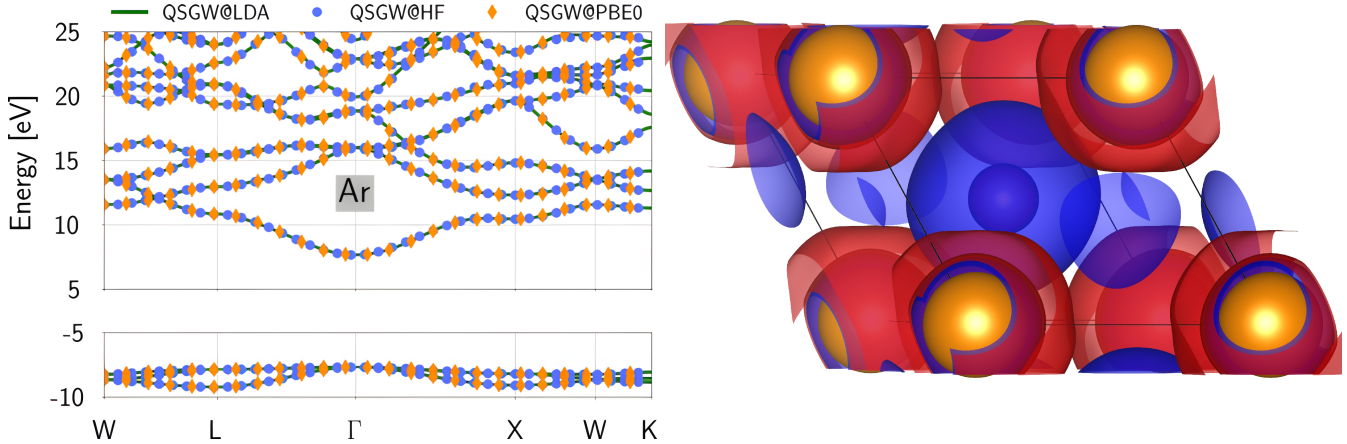


Figure 9: Left: QSGW bandstructures of Ar obtained with different starting points: LDA (solid-green line), HF (purple circles), and PBE0 (orange diamonds). Right: Charge-density difference in CaO between QSGW and LDA results at an isovalue of  $\pm 1.5 \times 10^{-3} \text{ e a}_0^{-3}$ . Positive values are indicated in red, negative ones in blue. Orange and white spheres depict calcium and oxygen atoms, respectively. Plots adapted from Ref. [33].(copyright American Physical Society).

the optimized xc potential is defined as [141]:

$$v_{xc}^{\text{opt}}(\mathbf{k}) = \frac{1}{2} \sum_{nl} |\psi_{n\mathbf{k}}\rangle [\Re(\Sigma_{nl\mathbf{k}}(\epsilon_{n\mathbf{k}})) + \Re(\Sigma_{nl\mathbf{k}}(\epsilon_{l\mathbf{k}}))] \langle \psi_{l\mathbf{k}}|. \quad (49)$$

This formalism is implemented in `exciting` [33], showing that both the starting-point dependence can be overcome and a more physically meaningful GS electronic density can be obtained. Both are demonstrated in Fig. 9. A careful analysis of the charge-density redistribution reveals that it systematically reduces the delocalization error inherent of semilocal xc functionals [114].

Finally, we emphasize the importance of the all-electron nature of `exciting` in this context. By treating valence, semicore, and core states on equal footing, the method accurately captures core-valence exchange and correlation contributions to the self-energy. In contrast, neglecting these contributions, as is common in pseudopotential-based approaches, is already a source of error in  $G_0W_0$  calculations [190, 191], and self-consistent iterations can further amplify this error, potentially leading to larger biases in QP energies and charge distributions, particularly in materials where semicore or core states play an active role.

## 5.7 Computational advancements: expansion and addition screening

The computational cost of calculating the non-interacting polarizability represents a major bottleneck in both  $G_0W_0$  and BSE calculations, scaling as  $\mathcal{O}(N_{\text{at}}^4)$  with the number of atoms  $N_{\text{at}}$  in the unit cell. This challenge becomes particularly severe for heterostructures and interface systems, which typically require large supercells compared to the individual components. To address this, we have implemented the EAS approach, extending the formalism originally developed for plane-wave basis sets [177, 178] to the mixed-product basis [179]. The key idea of the EAS is an additive ansatz, *i.e.*, the polarizability of the heterostructure is obtained by summing the contributions of the individual components. This comes with the advantage that the polarizability of the supercell of a constituent does not need to be computed for that supercell but instead can be obtained from the respective unit cell by a folding (expansion) procedure.

Our implementation of this formalism in the `exciting` code [179], advances beyond the original formulation by two key aspects. First, we have developed the necessary transformations for the mixed-product basis used in the LAPW method, accounting for the dual representation in MT spheres and interstitial regions. Second, we have extended the EAS to optical excitations within BSE (Section 6), where the polarizability plays an analogous role in screening the electron-hole interaction. We refer the reader to Ref. [179] for a full account of the implementation details.

The EAS is ideally suited for weakly bound vdW heterostructures where covalent interactions are negligible [192–194], allowing to separate the system in two distinct components. Fig. 10 summarizes the computational savings reported in Ref. [179] for an organic/inorganic hybrid material, formed by  $\text{MoS}_2$  and a monolayer of pyridine. The EAS reduces the computation time for the polarizability by 56% for  $G_0W_0$  and 69% for BSE, resulting in total speedups of 25% and 46%, respectively. In the context of BSE, the combination of EAS with the interpolative separable density fitting (ISDF) method [195] (see Section 6.3) represents a most efficient framework.

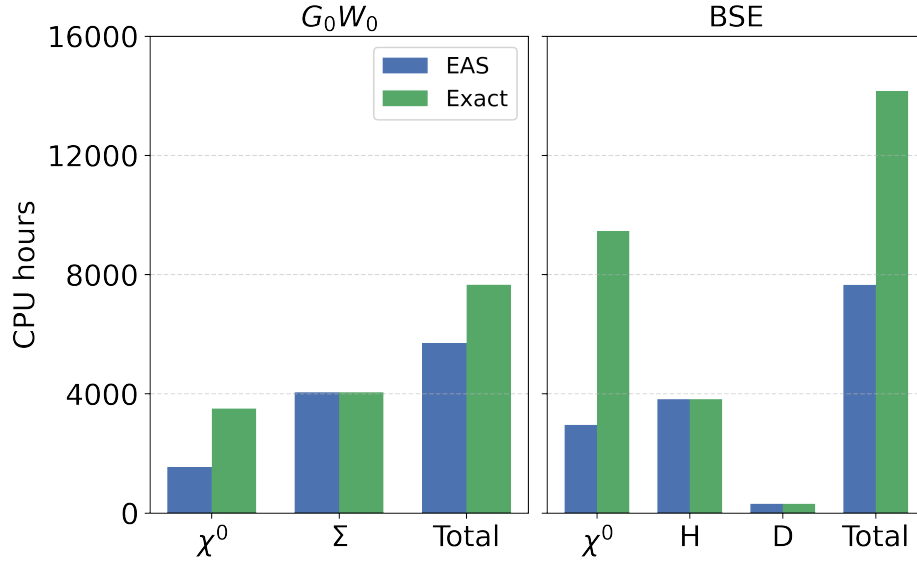


Figure 10: Computational effort for  $G_0W_0$  (left) and BSE (right) calculations of pyridine@ $\text{MoS}_2$  using the EAS method (blue) versus the exact calculations (green). The breakdown shows CPU hours for different computational steps: polarizability ( $\chi^0$ ), self-energy ( $\Sigma$ ), Hamiltonian set up (H), and diagonalization (D)

## 6 Bethe-Salpeter equation

### 6.1 State of the art

Excitonic effects have clear signatures in absorption spectra. A systematic method of including such two-body interactions is given by the BSE [9–12]. Using the results of a DFT or *GW* calculation as a starting point [14, 15], the BSE became the work horse of theoretical spectroscopy [13]. Solving the BSE is, however, still computationally demanding. The central task involves the construction and diagonalization of the Bethe-Salpeter Hamiltonian (BSH) in the basis of electronic transitions between occupied and unoccupied states. Owing to the two-body nature of the electron–hole interaction, the Hamiltonian contains dense off-diagonal couplings, and achieving quantitative convergence typically requires a dense sampling of the BZ. Together, these factors lead to the generation of very large Hamiltonian matrices and, consequently, to high computational cost [13, 15, 22, 196]. Significant progress has been achieved by expressing the interaction kernels using interpolative separable density fitting (ISDF) and combining this representation with an iterative Lanczos solver, which has been shown to substantially accelerate both matrix construction and spectral calculations [35, 195, 197, 198].

Beyond algorithmic advances, recent work has increasingly focused on extending the BSE formalism itself. In particular, going beyond the widely adopted approximation of static screening has emerged as an important direction, as dynamical screening effects are required to capture frequency-dependent correlations and can significantly improve the description of excitation energies and spectral features in a range of materials [199, 200]. At the same time, extensions of the BSE framework have enabled access to magnetic excitations, with magnonic signatures encoded in electron–hole transitions allowing for the description of spin-flip processes and collective spin modes [201]. These developments highlight the versatility of generalized BSE approaches in describing a broader class of collective excitations beyond conventional excitonic physics.

The BSE has also been successfully applied to non-equilibrium situations. By combining RT-TDDFT simulations with subsequent BSE calculations, it has become possible to model spectroscopic responses of systems driven out of equilibrium by external perturbations [202, 203], including pump-probe spectroscopy [89, 90, 204] (see Section 8). In addition, BSE-based methods have been extended to the theoretical description of resonant inelastic x-ray scattering (RIXS). These applications require an accurate treatment of core-level excitations and their coupling to valence states, posing both conceptual and computational challenges within the many-body framework [36, 205, 206].

Another emerging area of research concerns the coupling between excitonic states and lattice vibrations [207–211]. For example, phonon-mediated screening impact exciton binding energies and spectral features in polar materials [210, 211]. A consistent treatment of exciton-phonon coupling (EXPC) further gives rise to phenomena such as self-trapped exciton (STE) and excitonic polarons, which have been observed in a variety of materials [212–215].

### 6.2 Methodology

In practice, the solution of the BSE is reformulated as an effective two-particle Schrödinger equation. The corresponding two-particle wavefunction is expanded in a transition basis constructed from products of single-particle wavefunctions of the form

$$\psi_{o\mathbf{k}_+}(\mathbf{r})\psi_{u\mathbf{k}_-}(\mathbf{r}'), \quad (50)$$

$$\psi_{u(-\mathbf{k}_-)}(\mathbf{r})\psi_{o(-\mathbf{k}_+)}(\mathbf{r}'), \quad (51)$$

where *o* and *u* label occupied and unoccupied electronic states, respectively, and  $\mathbf{k}$  denotes a BZ wavevector. The single-particle wavefunction  $\psi_{i\mathbf{k}}(\mathbf{r})$  corresponds to electronic state *i* at crystal momentum  $\mathbf{k}$  and position  $\mathbf{r}$ . The shifted wavevectors are defined as  $\mathbf{k}_\pm = \mathbf{k} \pm \mathbf{q}/2$ , where  $\mathbf{q}$  is the momentum transfer. Eq. (50) describes resonant (excitation) transitions, while Eq. (51) corresponds to anti-resonant (de-excitation) transitions. Using this transition basis, solving the BSE is equivalent to solving the eigen-

value problem of an effective Hamiltonian of the form

$$H^{\text{BSE}}(\mathbf{q}) = \begin{pmatrix} A(\mathbf{q}) & B(\mathbf{q}) \\ -B(\mathbf{q}) & -A(\mathbf{q}) \end{pmatrix}.$$

The diagonal and off-diagonal blocks are given by

$$A_{ou\mathbf{k}, o'u'\mathbf{k}'}(\mathbf{q}) = D_{ou\mathbf{k}, o'u'\mathbf{k}'}(\mathbf{q}) + \gamma_x V_{ou\mathbf{k}, o'u'\mathbf{k}'}(\mathbf{q}) - W_{ou\mathbf{k}, o'u'\mathbf{k}'}(\mathbf{q}), \quad (52)$$

$$B_{ou\mathbf{k}, o'u'\mathbf{k}'}(\mathbf{q}) = \gamma_x V_{ou\mathbf{k}, o'u'\mathbf{k}'}(\mathbf{q}) - W_{ou\mathbf{k}, o'u'\mathbf{k}'}(\mathbf{q}), \quad (53)$$

where  $D$  denotes the diagonal (independent-particle) term,  $V$  the exchange interaction, and  $W$  the screened direct interaction. The factor  $\gamma_x$  allows to distinguish between spin singlet ( $\gamma_x = 2$ ) and spin triplet ( $\gamma_x = 0$ ) excitations. If the screened Coulomb interaction  $W$  is neglected, the resulting eigenvalue problem reduces to RPA.

A widely used approximation that substantially reduces the computational complexity of the problem is the Tamm-Dancoff approximation (TDA) [13]. In this approximation, the coupling between resonant and anti-resonant transitions is neglected, such that the off-diagonal block satisfies  $B(\mathbf{q}) \approx 0$ . As a result, the BSH becomes block diagonal, and the problem reduces to the diagonalization of the matrix  $A(\mathbf{q})$  alone. In this case, the effective Hamiltonian is given by

$$H^{\text{TDA}}(\mathbf{q}) = A(\mathbf{q}). \quad (54)$$

For simplicity, the Tamm-Dancoff approximation (TDA) is assumed throughout the following discussion. Nevertheless, the `exciting` code is capable of going beyond the TDA and explicitly accounting for the coupling terms when required [22].

The diagonal term is given by the energy differences between the participating occupied and unoccupied electronic states,

$$D_{ou\mathbf{k}, o'u'\mathbf{k}'}(\mathbf{q}) = [\epsilon_{u\mathbf{k}_-} - \epsilon_{o\mathbf{k}_+}] \delta_{oo'} \delta_{uu'} \delta_{\mathbf{k}\mathbf{k}'} . \quad (55)$$

Neglecting the interaction kernels altogether reduces the problem to the independent particle approximation (IPA), which is computationally efficient and widely used, but inherently incapable of capturing excitonic effects. The matrix elements of the exchange interaction are given by

$$V_{ou\mathbf{k}, o'u'\mathbf{k}'}(\mathbf{q}) = \frac{1}{N_{\mathbf{k}}^2} \iint_{\Omega \times \Omega} d\mathbf{r} d\mathbf{r}' \psi_{o\mathbf{k}_+}(\mathbf{r}) \psi_{u\mathbf{k}_-}^*(\mathbf{r}) v_C(\mathbf{r}, \mathbf{r}') \psi_{o'\mathbf{k}'_+}^*(\mathbf{r}') \psi_{u'\mathbf{k}'_-}(\mathbf{r}') , \quad (56)$$

where  $v_C(\mathbf{r}, \mathbf{r}')$  denotes the bare Coulomb interaction and  $\Omega$  is the volume of the unit cell. The matrix elements of the direct interaction are given by

$$\mathcal{W}_{ou\mathbf{k}, o'u'\mathbf{k}'}(\mathbf{q}) = \frac{1}{N_{\mathbf{k}}^2} \iint_{\Omega \times \Omega} d\mathbf{r} d\mathbf{r}' \psi_{o\mathbf{k}_+}(\mathbf{r}') \psi_{o'\mathbf{k}'_+}^*(\mathbf{r}') \mathcal{W}(\mathbf{r}, \mathbf{r}') \psi_{u\mathbf{k}_-}^*(\mathbf{r}) \psi_{u'\mathbf{k}'_-}(\mathbf{r}) , \quad (57)$$

where  $\mathcal{W}(\mathbf{r}, \mathbf{r}')$  denotes the statically screened Coulomb interaction. It is defined as

$$\mathcal{W}(\mathbf{r}, \mathbf{r}') = \int d\mathbf{r}'' v_C(\mathbf{r}, \mathbf{r}'') \varepsilon^{-1}(\mathbf{r}'', \mathbf{r}') . \quad (58)$$

with  $\varepsilon^{-1}$  being the inverse dielectric function.

The real-space integrals entering the exchange and direct interaction kernels can be evaluated efficiently in reciprocal space. In this representation, the matrix elements of the exchange and screened interactions take the form

$$V_{ou\mathbf{k}, o'u'\mathbf{k}'}(\mathbf{q}) = \sum_{\mathbf{G}} \hat{v}_{\mathbf{G}}(\mathbf{q}) M_{ou\mathbf{k}_-}^*(\mathbf{G}, \mathbf{q}) M_{o'u'\mathbf{k}'_-}(\mathbf{G}, \mathbf{q}) , \quad (59)$$

$$\mathcal{W}_{ou\mathbf{k}, o'u'\mathbf{k}'}(\mathbf{q}) = \sum_{\mathbf{G}, \mathbf{G}'} \hat{\mathcal{W}}_{\mathbf{G}\mathbf{G}'}(\mathbf{k} - \mathbf{k}') M_{o'\mathbf{k}'_+}^*(\mathbf{G}, \mathbf{k} - \mathbf{k}') M_{u'\mathbf{k}'_-}(\mathbf{G}', \mathbf{k} - \mathbf{k}') , \quad (60)$$

where the planewave matrix elements are defined as

$$M_{mnk}(\mathbf{G}, \mathbf{q}) = \langle n\mathbf{k} | e^{-i(\mathbf{G}+\mathbf{q})\mathbf{r}} | m(\mathbf{k}+\mathbf{q}) \rangle. \quad (61)$$

These matrix elements are computed within the LAPW+LO basis using single-particle states obtained from a GS calculation. The Fourier transforms of the bare and screened Coulomb interactions are given by

$$v_{\mathbf{G}}(\mathbf{q}) = \frac{1}{\Omega} \frac{4\pi}{|\mathbf{G} + \mathbf{q}|^2}, \quad (62)$$

$$\mathcal{W}_{\mathbf{G}, \mathbf{G}'}(\mathbf{q}) = v_{\mathbf{G}}(\mathbf{q}) \varepsilon_{\mathbf{G}\mathbf{G}'}^{-1}(\mathbf{q}, \omega = 0). \quad (63)$$

The dielectric matrix  $\varepsilon_{\mathbf{G}\mathbf{G}'}(\mathbf{q}, \omega)$  is evaluated within the random-phase approximation (RPA) [216] and reads

$$\varepsilon_{\mathbf{G}\mathbf{G}'}^{\text{RPA}}(\mathbf{q}, \omega) = \delta_{\mathbf{G}, \mathbf{G}'} - \frac{\hat{v}_{\mathbf{G}}(\mathbf{q})}{N_{\mathbf{k}}} \sum_{ijk} \frac{f_{j\mathbf{k}+\mathbf{q}} - f_{i\mathbf{k}}}{\epsilon_{j\mathbf{k}+\mathbf{q}} - \epsilon_{i\mathbf{k}} - \omega} M_{ijk}^*(\mathbf{G}, \mathbf{q}) M_{ijk}(\mathbf{G}', \mathbf{q}), \quad (64)$$

where  $f_{i\mathbf{k}}$  denotes the occupation of an electronic state with energy  $\epsilon_{i\mathbf{k}}$ .

### 6.3 Low-scaling BSE implementation

For complex materials, solving the BSE is a computationally demanding task and often not feasible in practice. This is particularly true when highly converged results with respect to the  $\mathbf{k}$ -grid are required, such as to obtain precise exciton binding energies. The construction of the BSE matrix scales as  $\mathcal{O}(N_o^2 N_u^2 N_k^2)$ , and solving the resulting eigenvalue problem scales as  $\mathcal{O}(N_o^3 N_u^3 N_k^3)$ , quickly becoming prohibitive with increasing system size. To reduce the computational complexity associated with computing the matrix elements, we approximate pair products of wavefunctions using the ISDF. Given a set of wavefunctions  $\psi_{i\mathbf{k}}(\mathbf{r})$ , where  $\mathbf{r}$  denotes points on a discrete real-space grid of size  $N_g$  for sampling the unit cell, any pair product can be approximated as an interpolation of the wavefunctions evaluated at a small number  $N_{\mu}$  of special interpolation points  $\psi_{i\mathbf{k}}(\mathbf{r}_{\mu}) \equiv u_{i\mathbf{k}}^{\mu}$  [197, 198]:

$$\psi_{i\mathbf{k}}^*(\mathbf{r}) \psi_{j\mathbf{k}'}(\mathbf{r}) \approx \sum_{\mu=1}^{N_{\mu}} \zeta_{\mu}(\mathbf{r}) \psi_{i\mathbf{k}}^*(\mathbf{r}_{\mu}) \psi_{j\mathbf{k}'}(\mathbf{r}_{\mu}), \quad (65)$$

where  $\zeta_{\mu}(\mathbf{r})$  are interpolation functions that can be computed efficiently. The interpolation points  $\{\mathbf{r}_{\mu}\}$  themselves are obtained efficiently using a centroidal Voronoi tessellation (CVT) [217]. By replacing the wavefunction pair products in Eq. (56) and Eq. (57) with the ISDF representation, the interaction kernels are reformulated such that they can be applied efficiently to a vector without explicitly constructing the full matrix. When combined with a Lanczos solver, this approach significantly reduces the overall computational scaling to  $\mathcal{O}(N_o N_u N_k \log N_k)$  [35, 195]. In Fig. 11, we demonstrate for the example of LiF that the new implementation in **exciting** reproduces the spectrum in perfect agreement with the direct approach, with improved scaling with respect to the number of  $\mathbf{k}$ -points. While in this simple example, the speedup is a factor of six, it can be even two orders of magnitude for larger Hamiltonians.

### 6.4 SVLO in the BSE

Precise BSE calculations require high-quality GS calculations as a starting point. This is particularly challenging for systems with strong SOC, where convergence typically requires a large number of unoccupied states,  $N_{\text{unocc}}$ . The SVLO basis, introduced in Section 3.6, achieves convergence of GS calculations with  $N_{\text{unocc}}$  reduced by orders of magnitude compared to the conventional SV basis. We extend this concept to BSE calculations by consistently implementing both planewave and momentum matrix elements in the SVLO basis. Fig. 12 illustrates the impact of the two basis sets on a representative BSE calculation by showing the exciton binding energy of  $\gamma\text{-CsPbI}_3$  as a function of  $N_{\text{unocc}}$ . The SVLO basis exhibits a substantially faster convergence, reaching the target accuracy with substantially fewer unoccupied states.

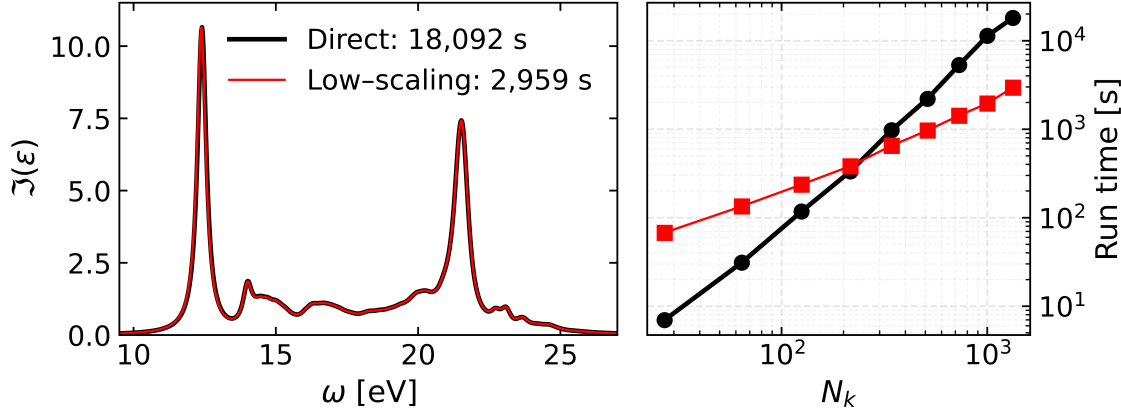


Figure 11: Left: Optical absorption spectrum of LiF on an  $11^3$   $\mathbf{k}$ -point grid obtained from the direct solution of the BSE (black) and from the ISDF–Lanczos BSE (red); the corresponding run times differ by a factor of 6. Right: Run time of the direct (black line, round markers) and ISDF–Lanczos BSE (red line, square markers) implementations as a function of the number of  $\mathbf{k}$ -points.

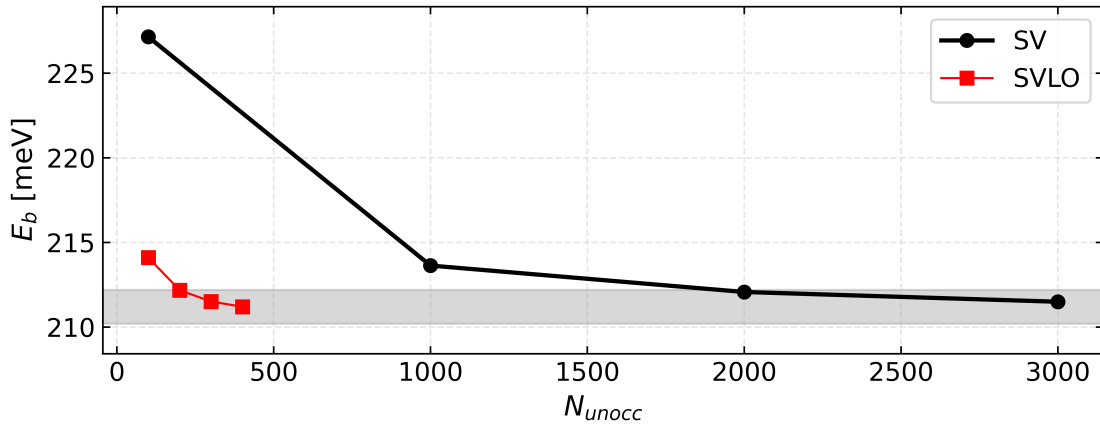


Figure 12: Exciton binding energy of  $\gamma$ -CsPbI<sub>3</sub> as a function of the number of unoccupied states,  $N_{unocc}$ . The gray shaded region indicates the convergence threshold of 2 meV.

## 6.5 Non-equilibrium BSE

The standard implementation of the BSE provides an accurate description of neutral excitations in materials. However, it is limited to steady-state conditions and fails to account for the non-equilibrium dynamics that arise under ultrafast excitations. In pump-probe spectroscopy, for instance, a laser pulse drives the system far from equilibrium, resulting in transient modifications to the electronic structure and optical response. To capture these effects, we have implemented a non-equilibrium variant of BSE by including photoinduced carrier distributions in the evaluation of both the momentum matrix elements and the screened Coulomb interaction [89, 90]. This modification enables the calculation of transient excitonic states and the corresponding spectra in the presence of non-equilibrium carrier populations. In practice, the approach involves solving the BSE using a time-dependent photoexcited carrier occupation, typically obtained from cDFT (see Section 3.7) or TDDFT (see Section 7.5). For an application to pump-probe spectroscopy, we refer to Section 8.3.

## 6.6 Resonant inelastic x-ray scattering

RIXS is a two step scattering process. An incident X-ray photon with energy  $\omega_1$  is absorbed by the system, creating an intermediate excited state by exciting a core electron into the conduction band. In a next step, the core hole is filled by a valence electron, yielding the emission of a photon with energy  $\omega_2$ . The final excited state thus consists of a hole in the valence band and an excited electron in the conduction band.

tion band. While energies of both incoming and outgoing photons lie in the X-ray region, the energy loss  $\omega = \omega_1 - \omega_2$  is in the range of only a few eV. The process is described by the Kramers-Heisenberg formula, following the theoretical description proposed in Refs. [36, 206] and implemented in the **BRIXS** package. Recent extensions concern the generalization in terms of arbitrary polarization vectors of the incoming and outgoing photon [218]. Accurate RIXS spectra are computed based on the results of two BSE calculations, one for the core, and one for the optical excitations. **BRIXS** uses the exciton eigenstates and eigenvalues from both calculations to determine the oscillator strengths and the excitation pathways. In a subsequent step, these quantities are combined to calculate the RIXS spectra for selected excitation energies. The present framework can be straightforwardly extended to non-equilibrium RIXS by employing non-equilibrium BSE calculations, as described in Section 6.5. For more details on the implementation of RIXS in **BRIXS**, we refer to Ref. [37].

We showcase the capabilities of **BRIXS** for the carbon K-edge of graphite. Graphite is a layered material with strong covalent in-plane bonds and weak inter-plane vdW interactions. While  $\pi$ -orbitals are oriented predominantly perpendicular to the graphene layers,  $\sigma$ -orbitals lie within the plane. Thus, graphite exhibits strong angular dependencies in its RIXS response. We consider an incident angle of  $\alpha = 60^\circ$  with perpendicular polarization relative to the beam direction, while the emitted photons are detected at  $90^\circ$  relative to the incident beam. Lifetime broadenings of 0.5 eV and 0.1 eV are applied for the intermediate state and the final state, respectively. The resulting RIXS spectra, shown in Fig. 13, reveal distinct angular dependencies. The left panel of Fig. 13 displays the RIXS intensity as a function of energy loss for several excitation energies  $\omega_1$ . For the chosen incident angle, the spectral feature region of 7 eV to 11 eV is dominating, indicating favored transitions into lower-lying  $\sigma^*$  states. In contrast, transitions into  $\pi^*$  states, lying closer to the Fermi energy, are suppressed and exhibit significantly weaker spectral features for low energy loss. However, the relative intensity of these  $\pi$ -related features becomes more pronounced at higher  $\omega_1$ . The right panel presents the normalized double-differential RIXS cross section as a function of both excitation energy  $\omega_1$  and energy loss  $\omega$ . It highlights the same dominant spectral region between 7 eV to 11 eV, while features at lower energy loss appear with reduced intensity. In addition, systematic shifts in the 3 eV to 5 eV energy-loss range towards higher energy loss with increasing excitation energy are observed. This behavior reflects the dispersion of the  $\pi$  band involved in the corresponding excitation and de-excitation pathways.

Since RIXS spectra are obtained from preceding BSE calculations, the **BRIXS** package was designed as a stand-alone tool, *i.e.*, it is not directly implemented in **exciting**. It is seamlessly integrated within **excitingworkflow**, but can also accept input from other BSE codes. The RIXS DDCS is computed with the Python package **pyBRIXS**. Both packages are available on GitHub [219, 220].

## 6.7 Lattice screening in the optical spectra of polar materials

While, in principle, the BSE accounts for screening effects of the Coulomb interaction between electrons and holes by both electronic and vibrational polarization, in practice most implementations consider only electronic screening, despite the fact that exciton-phonon coupling gives rise to a wide range of well-established physical phenomena (see Section 6.8). One particularly notable consequence of exciton-phonon coupling is the reduction of exciton binding energies, which originates from a weakened Coulomb attraction due to vibrational contributions to the screening. This lattice screening is especially important in ionic materials, where long-range optical phonon modes can generate strong macroscopic electric fields [221]. Within the BSE framework, such effects have previously been incorporated by modeling additional screening through approximations to the dielectric function [163, 222–227]. More recent first-principles approaches instead explicitly include a phonon-induced contribution to the screened Coulomb interaction [208, 210, 211].

Phonon-assisted screening effects have been implemented into the screened Coulomb interaction of the BSE framework. Applications to polar semiconductors such as ZnS, MgO, and GaN [211] have shown that vibrational screening not only leads to a renormalization of exciton binding energies at the absorption onset, but also to comparable red shifts of higher-energy absorption features in the order of 50 meV. These effects are mainly caused by long-range Fröhlich coupling to polar longitudinal optical phonons,

while other vibrational modes contribute negligibly.

## 6.8 Exciton-phonon coupling and exciton-polarons

The EXPC connects optical excitations to the lattice degrees of freedom. In some crystals and molecules, the creation of an exciton induces a charge-density redistribution, which can in turn drive a local lattice distortion. This lattice distortion feeds back to the excitons by renormalizing the excitonic wavefunction. The composite QP formed by an exciton dressed by its accompanying lattice distortion is commonly referred to as an exciton–polaron, and it is also known as a STE.

STEs can be obtained by solving a system of coupled equations that describe the interaction between the STE wavefunction and the lattice distortion. The theoretical framework and computational workflow shown in Fig. 14 follow Ref. [212]. Similar equations were independently formulated later and applied by other groups [213–215]. In this approach, the EXPC interaction matrix [228], which is essentially the excited-state force along phonon coordinates, is constructed by combining DFPT with the momentum-dependent BSE. The local lattice distortion is expanded by phonon normal modes, and the STE wavefunction is represented using momentum-dependent exciton wavefunctions. Notably, this formulation avoids explicit supercell modeling of STEs, enabling the entire computational procedure to be carried out within the primitive cell.

We take the CO molecule as a representative example to illustrate how the EXPC framework can be used to predict structural relaxation in the excited state. Fig. 15 shows a pronounced geometry relaxation upon photoexcitation: the C–O bond length increases from 1.13 Å in the ground state to 1.22 Å in the  $1^1\Pi$  excited state. Although CO exhibits only a single vibrational mode, our approach circumvents the conventional multi-step geometry optimization required by the excited-state force method, directly providing the relaxed excited-state structure.

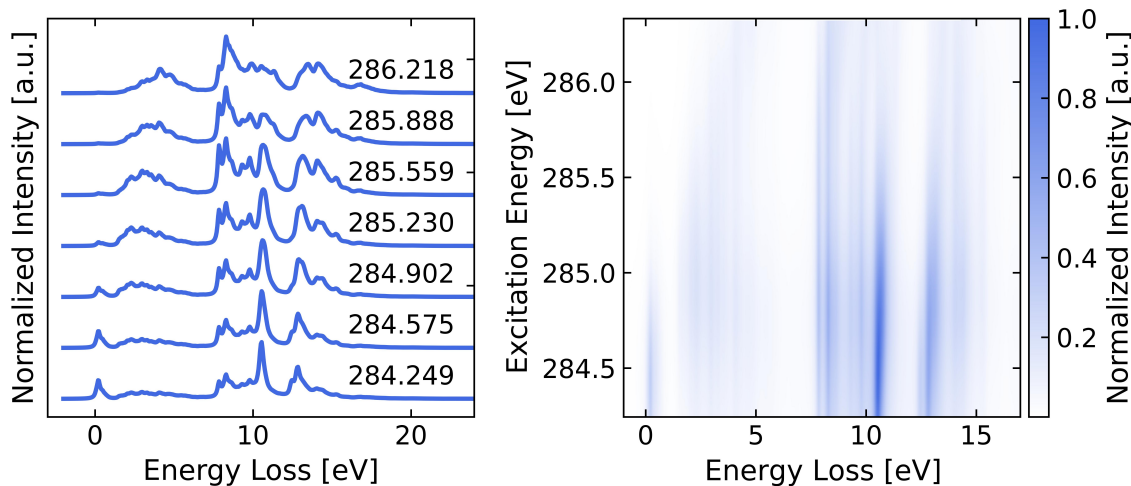


Figure 13: Left: RIXS spectra for the carbon K-edge of graphite as a function of the energy loss for different excitation energies  $\omega_1$ . Right: Normalized double-differential RIXS cross section as function of excitation energy  $\omega_1$  and energy loss  $\omega$ . The incident beam angle  $\alpha$  is  $60^\circ$ , with perpendicular polarization relative to the beam direction, described by  $(\cos \alpha, 0, \sin \alpha)$ . The emitted photons are detected at an angle of  $90^\circ$ , relative to the incident beam, with corresponding polarization given by  $(-\sin \alpha, 0, \cos \alpha)$ .

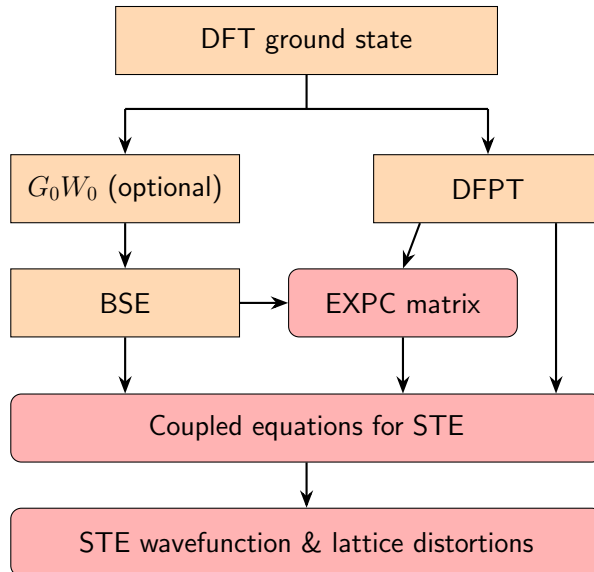


Figure 14: Workflow for constructing the EXPC matrix elements and computing STEs.

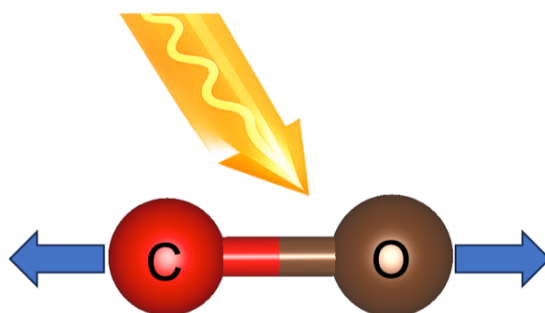


Figure 15: Schematic illustration of the excited-state structural relaxation of the CO molecule.

## 7 Time-dependent DFT

### 7.1 State of the art

TDDFT is an extension of DFT for describing electronic excitations of systems under external time-dependent perturbations. Formally, it is an exact theory as proven by the Runge-Gross theorem [3], which establishes a one-to-one correspondence between the time-evolution of the complex many-body wavefunction and the time-dependent density. Compared to methods based on Green functions, TDDFT is less well suited for materials with strong electron-hole interaction, but offers a superior balance between computational cost and accuracy [229], making it applicable to significantly larger and more complex systems. Due to this compelling advantage, TDDFT has become one of the most widely used methods in quantum chemistry and materials science to study excitations in molecules, nanostructures, and bulk materials [4–7]. In practical calculations, TDDFT can be applied either in the frequency domain or in the time domain, each of them offering advantages and limitations [230–233]. In the former, the time-dependent density is expressed directly in frequency space, typically within the linear response (LR) regime, where density variations are treated as a first-order response to an external perturbative potential. For instance, LR-TDDFT has been widely adopted to study optical spectra, electron-energy-loss spectra, low-lying excitation energies, and spin-flip transitions [4, 5, 233, 234]. More recently, it has even been applied to describe x-ray Thomson scattering in warm dense matter [235], magnetic excitations in ferromagnetic materials [236], self-trapped excitons in perovskites [237], and excited-state conical-intersection topologies in molecular systems[238].

Although the initial success of TDDFT can be mostly attributed to the LR formulation, recent advances in ultra-fast spectroscopy have triggered a crescent interest in real-time (RT) TDDFT as a theoretical tool for modeling transient spectroscopies, where full dynamical information about the excitation process is required [239]. In RT-TDDFT, the electron density is propagated explicitly in time in a non-perturbative way, providing direct insight into photoinduced processes in molecules and nanoscale systems. It has been successfully employed to simulate a broad range of phenomena, including non-linear optical processes [240], high-harmonic generation [241], attosecond charge injection and photodissociation [239], field-driven spin dynamics [4], strong-field and thermal ionization [242], pump-probe responses [241, 243], energy transfer mechanisms [240], optically driven demagnetization [244], and plasmonic resonances [245]. Another important capability enabled by RT-TDDFT is the coupling of electron dynamics with nuclear motion, allowing for non-adiabatic molecular dynamics (MD) that can track changes in atomic positions in response to electronic excitations, *e.g.*, laser pulses [34, 242]. One recurrent approach is Ehrenfest dynamics, in which the nuclei evolve classically according to Newton's equations, while the forces acting on them are obtained from the time-dependent electronic density computed via RT-TDDFT. This strategy has been employed in numerous studies; for example, to model solvated DNA under proton irradiation [246], coherent phonon generation [247], charge separation in photovoltaic materials [248], and excited carrier dynamics in carbon and BN nanostructures [249–251]. Furthermore, the MD description can be extended beyond the classical treatment of nuclei to incorporate quantum ionic effects within a multi-component formalism [233, 252, 253].

The accuracy of TDDFT, and consequently its agreement with experiments, depends strongly on the choice of the xc functional in RT-TDDFT or, correspondingly, of the xc kernel in LR-TDDFT [230, 233, 234, 254]. While considerable effort has been devoted in recent years to improving xc functionals and kernels [158, 233, 242, 255–260], the importance of numerical precision in TDDFT calculations is often overlooked. Without stringent numerical control, it is generally impossible to disentangle errors due to approximations (xc functional and kernel) from those introduced by the numerical implementation itself. In this context, like for DFT and *GW* calculations, a full-potential all-electron implementation offers a unique advantage. Based on the LAPW+LO basis, **exciting** provides efficient LR- and RT-TDDFT implementations, the latter including the capability of non-adiabatic MD via Ehrenfest dynamics.

## 7.2 Methodology

The time-evolution of the many-body wavefunction  $\Psi(t)$  representing an  $N$ -electron system subjected to a time-dependent external potential  $\hat{v}_{\text{ext}}(\mathbf{r}, t)$  is governed by the time-dependent Schrödinger equation. Given the initial state  $\Psi(0)$ , the Runge-Gross theorem guarantees that there is a unique map between  $\Psi(t)$  and the time-dependent electron density  $n_{\text{KS}}(\mathbf{r}, t)$  [3]. This correspondence allows for replacing the complex object  $\Psi(t)$  by  $n_{\text{KS}}(\mathbf{r}, t)$  as the central variable, thereby making the study of non-equilibrium quantum dynamics much more tractable. Similar to static DFT, in TDDFT,  $n_{\text{KS}}(\mathbf{r}, t)$  is obtained via a set of time-dependent KS functions  $|\psi_{n\mathbf{k}}\rangle$ , whose evolution is governed by:

$$\frac{d}{dt}|\psi_{n\mathbf{k}}(t)\rangle = -i\hat{h}_{\text{KS}}(t)|\psi_{n\mathbf{k}}(t)\rangle. \quad (66)$$

The time-dependent KS Hamiltonian is given by

$$\hat{h}_{\text{KS}}(t) = \hat{h}_{\text{KS}}(0) + \Delta\hat{h}_{\text{KS}}(t) + \hat{v}_{\text{ext}}(t), \quad (67)$$

where  $\Delta\hat{h}_{\text{KS}}(t)$  accounts for the changes in the Hartree and xc potentials:

$$\Delta\hat{h}_{\text{KS}}(t) = [\hat{v}_{\text{H}}(t) - \hat{v}_{\text{H}}(0)] + [\hat{v}_{\text{xc}}(t) - \hat{v}_{\text{xc}}(0)]. \quad (68)$$

One practical way to obtain spectroscopic properties is to assume that  $\hat{v}_{\text{ext}}$  is small and to apply perturbation-theory within LR-TDDFT. One central component is the reducible polarizability,  $\chi$ , also referred to as the density-density response function, which characterizes the response of the electron density due to the external potential:

$$\chi(\mathbf{r}, \mathbf{r}', t - t') = \frac{\delta n_{\text{KS}}(\mathbf{r}, t)}{\delta \hat{v}_{\text{ext}}(\mathbf{r}', t')}. \quad (69)$$

When transformed to the frequency domain and reciprocal space,  $\chi$  is given by a Dyson equation

$$\chi(\mathbf{q}, \omega) = \chi^0(\mathbf{q}, \omega) + \chi^0(\mathbf{q}, \omega) [v_{\text{H}}(\mathbf{q}) + f_{\text{xc}}(\mathbf{q}, \omega)] \chi(\mathbf{q}, \omega), \quad (70)$$

where  $\chi^0$  denotes the independent-particle polarizability, and  $f_{\text{xc}}$  is the xc kernel:

$$f_{\text{xc}}(\mathbf{r}, \mathbf{r}', t - t') = \frac{\delta \hat{v}_{\text{xc}}(\mathbf{r}, t)}{\delta n_{\text{KS}}(\mathbf{r}', t')}. \quad (71)$$

$f_{\text{xc}}$  measures the first-order response of  $\hat{v}_{\text{xc}}$  to electron density fluctuations. Analogous to the xc functional in static DFT, the choice of  $f_{\text{xc}}$  is the primary factor determining the accuracy of the calculated spectra: More sophisticated kernels representing higher levels of theory are generally expected to yield improved agreement with experiment [261].

From the polarizability, the microscopic dielectric function  $\varepsilon$  is obtained as

$$\varepsilon^{-1}(\mathbf{q}, \omega) = 1 + v_{\text{H}}(\mathbf{q}) \chi(\mathbf{q}, \omega), \quad (72)$$

the macroscopic dielectric function follows as

$$\varepsilon_{\text{mac}}(\mathbf{q}, \omega) = 1/\varepsilon_{00}^{-1}(\mathbf{q}, \omega). \quad (73)$$

$\varepsilon_{\text{mac}}$  is a complex function whose imaginary part is proportional to the absorption spectrum [13]. Furthermore, it gives access to several related frequency-dependent quantities, often termed *optical constants*, such as the loss function,  $\mathbb{L}(\mathbf{q}, \omega)$ , and the optical conductivity,  $\sigma$ :

$$\mathbb{L}(\mathbf{q}, \omega) = -\Im[\varepsilon_{\text{mac}}^{-1}(\mathbf{q}, \omega)], \quad (74)$$

$$\sigma(\mathbf{q}, \omega) = -i\frac{\omega}{4\pi}[\varepsilon_{\text{mac}}(\mathbf{q}, \omega) - 1]. \quad (75)$$

A different strategy, as adopted in RT-TDDFT, is to remain in the time-domain and explicitly propagate the KS wavefunctions according to Eq. 66. This equation is usually solved using a time-evolution operator (propagator)  $\hat{U}$  [262]:

$$\hat{U}(t + \Delta t, t) = \hat{\mathcal{T}} \left[ \exp \left( -i \int_t^{t + \Delta t} \hat{h}_{\text{KS}}(t') dt' \right) \right]. \quad (76)$$

The wavefunctions are then evolved in discrete time steps  $\Delta t$  as:

$$|\psi_{n\mathbf{k}}(t + \Delta t)\rangle = \hat{U}(t + \Delta t, t) |\psi_{n\mathbf{k}}(t)\rangle. \quad (77)$$

A common approximation in RT-TDDFT is the so-called adiabatic approximation, in which  $\hat{v}_{\text{xc}}(t)$  does not contain memory effects. Instead, it depends solely on the instantaneous KS density, and retains the same functional form as in ground-state DFT, with the ground-state density simply being replaced by its time-dependent counterpart.

While RT-TDDFT is usually employed to predict the real-time evolution of a system under a time-dependent external potential, such as a laser pulse, it can be also used to determine frequency-dependent optical constants. By adopting the velocity-gauge, the interaction with the external field  $\hat{v}_{\text{ext}}$  is expressed as:

$$\hat{v}_{\text{ext}}(t) = \hat{v}_{\text{ext}}(0) + \frac{\mathbf{A}(t)^2}{2c^2} - \frac{i}{c} \mathbf{A}(t) \cdot \nabla. \quad (78)$$

In this gauge, the vector potential is  $\mathbf{A}(t) = -c \int_0^t \mathbf{E}(t') dt'$ , where  $\mathbf{E}$  stands for the applied electric field, assumed to be spatially homogeneous within the unit cell. To obtain the optical response functions, the macroscopic current density  $\mathbf{J}(t)$  is evaluated as

$$\mathbf{J}(t) = \sum_{n\mathbf{k}} w_{\mathbf{k}} f_{n\mathbf{k}} \langle \psi_{n\mathbf{k}}(t) | i\nabla | \psi_{n\mathbf{k}}(t) \rangle - \frac{N\mathbf{A}(t)}{c\Omega}, \quad (79)$$

$N$  being the number of valence electrons per unit cell. Upon Fourier transformation to the frequency domain, the  $i, j$  tensor-components of  $\varepsilon_{\text{mac}}$  are given by

$$\varepsilon_{\text{mac}}^{ij}(\omega) = \delta_{ij} + \frac{4\pi i}{\omega} \frac{J_i(\omega)}{E_j(\omega)} \quad (80)$$

with  $i, j \in x, y, z$  denoting Cartesian directions.

### 7.3 Linear-response TDDFT in **exciting**

In **exciting**, the matrix elements of the independent-particle polarizability are evaluated as

$$\chi^0_{\mathbf{GG}'}(\mathbf{q}, \omega) = \frac{1}{N_{\mathbf{k}}\Omega} \sum_{nn'\mathbf{k}} \frac{f_{n\mathbf{k}} - f_{n'\mathbf{k}+\mathbf{q}}}{\epsilon_{n\mathbf{k}} - \epsilon_{n'\mathbf{k}+\mathbf{q}} + \omega + i\eta} M_{nn'\mathbf{k}}(\mathbf{G}, \mathbf{q}) M_{nn'\mathbf{k}}^*(\mathbf{G}', \mathbf{q}), \quad (81)$$

where the  $\mathbf{q}$ -dependent matrix elements  $M_{nn'\mathbf{k}}(\mathbf{G}, \mathbf{q})$  are defined in Eq. 61.  $\chi^0_{\mathbf{GG}'}(\mathbf{q}, \omega)$  is then inserted into the Dyson equation (Eq. 70) to obtain the reducible polarizability  $\chi_{\mathbf{GG}'}(\mathbf{q}, \omega)$ . This formulation includes local-field effects (LFEs), which are accounted for by the microscopic  $\mathbf{G} \neq 0$  components of the induced response. In Eq. (70), the exchange-correlation kernel  $f_{\text{xc}}$  must be specified. In **exciting**, the following kernels are implemented:

- RPA, defined by  $f_{\text{xc}} = 0$ ;
- Adiabatic LDA, which is derived from the LDA xc potential;
- Long-range corrected kernels, including both a static form,  $f_{\text{xc}} = \alpha/\mathbf{q}^2$  [263], and a dynamic version,  $f_{\text{xc}} = (\alpha + \beta\omega^2)/\mathbf{q}^2$  [264];

- Family of bootstrap kernels [158, 265];
- BSE-derived many-body kernel [263, 266].

In addition, also the independent particle approximation (IPA) is available. This corresponds to setting  $\chi(\mathbf{q}, \omega) = \chi_0(\mathbf{q}, \omega)$  in Eq. 70. In the long-wavelength limit  $\mathbf{q} \rightarrow 0$ , the matrix elements  $M_{nn'\mathbf{k}}$  are expressed in terms of the momentum matrix elements  $\mathbf{P}_{nn'\mathbf{k}}$ , which allows for computing the full macroscopic dielectric tensor  $\varepsilon_{\text{mac}}^{ij}(\omega)$ . Optionally, the anomalous Hall contribution can be included in the tensor, which allows for computing magneto-optical Kerr effect (MOKE) spectra [267]. More information on the implementation of LR-TDDFT in **exciting** can be found in Refs. [20, 268, 269].

## 7.4 Real-time TDDFT in **exciting**

To solve Eq. 77, several propagators are implemented in **exciting**, namely the simple exponential, the exponential at midpoint, the approximate enforced time-reversal symmetry scheme, the commutator-free Magnus expansion of fourth order, the exponential using a basis of the Hamiltonian eigenvectors, and the classical fourth-order Runge-Kutta method [231]. Using one of these propagators, Eq. 77 is solved by expanding each KS state in a chosen basis set  $|\phi_{n\mathbf{k}}\rangle$ , with time-dependent coefficients  $c_{n\mathbf{k}}(t)$ :

$$|\psi_{n\mathbf{k}}(t)\rangle = \sum_{n'} c_{nn'\mathbf{k}}(t) |\phi_{n'\mathbf{k}}\rangle. \quad (82)$$

Two basis sets are implemented:

- The default LAPW+LO basis functions, known for achieving the ultimate precision in describing KS states [231];
- The GS KS wavefunctions  $|\psi_{n\mathbf{k}}(0)\rangle$ , which typically offer a more computationally efficient alternative [270]. In this case, the basis set includes excited states, whose number must be carefully converged.

To monitor the effects of the external electric field, **exciting** can output the time-dependent fluctuations in charge density  $n_{\text{KS}}(\mathbf{r}, t) - n_{\text{KS}}(\mathbf{r}, 0)$ . This can provide insight into how electrons are driven by the laser pulse and how chemical bonds are affected during the excitation process. Furthermore, by projecting the time-dependent Kohn-Sham (TDKS) states  $|\psi_{n\mathbf{k}}(t)\rangle$  onto the reference ground-state wavefunctions, **exciting** provides the number of excited electrons and holes per unit cell together with their distribution in  $\mathbf{k}$ -space [231]:

$$\Delta f_{n\mathbf{k}}(t) = \sum_{n'} f_{n'\mathbf{k}}(0) \langle \psi_{n\mathbf{k}}(0) | \psi_{n'\mathbf{k}}(t) \rangle - f_{n\mathbf{k}}(0), \quad (83)$$

where a positive (negative) value corresponds to the presence of an excited electron (hole). To exemplify this feature, Fig. 16 illustrates the number of excited electrons per unit cell in WSe<sub>2</sub> subjected to a laser pulse of frequency 1.9 eV and duration 4.0 fs. The intensity of the applied field is varied from  $I_0 = 1.5 \text{ TW/cm}^2$  down to  $I_0/8$ . Figure 16 also shows the distribution of excitations in  $\mathbf{k}$ -space at times 1.0 (top), 2.1 (middle), and 4.0 fs (bottom).

For users more interested in methodological details, besides the adiabatic approximation, two other models of  $\Delta\hat{h}_{\text{KS}}(t)$  are implemented:

- $\hat{v}_{\text{xc}}(t)$  is kept fixed at its ground-state value  $\hat{v}_{\text{xc}}(0)$ . In the linear regime, this corresponds to the RPA.
- Both  $\hat{v}_{\text{H}}(t)$  and  $\hat{v}_{\text{xc}}(t)$  are frozen to their initial values, so that the vector potential  $\mathbf{A}(t)$  is the only driver of the time evolution. This represents the IPA.

Strictly speaking, these latter schemes lie outside the formal TDDFT framework and should instead be regarded as TDKS approaches. Nevertheless, they can be useful to disentangle the individual contributions of the xc and Hartree potentials to the excitation dynamics.

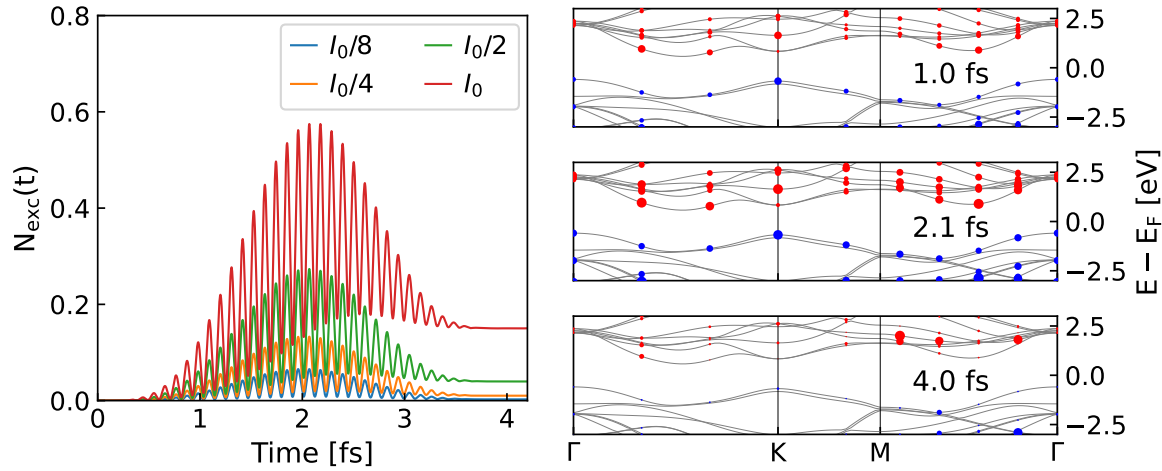


Figure 16: Left: Number of excited electrons per unit cell in WSe<sub>2</sub> for various laser intensities ( $I_0 = 1.5 \text{ TW/cm}^2$ ). Right: Bandstructure of WSe<sub>2</sub>, showing the populations of excited electrons (red) and holes (blue) in the conduction and valence bands, respectively, at times 1.0 (top), 2.1 (middle), and 4.0 fs (bottom).

## 7.5 Femtosecond dynamics for ultrafast pump-probe spectroscopy

RT-TDDFT can also provide a first-principles description of the pump step in ultrafast pump-probe experiments. The pump pulse is modeled through a time-dependent vector potential whose parameters, such as duration, frequency, polarization, and fluence, are chosen to match experimental conditions. In the presence of this external driving field, the KS states are explicitly propagated in real time according to Eq. (66), yielding the non-equilibrium electronic state induced by the pump. The resulting non-equilibrium electronic state is monitored through projections onto the GS KS manifold. In practice, we construct the  $\mathbf{k}$ - and band-resolved occupations, according to Eq. (83), and the photoinduced changes  $\Delta f_{n\mathbf{k}}(t) = f_{n\mathbf{k}}(t) - f_{n\mathbf{k}}(0)$ . These femtosecond occupations retain the transient redistribution in energy and  $\mathbf{k}$ -space induced by the pump pulse. The occupation numbers  $f_{n\mathbf{k}}(t)$  evaluated at selected pump-probe delays are then provided as input to the non-equilibrium BSE implementation (see Section 8.3).

## 7.6 Non-adiabatic molecular dynamics

The Born-Oppenheimer (BO) approximation is one of the most widely adopted approaches in *ab initio* MD. Under this approximation, the nuclei are considered point charges moving on a potential energy surface generated by the electrons and other nuclei. The electrons, in turn, are treated quantum mechanically; they respond adiabatically to the nuclear motion, remaining in their eigenstate (typically the GS) at each time step [34, 271–276]. Despite its success, the BO approximation is inadequate for certain scenarios, such as modeling the interaction between electromagnetic waves and matter. Processes in which electrons are excited by ultra-fast time-dependent fields and subsequently dissipate energy through coupling to lattice vibrations are inherently non-adiabatic and thus require treatment beyond the BO approximation [34, 273]. Prominent examples of such phenomena, which are of growing interest, include pump-probe experiments [245] (see Section 8). An efficient approach to non-adiabatic MD is the Ehrenfest method, which combines a classical treatment of the nuclei with a non-adiabatic evolution of the electronic wavefunctions, usually within the framework of RT-TDDFT [34, 277, 278]. Ehrenfest dynamics has been implemented in **exciting**, enabling the efficient simulation of complex non-adiabatic processes.

Within the velocity-gauge, as assumed in this implementation, the action integral for the total system of nuclei and electrons is [34]

$$\int_{t_1}^{t_2} dt \left[ \sum_{\alpha} \frac{M_{\alpha} \dot{\mathbf{S}}_{\alpha}^2}{2} + \frac{Z_{\alpha}}{c} \dot{\mathbf{S}}_{\alpha} \cdot \mathbf{A}(t) \right] + \int_{t_1}^{t_2} dt \sum_{n\mathbf{k}} f_{n\mathbf{k}} w_{\mathbf{k}} \left\langle \psi_{n\mathbf{k}}(t) \left| i \frac{\partial}{\partial t} - \hat{h}_{\text{KS}} \right| \psi_{n\mathbf{k}}(t) \right\rangle. \quad (84)$$

It comprises two terms. The first one describes the nuclear motion and its coupling with the external

electric field, whereas the second term represents the electronic contributions. Extremizing the action integral with respect to  $|\psi_{n\mathbf{k}}\rangle$  leads to Eq. (66) as the electronic equation of motion. Since the LAPW+LO basis depends on the atomic positions,  $|\phi_n\rangle$  in Eq. (82) change over time following the nuclear motion. Taking this into account gives:

$$\sum_{n'} \langle \phi_{n\mathbf{k}} | \phi_{n'\mathbf{k}} \rangle \dot{c}_{n'n''}(t) = - \sum_{n'} \left[ i \langle \phi_{n\mathbf{k}} | \hat{h}_{\text{KS}} | \phi_{n'\mathbf{k}} \rangle(t) + \sum_{\alpha} \dot{\mathbf{S}}_{\alpha} \cdot \left\langle \phi_{n\mathbf{k}} \left| \frac{\partial \phi_{n'\mathbf{k}}}{\partial \mathbf{S}_{\alpha}} \right. \right\rangle \right] c_{n'n''}(t). \quad (85)$$

The corresponding equation for the motion of the nuclei is:

$$M_{\alpha} \ddot{\mathbf{S}}_{\alpha}(t) = - \frac{Z_{\alpha}}{c} \frac{d\mathbf{A}}{dt}(t) + \mathbf{F}_{\text{HF},\alpha}(\mathbf{S}_{\alpha}, t) + \mathbf{F}_{\text{corr},\alpha}(\mathbf{S}_{\alpha}, t). \quad (86)$$

The first term on the right-hand side denotes the external force due to the interaction with the applied electric field;  $\mathbf{F}_{\text{HF},\alpha}$  is the Hellmann-Feynman force; and  $\mathbf{F}_{\text{corr},\alpha}$  represents the so-called Pulay corrections. Details on the implementation can be found in Ref. [34].

## 7.7 Effective Schrödinger equation with dynamical Berry-phase field coupling

While the velocity gauge can be employed in a wide class of problems, it has two major drawbacks. First, at low frequencies of the external field, velocity-gauge calculations may exhibit non-physical divergences associated with numerical accuracy limitations [279, 280]. Another disadvantage is related to the introduction of non-local potentials in the time-dependent Hamiltonian, such as scissor-correction operators or non-local self-energies. In this case, each operator must be gauge-transformed, resulting in more involved expressions that can complicate numerical implementations [281, 282]. Moreover, the velocity operator used to calculate the density current must be modified to incorporate all non-local contributions to the Hamiltonian [283, 284]. These difficulties are absent when the length gauge is employed. However, a straightforward use of the standard field-coupling term  $\mathbf{E}(t) \cdot \mathbf{r}$  violates the periodic boundary conditions (PBC) usually employed in calculations with extended systems. An effective Schrödinger equation approach that employs the length gauge in a PBC-compatible way by using the dynamical Berry phase, was developed in Refs. [285, 286] and implemented in the YAMBO package [125].

With the RT-TDDFT module of **exciting**, it is possible to use the dynamical Berry-phase approach and numerically integrate the following equations of motion for spatially periodic parts of the valence KS wavefunctions  $|v_{m\mathbf{k}}(t)\rangle = e^{-i\mathbf{k}\cdot\mathbf{r}'} |\psi_{m\mathbf{k}}(t)\rangle$ :

$$i \frac{d}{dt} |v_{m\mathbf{k}}(t)\rangle = \left\{ e^{-i\mathbf{k}\cdot\mathbf{r}'} \left[ \hat{h}_{\text{KS}}(0) + \Delta \hat{h}_{\text{QP}} + \Delta \hat{h}_{\text{KS}}(t) \right] e^{i\mathbf{k}\cdot\mathbf{r}'} + i \mathbf{E}(t) \cdot \partial_{\mathbf{k}} \right\} |v_{m\mathbf{k}}(t)\rangle, \quad (87)$$

where  $\mathbf{r}'$  and  $\mathbf{r}$  correspond to the coordinates of the bra- and ket-states respectively,  $\partial_{\mathbf{k}}$  denotes gauge-invariant  $\mathbf{k}$ -derivative, and  $\Delta \hat{h}_{\text{QP}}$  is a scissor-correction operator [13, 287], which rigidly shifts the conduction band (CB) by  $\Delta\epsilon_{\text{QP}}$  to mimic the QP gap:

$$\Delta \hat{h}_{\text{QP}} = \Delta\epsilon_{\text{QP}} \sum_{m \in \text{CB}} |\psi_{m\mathbf{k}}\rangle \langle \psi_{m\mathbf{k}}|. \quad (88)$$

We note that Eq. (87) lies beyond the scope of standard DFT, which implies a one-to-one mapping of electronic density and one-particle KS potential. More details on the numerical implementation of the propagation of Eq. (87) in **exciting** will be published elsewhere [288].

After the propagation, the time-dependent macroscopic polarization can be obtained using the modern theory of polarization [289, 290]:

$$\mathbf{P}_{\alpha} = \frac{\mathbf{a}_{\alpha}}{\pi \Omega N_{\mathbf{k}_{\alpha}^{\perp}}} \sum_{\mathbf{k}_{\alpha}^{\perp}} \Im \left[ \ln \prod_{i=1}^{N_{\mathbf{k}_{\alpha}}-1} \det \langle v_{m\mathbf{k}} | v_{n\mathbf{k}_{\alpha}^{\perp}} \rangle \right], \quad (89)$$

where  $N_{\mathbf{k}_\alpha}$  and  $N_{\mathbf{k}_\perp}$  denote the number of  $\mathbf{k}$  points along cell direction  $\alpha$  and orthogonal to it, respectively. The polarization can be used to calculate optical response functions, such as the macroscopic dielectric function:

$$\epsilon_{\text{mac}}^{ij}(\omega) = \delta_{ij} + 4\pi P_i(\omega)/E_j(\omega). \quad (90)$$

As an illustration, we calculate the linear-response absorption spectrum of an h-BN monolayer by applying an external field in the form of a Dirac delta function  $\mathbf{E}(t) = \delta(t = 0) \mathbf{e}_y$ , which is flat in the frequency domain. A scissor shift of  $\epsilon_{\text{QP}} = 2.6$  eV is used in the calculations to mimic the h-BN QP gap of 7.25 eV [291]. In Fig. 17, we show the imaginary part of the corresponding component of the dielectric function,  $\epsilon_{\text{mac}}^{yy}(\omega)$ . As seen from the results, the simple inclusion of the scissor operator in the dynamical equation within the length gauge leads to the desired shift in the linear-response spectrum.

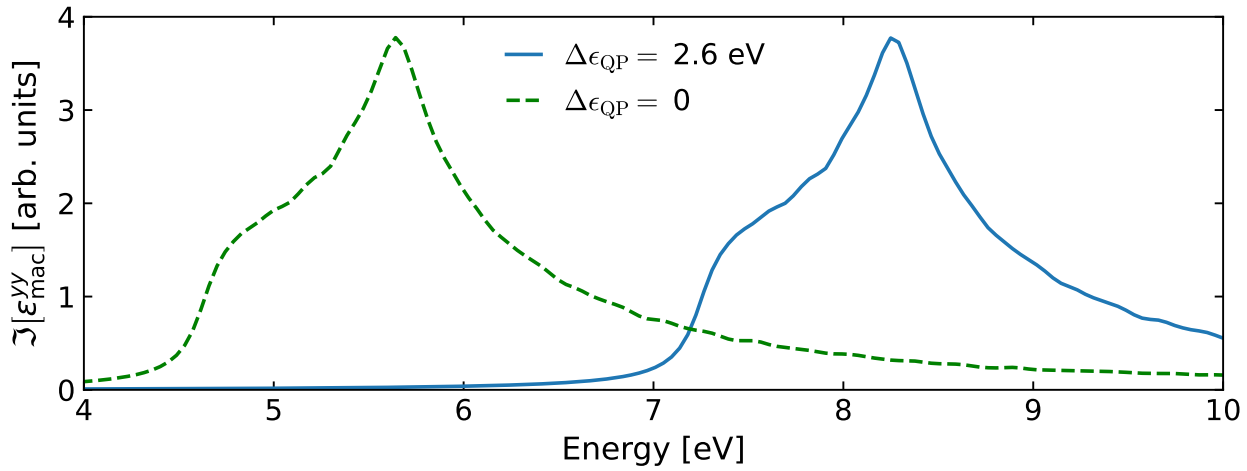


Figure 17: Imaginary part of the dielectric function (Eq. (90)) of an h-BN monolayer, calculated from the time-dependent macroscopic polarization obtained as a response to the delta-shaped pulse via propagating Eq. (87). Solid and dashed curves correspond to different values of the scissor shift used in Eq. (88). A Lorentzian broadening of 0.1 eV is included in the Fourier transform of the postprocessing-step.

## 8 Pump-probe spectroscopy

### 8.1 State of the art

Pump-probe spectroscopy is a state-of-the-art time-resolved technique for investigating light-matter interaction, particularly non-equilibrium processes like exciton dynamics [292]. Advances in laser technology enable this technique to access a broad energy window, from the infrared and visible [293] to the extreme ultraviolet [294] and X-ray domains [295]. In pump-probe probe spectroscopy experiments, transient features have been widely reported and associated with photoinduced carriers and excitonic effects [296–301]. Interpreting these signals requires theoretical frameworks that can accurately describe the excited-state electronic structure and its evolution under sequential light–matter interactions.

Several theoretical approaches have been developed to simulate pump-probe experiments, including Bloch-equation-based formalisms [302, 303], and model Hamiltonian approaches [304, 305], which do not provide a truly predictive, first-principles description of real materials. As an alternative, TDDFT has become a popular *ab initio* approach for simulating the pump-probe process [297, 300]. However, this mean-field formulation does not explicitly capture many-body interactions. More accurate correlated wavefunction techniques, including a time-dependent configuration-interaction-singles approach [306] and CC theory [307], can accurately treat the electron correlation, but the high computational cost limits their application to atoms or molecules. Many-body approaches based on the BSE have proven highly successful for describing both optical absorption and X-ray absorption spectroscopy (XAS) in solids, capturing electron-hole interactions essential for valence and core excitations (see Section 6).

In standard applications, BSE calculations treat either optical excitations or core-level excitations starting from the ground state, *i.e.*, in a *static* manner. Extensions to non-equilibrium implementations remain limited. While BSE-based methods have been applied to describe optical-pump / optical-probe scenarios involving valence excitons [308], studies of X-ray or extreme-ultraviolet spectra of optically excited materials typically employ approximate treatments of valence excitations and do not adopt a unified many-body description of valence and core excitations [309–311]. Overcoming such shortcomings, a fully consistent many-body description of X-ray absorption from excitonic initial states has only recently been achieved by treating both optical and core-excited states within a unified theoretical framework [204]. To capture the time evolution of the carrier distribution induced by pump excitation, a theoretical approach based on the non-equilibrium BSE formalism has recently been developed [89, 90].

### 8.2 Optical pump / X-ray probe spectroscopy

A framework based on the BSE has been developed to describe optical-pump / X-ray-probe experiments in solids [204]. It allows for treating valence-excited states as initial states and core-excited states as final states within the same formalism. The key novelty of this approach is the consistent inclusion of electron–hole interactions for both valence and core excitations, enabling a direct connection between transient pre-edge features in X-ray absorption spectra and the microscopic structure of valence excitons.

This framework provides a rigorous basis for modeling and interpreting pump–probe X-ray experiments on photoexcited materials. It is based on second-order time-dependent perturbation theory combined with BSE calculations. For this purpose, we introduce the **PreXAS-Exciton** package. This implementation extends the BSE formalism to pump–probe scenarios, where an optical pulse first generates a valence exciton and a subsequent X-ray pulse probes the resulting transient electronic structure into vacant states below the Fermi level. It requires outputs from two independent **exciting** BSE calculations and is available on GitHub [312]. This package provides a first-principles route for modeling polarization- and element-resolved X-ray signatures of excitonic states in solids. From two BSE runs—one describing optical valence-to-conduction excitations and another yielding core-to-conduction excitations, the code evaluates transition weights connecting these excitonic states. The execution of **PreXAS-Exciton** requires only a few input parameters: the excitation energies  $\omega_o$  and  $\omega_x$  of the optical and X-ray pulses, the numbers  $N_{\lambda_v}$  and  $N_{\lambda_c}$  of considered valence–conduction and core–conduction excitations, the lifetime broadenings  $\eta_I$  and  $\eta_F$  of the intermediate and final states, and the polarizations of the pump and probe

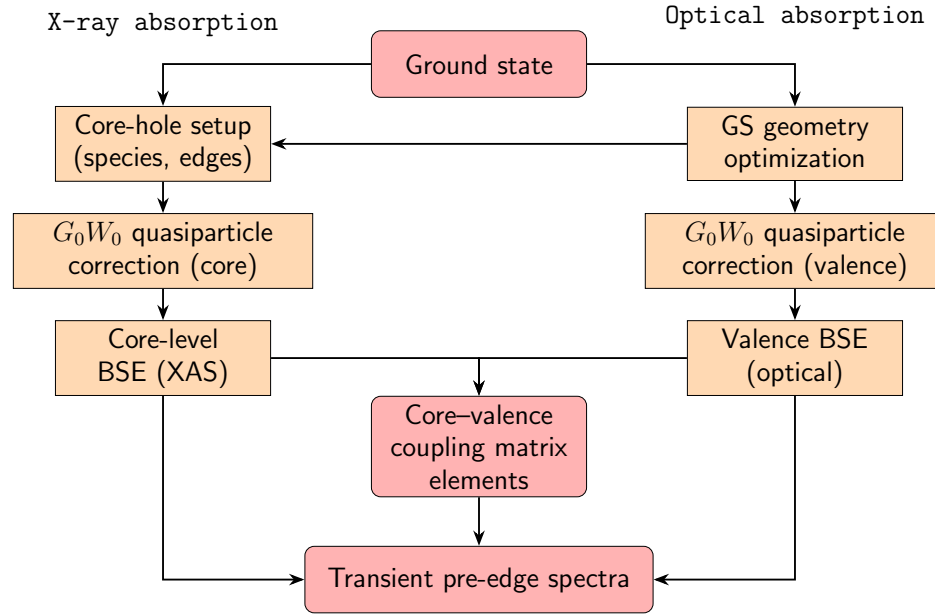


Figure 18: Workflow for simulating optical pump / X-ray probe spectra using the PreXAS-Exciton package based on exciting data.

pulses.

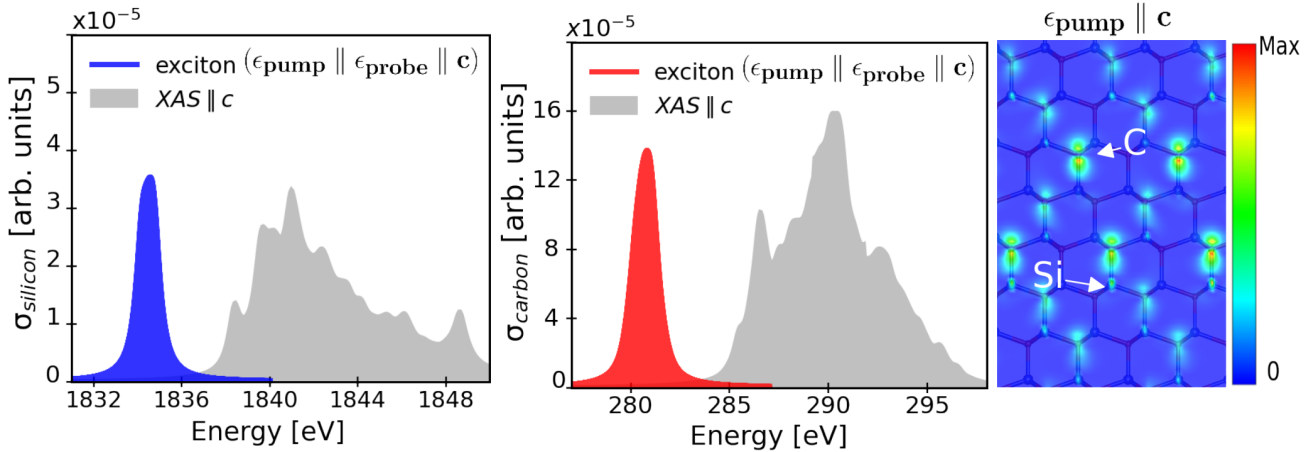


Figure 19: Silicon K-edge XAS (left) and carbon K-edge spectra (middle panel) in 4H-SiC. The blue (red) peak shows XAS spectra of optically pumped states for the polarizations of the pump and probe pulses parallel to the crystallographic **c** direction. The GS XAS spectra are shown in gray. Right: 2D cuts of the averaged hole distribution of the excitonic states after the action of a pump pulse polarized parallel to **c**. Figure adapted from Ref. [204] (copyright American Physical Society).

As an example, we show calculations for 4H-SiC in Fig. 19. We analyze the hole distribution (right panel) obtained for pump-pulse polarizations along the crystallographic **c** direction, together with the corresponding polarization-resolved pre-edge X-ray absorption signals (left and middle panels). The hole distribution cut exhibits predominantly carbon and silicon *p*-type characters oriented along the **c** axis. The associated pre-edge spectra reveals a strong peak caused by an enhanced transition probability from the core level into these valence states compared to the perpendicular direction (not shown here). This behavior reflects the sensitivity of core-level transitions to orbital symmetry and demonstrates a direct correspondence between the spatial orientation of the excitonic hole distribution and the intensity of the pre-edge feature in the X-ray absorption spectrum. For details, we refer to Ref. [204].

### 8.3 Pump-probe spectroscopy based on non-equilibrium BSE

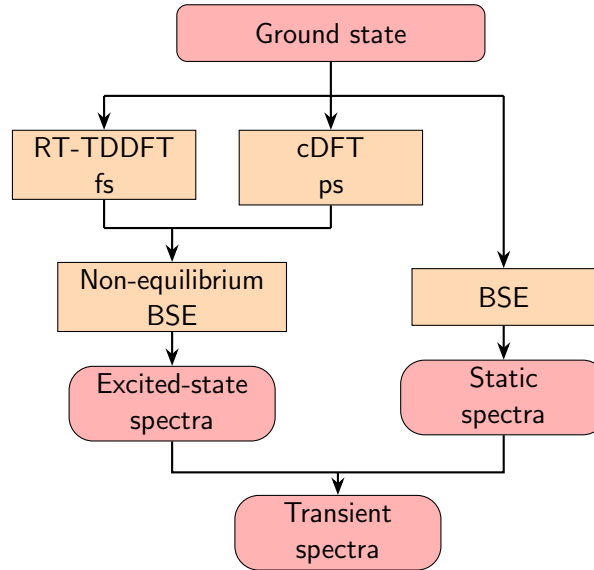


Figure 20: Workflow for simulating pump-probe spectra using non-equilibrium BSE.

We have developed a computational framework based on the newly implemented non-equilibrium BSE (see Section 6.5), as shown in Fig. 20. This framework makes use of RT-TDDFT and cDFT, respectively, to model the pump-induced dynamics across different timescales. At femtosecond time delays, carrier populations are extracted from RT-TDDFT simulations (see Section 7.5), where Kohn-Sham orbitals evolve under a time-dependent vector potential representing the optical pump. At longer, *i.e.*, picosecond, timescales, thermalized carrier occupations are obtained according to the Fermi-Dirac distribution using cDFT (see Section 3.7). The resulting photoexcited carrier populations are incorporated into the BSE Hamiltonian, modifying both the transition matrix elements and the screened Coulomb interaction. These modifications account for two essential many-body effects that govern transient optical responses, namely Pauli blocking and Coulomb screening. The transient absorption (TA) spectrum is given as the difference between the excited-state and static spectra. It has been successfully applied to a range of semiconductors, including WSe<sub>2</sub>, CsPbBr<sub>3</sub>, and ZnO [89, 90]. In Fig. 21, we show the pump-induced absorption spectra for the K-edge of Zn in ZnO and its evolution across different timescales. By disentangling the contributions from Pauli blocking and photoinduced Coulomb screening, we identify the latter as the dominant mechanism governing the spectral response [89]. Overall, this framework provides a quantitative method for simulating and interpreting pump-probe experiments. It can capture transient excitations on different time scales, from femtoseconds to picoseconds, and across a broad spectral range, from the visible and near-infrared to the extreme ultraviolet and X-ray regimes.

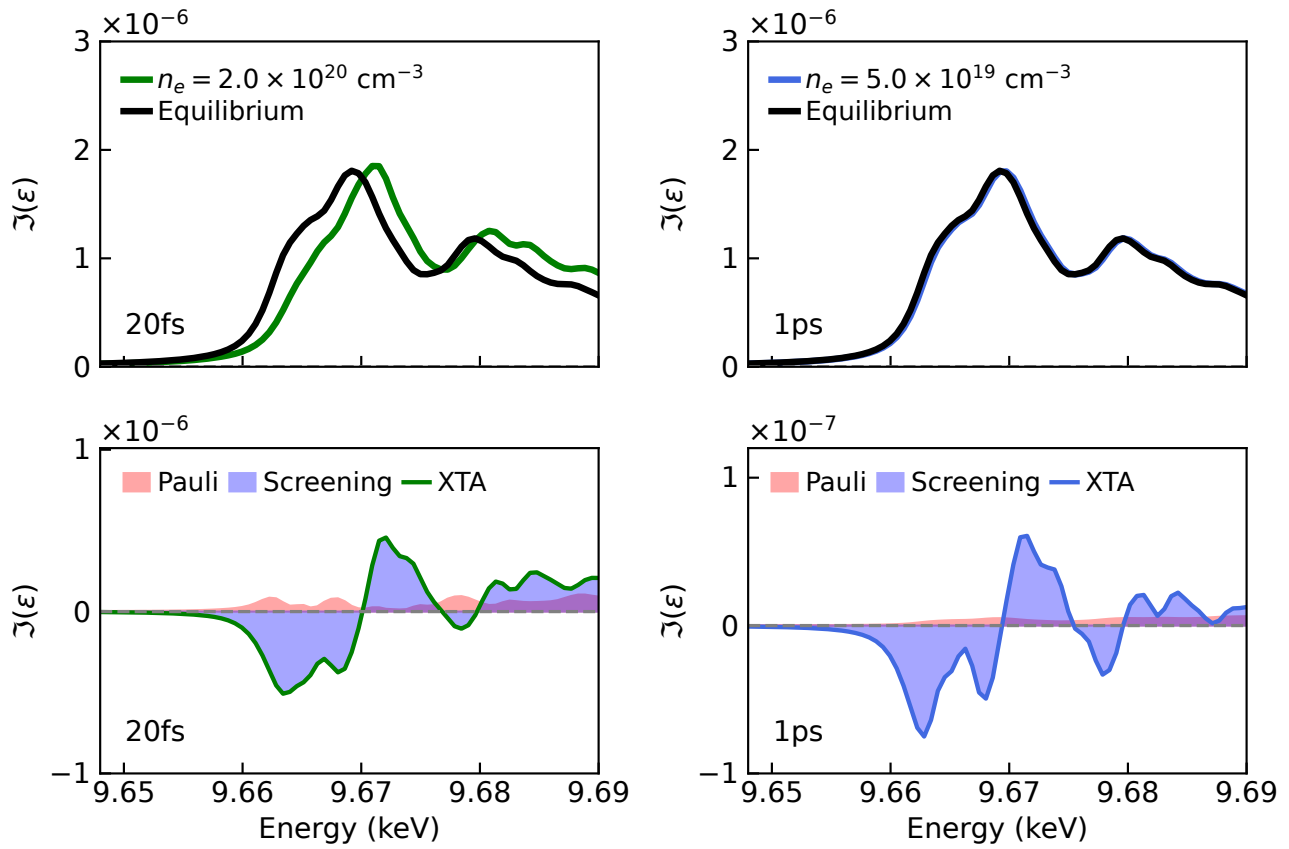


Figure 21: Top panels: Static (black) and excited-state XAS spectra (green/blue) at different carrier densities,  $n_e$ , on the femtosecond (left) and picosecond (right) timescales for the Zn K-edge of ZnO. Bottom panels: Corresponding TA spectra and their decomposition into Coulomb screening (blue) and Pauli blocking (red) effects.

## 9 Tools, workflows, and interfaces

### 9.1 State of the art

In modern computational materials science, the usage of an electronic-structure code extends far beyond its mere execution of isolated calculations. Research practices increasingly rely on automated workflows, large-scale data generation [313], systematic convergence studies [314], and advanced post-processing tools that transform raw outputs into physically meaningful observables. At the same time, users expect user-friendly interfaces, reproducible workflows, and seamless integration with external frameworks such as high-throughput platforms, data infrastructures, and analysis environments. As a result, the state of the art in the field has shifted from monolithic, stand-alone DFT programs toward rich software ecosystems that combine simulation engines with workflow frameworks, analysis tools, continuous testing, and comprehensive documentation. For a more detailed review on workflows in materials science, we refer to Ref. [315].

Building on this evolution, modern electronic-structure research is typically supported by a diverse set of auxiliary codes that complement the core simulation engine. These include code-specific and code-agnostic post-processing frameworks for extracting materials properties, scripting interfaces for systematic input generation and output parsing, and workflow layers that orchestrate complex, multi-step simulations. Such components are most commonly implemented in Python. Together, these tools reduce the manual effort required to perform routine tasks, promote reproducibility, and enable scalable computational studies.

Python interfaces to electronic-structure codes have become building blocks for modern automation and reproducibility, as exemplified by the ABINIT code [316], which is supported by the Python library AbiPy, or VASP [317], which is supported by py4vasp. The development of `excitingtools` [318] fits well with the trend of providing a Python interface layer for input/output handling and workflow automation. Similarly, the Atomic Simulation Environment (ASE) [319] offers a general Python interface to multiple electronic-structure codes through so-called calculators, including VASP, Quantum ESPRESSO [320], GPAW [321], and many more, serving as a basis for workflow automation and steering of atomistic simulations. `excitingtools` has been adopted by ASE, where it serves as the interface to the `exciting` code.

Workflow libraries for atomistic and electronic-structure calculations are, in principle, largely independent of the underlying code, as they implement abstract concepts such as tasks, dependencies, provenance, and execution backends [322]. In practice, however, the implementation of robust and efficient workflows requires a tight coupling to the specifics of each electronic-structure code, including its input parameters, output formats, error modes, and restart capabilities. Prominent examples include Atomic Simulation Recipes (ASR) [323], which allows to create higher-level workflow layers on top of code-specific ASE calculators to define reusable workflows for ground-state and materials-property calculations, executed with MyQueue [324]. Similarly, the Materials Project [325] software stack combines pymatgen [326] for structured input/output handling with workflow engines such as jobflow [327] and atomate2 [328], providing automated and provenance-aware workflows primarily targeting codes like VASP and Quantum ESPRESSO. Another widely used framework is AiiDA [329], which offers a code-agnostic workflow engine and provenance model, but still relies on dedicated plugins to interface individual simulation codes in a reliable and reproducible manner. `exciting` is situated within this evolving landscape, offering a rich portfolio of methodology, including the Python packages `excitingtools` and `excitingworkflow`, as well as interfaces to other simulation codes.

### 9.2 Workflow tools in support of `exciting`

In this section, we describe various components of the `exciting` software ecosystem. The Python library `excitingtools` [318] provides a high-level, extensible interface, designed to simplify both input generation and output analysis of `exciting`. It offers robust parsers that convert `exciting` output files into well-structured and serializable Python classes and dictionaries, enabling seamless integration with

data-analysis frameworks and higher-level workflow managers. It provides object-oriented classes for constructing and manipulating input files in a flexible and programmatic way. The library aims to support the full range of **exciting**'s capabilities, including GS and excited-state calculations such as *GW*, BSE, and RT-TDDFT. The package is distributed with the **exciting** code, and is additionally publicly available on PyPI [330].

Within the **exciting** ecosystem, the Python package **excitingworkflow** builds directly on top of **exciting** to provide a framework for defining and executing automated high-throughput calculations and complex workflows with **exciting**. It employs the jobflow library as its underlying workflow framework, enabling the modular definition, execution, and chaining of computational tasks. Designed with scalability and reproducibility in mind, the package supports remote execution on compute clusters with queue managers like Slurm through jobflow-remote. **excitingworkflow** forms the basis for systematic and reproducible **exciting** calculations within automated workflow environments. It currently implements workflows for monitoring the convergence of various input parameters and for the automated optimization of the LO basis. The convergence workflows are designed to be highly dynamic. In each step, the selected parameter is updated, the corresponding calculation is executed, the convergence criterion is evaluated, and additional steps are generated only when necessary. Robust error-handling mechanisms are included to automatically recover from common issues, such as time-outs or insufficient memory. **excitingworkflow** will be released in the near future.

In addition to these more comprehensive workflow tools, we also maintain the Python package **excitingscripts**, which provides practical scripts for using **exciting**. These scripts give users convenient access to commonly used functions, such as setting up convergence tests in a human readable form, updating parameters in input files, plotting results, and more. Currently, the main purpose of the **excitingscripts** package is to support the comprehensive suite of **exciting** tutorials (see Section 2.2). The code is distributed together with the **exciting** source code. To allow for more frequent updates, we also publish it as a standalone package in PyPI, available at <https://pypi.org/project/excitingscripts/>.

### 9.3 Computing elastic constants: **ElaStic**

The Python package **ElaStic** [331] allows users to calculate second and third-order elastic coefficients using **exciting** [332] or other electronic-structure codes such as Quantum Espresso [333, 334] and VASP [335]. The package has recently been fully rewritten using the newest Python standards, and many features have been updated to reduce the computational burden and facilitate integration into high-throughput workflows [336]. In order to speed up the selection of Lagrangian vectors, the MatID library is used, which is a robust Python API that uses Spglib [337]. To lessen the computational load, a new set of Lagrangian vectors are introduced. The new code presents an automated procedure to determine the optimal polynomial-fit order and the maximum strain to include in the fitting process. Finally, the code is modularized and configured via a YAML file so that it can be easily integrated into a jobflow workflow. These new additions allow one to run automated workflows to calculate elastic coefficients using **exciting** and other DFT codes.

### 9.4 Interface to SIRIUS

Complex systems, such as cells containing defects, large organic crystals, metal-organic frameworks, or surfaces and interface systems are hard to tackle with standard implementations. To overcome the memory and scalability limitations associated with such problems, **exciting** has been interfaced with SIRIUS [32], a domain-specific library for electronic-structure calculations. SIRIUS offers more opportunities for parallelization and improved efficiency, thus allowing **exciting** to efficiently handle much larger systems like large perovskites or interfaces. As reference cases, calculations for a pyrene-MoS<sub>2</sub> interface and BA<sub>2</sub>PbI<sub>4</sub> show that the **exciting**-SIRIUS interface achieves speedups of about 5× and 35×, respectively, compared to standard **exciting** runs.

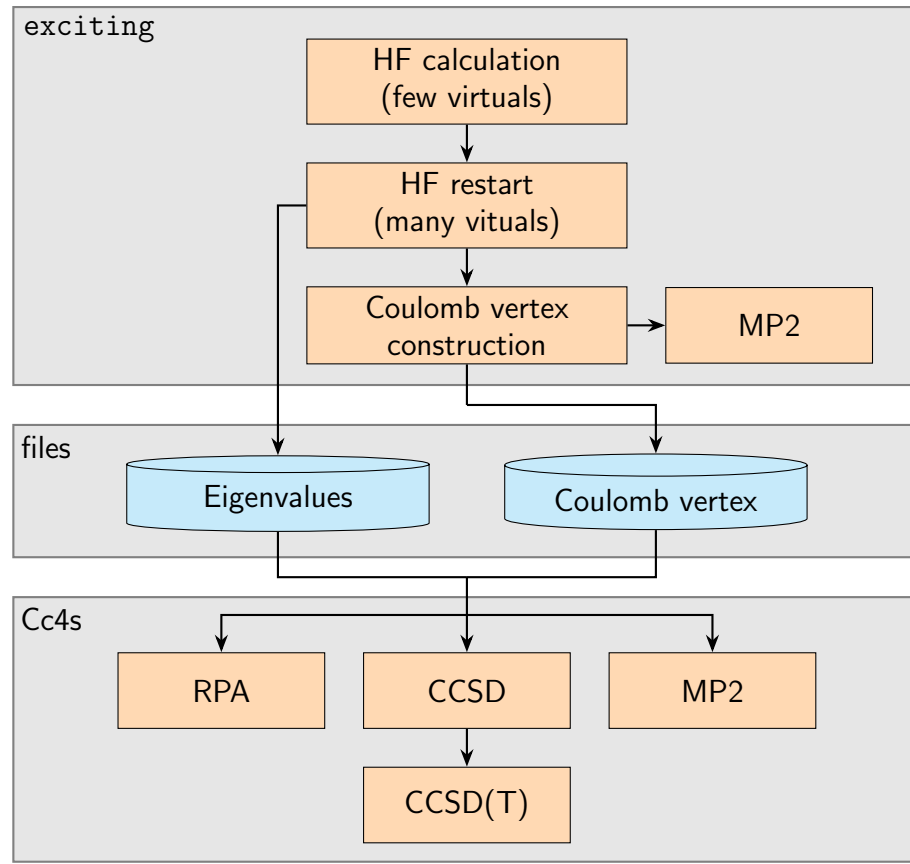


Figure 22: Workflow for correlation-energy calculations using Cc4s. The acronyms are explained in Section 9.5.

## 9.5 Coupled-cluster calculations through an interface to Cc4s

Cc4s is an open-source code [38] that implements quantum-chemistry methods [338–340] for solving the many-electron Schrödinger equation. The code is designed for periodic systems [341], but it also supports atoms and molecules. The workflow for computing the electron correlation energy is shown in Fig. 22. It consists of (i) reference HF calculations, (ii) computing the Coulomb vertex and band energies, and (iii) the correlation-energy calculation using the RPA, second-order Møller-Plesset perturbation theory (MP2), the CC method considering single and double excitations (CCSD) or beyond by considering triple excitations perturbatively in the CCSD(T) method. We implemented steps (i) and (ii) in `exciting`, and use the interface to Cc4s that carries away step (iii). This workflow has already been used in proof-of-principle calculations [342].

## 9.6 Transport calculation through an interface to elphbolt

The open-source software elphbolt [39] solves the coupled BTEs with the aid of Wannier-Fourier interpolation. `exciting` has the capability of computing MLWFs, phonons, and EPC constants. It thus allows for the export of the localized real-space representations of the electronic Hamiltonian, the dynamical matrices, and EPC matrix elements, which are then used as an input for elphbolt calculations.

## 10 Data handling and machine learning

### 10.1 State of the art

Data-centric approaches have become an important part of materials science. This also concerns electronic-structure theory, as summarized in a recent roadmap article [343]. High-quality data are crucial for the success of ML and are currently a major bottleneck [344]. Therefore, open materials databases are invaluable for overcoming this problem. Such databases are often established in the context of high-throughput calculations [325, 345–347], and their amount of data is growing rapidly. NOMAD [348, 349] has taken a different approach by inviting the electronic-structure community to contribute and share their data. Since it was opened to the public in 2014, almost 19 million entries from computational materials science have been published, including contributions from smaller projects and large high-throughput calculations. Through continuous development of the NOMAD software [349], an increasing number of computational techniques is now supported, including excited-state methods from MBPT, TDDFT, dynamical mean-field theory (DMFT), and MD. NOMAD also hosts benchmark data, for example, a comparison of x-ray spectra produced by three different codes, *i.e.*, Ocean, **exciting**, and XSPECTRA [350].

The NOMAD dataspace is often used for ML, *e.g.*, training a large language model (LLM) for crystal-structure prediction [351]. Combining ML with multi-scale modeling techniques, property prediction for disordered alloys has been demonstrated [40]. An emerging, most popular application of ML is the training of force fields. At the time of writing of this review, new models are published monthly [352]. We emphasize that NOMAD hosts the raw data of the Alexandria database [347], which is frequently used as training data for high-performing ML force fields. Beyond crystal structure optimization and prediction, ML models are used for predicting material properties directly from crystal structures [353, 354], classification tasks [355, 356], recommendation of novel compounds [357, 358], or crystal structure generation [359]. Due to the large number of recent publications, we refer the interested reader to reviews focused on the topic [360–362].

We note that there is a severe lack of available training data generated with higher-level methods. In fact, with a few exceptions, *e.g.*, Ref. [363], most ML models are trained on DFT results obtained with semi-local functionals. Moreover, there is a bottleneck what concerns error quantification of computational results, which would help to assess data quality and the impact of either methods and approximations or computational precision. Some work in this direction are studies dedicated to quantifying similarity [364, 365] and error estimates [28, 366].

**exciting** is well supported by the NOMAD data infrastructure. The output files created by **exciting** are recognized by NOMAD parsers, and their content is extracted according to the underlying metadata schema [367]. At present, NOMAD contains several ten thousand **exciting** calculations from 73 authors from all over the world, making it the 8th most used computational code on NOMAD.

### 10.2 Data-driven error quantification

The numerical precision of a calculation depends on the computational parameters, most importantly the BZ sampling and the basis-set quality (see Section 2.1). In order to quantify how computational settings affect a calculation’s precision, we can train ML models. Here, we choose the basis-set size as an example. This approach can be used to predict, for instance, the total energy of an expensive calculation from a less precise one and even to perform an extrapolation to the complete basis set (CBS) limit [366, 368]. CBS extrapolation facilitates the reuse of data by placing calculations from different sources on a more equal footing. By quantifying the precision of existing calculations, *e.g.*, from the NOMAD data infrastructure, the model can help reuse them for a different purpose. Typically, CBS extrapolation uses a series of calculations with an increasing basis-set size. In recent works, some of us have trained different models to predict the CBS energy from a single calculation, which is a more difficult task [28, 366]. We want to highlight one model here, which was trained using the symbolic regression method SISMO [369, 370]. Symbolic regression techniques have the benefit that the resulting model can be expressed as an arithmetic formula of the input features [355]. This makes the resulting models highly interpretable. In

the left panel of Fig. 23, we showcase the performance of such a model on a benchmark dataset from Ref. [28] consisting of diverse binary materials, computed with a systematic variation in the basis-set size from artificially low values to very large values. As a result, the energy differences between these calculations,  $\Delta E^{AB}$ , span several orders of magnitude. This makes the ML task more difficult [366]. By optimizing for the root-mean-squared-logarithmic-error (RMSLE) of  $\Delta E^{AB}$ , the SISSO model performs well across the target's wide range of values for the diverse set of materials in the test set [366]. It can be used to recommend, for a given material and a targeted tolerance in the resulting property, the optimal basis-set size for a computation. Recent work has expanded this focus to quantify the uncertainty in more complex properties such as the lattice parameters, band gaps, and the density of states with respect to the basis-set size and the  $k$ -point mesh [371].

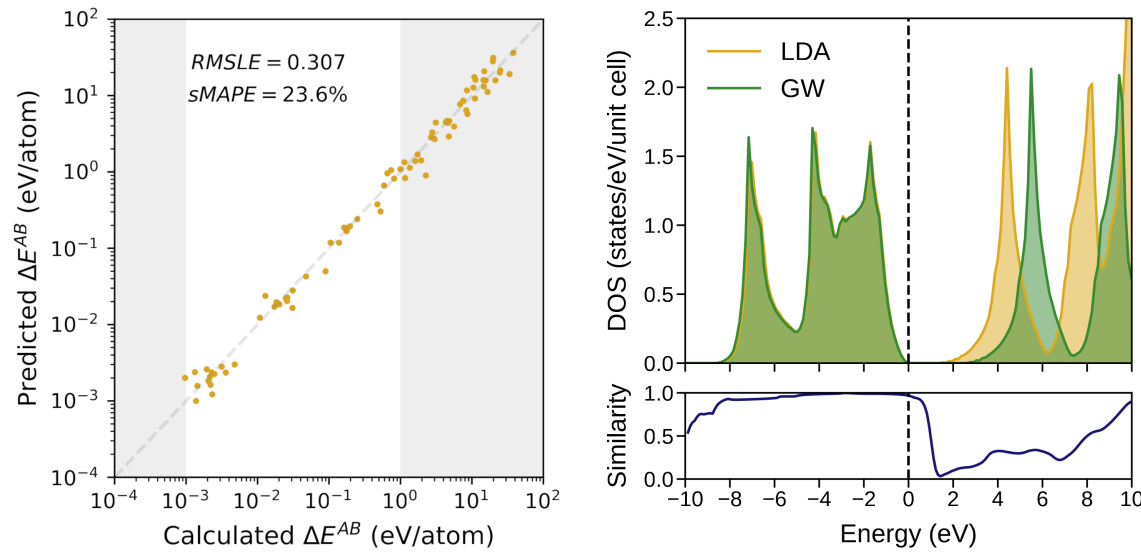


Figure 23: Examples of data-driven error quantification. Left: Results of a SISSO model to predict the delta to the CBS energies from the test data split, all calculated with `exciting`.  $\Delta E^{AB}$  refers to the difference in the total energy from a calculation done with basis-set size  $N_b$  and the CBS value [366]. Note the log-log scale to help visualize smaller  $\Delta E^{AB}$  values. Calculated  $\Delta E^{AB}$  values between 1 meV/atom and 1 eV/atom (white background) are of particular interest to DFT practitioners. Right: DOS of SiC [372], computed with LDA (yellow) and the *GW* approximation (green), aligned at the valence band maximum. Bottom right: Similarity between the LDA and the *GW* result as a function of energy.

The need for data-quality assessment concerns not only scalar quantities like energies, but also spectral properties. Typically, the assessment of spectra is performed qualitatively by visual inspection to analyze, for example results from different levels of theory. Applied to big data, *e.g.*, for large scale benchmark tests, this approach is not feasible. One way of approaching this challenge is the use of similarity metrics [364, 365, 373], which can be defined for any type of data and allow to quantify how (dis)similar results are. In the top right panel of Fig. 23, we show an example for this approach by presenting the DOS of SiC [372] computed by two different approaches, *i.e.*, at the DFT level, using the LDA functional, and at the *GW* level, using the  $G_0W_0$  approach on top of the LDA result. Comparing them, we observe the typical blue-shift of the conduction bands, since the *GW* result exhibits a larger band gap. We quantify this difference using the method described in Ref. [374]: We use fingerprints of the electronic structure[364], to encode the DOSs of both calculations in a small energy window around a selected reference energy. We then compare these fingerprints for a range of different reference energies, obtaining an energy-resolved quantitative measure of the similarity of the two DOSs, which is shown in the bottom right panel of Fig. 23. As a similarity metric, we use the Tanimoto coefficient[375]. In the valence bands, the two results overlap almost perfectly, resulting in a similarity value of almost 1. Around the Fermi level at 0 eV, the similarity drops sharply, due to the larger band-gap of the *GW* result. Identifying and quantifying the effect of different approximations on the results of electronic structure calculations is key to understanding, which material classes require which level of theory for an accurate description. Such tools are especially important for large-scale benchmarks and scans of the whole

materials space, as they allow to quickly assess the impact of different levels of theory to the computational results.

### 10.3 NOMAD Oasis for **exciting** data

The NOMAD software (see Section 10.1) can be installed locally for the organization of a research group's data or collaborations between groups. Such an installation, which can be customized to individual needs, is called NOMAD Oasis. The authors of this review manage an Oasis at the Humboldt-Universität zu Berlin, which is specifically configured for a research group focused on electronic-structure calculations. Starting with practicalities, we have increased, for example, the limit of unpublished uploads that a user can have. This allows group members to upload and share unfinished or even failed calculations for discussions with their colleagues. Increasing the allowed upload size makes it possible to share raw (binary) data that are too large for the central NOMAD instance. The Oasis is also accessible via the public internet, which allows for uploads directly from HPC centers. Obviously, the access to our Oasis is restricted to group members and collaborators, since it contains unpublished research.

Overall, we make use of the flexible setup of NOMAD Oasis: Individual components of the system, such as the database and web interface, are running in Docker (<https://www.docker.com/>) containers. We have extended the Oasis infrastructure by hosting a MongoDB (<https://www.mongodb.com/>) database in a container. This is shown in Fig. 24, where the gray box indicates the setup described here: A Jobflow database is running as a webservice next to the NOMAD Oasis. This configuration allows group members to upload and store workflow traces and other data produced by workflows implemented in **excitingworkf** (see Section 9.2), or any other framework based on jobflow-remote. At the same time, the input and output files are uploaded as raw data to the Oasis, where all relevant information is extracted from the raw files. This setup is specifically useful for running high-throughput workflows, since uploading and sharing can be automatized, making new data immediately available to collaborators.

Our setup has also benefits from an infrastructure point of view. From the users perspective, it simplifies the usage of different tools, since they can access different services under a single URL. For the administrator of the Oasis and the Jobflow database, the setup and maintenance of the services is simplified, since everything can be managed with a single configuration file. We provide the template for this setup at <https://github.com/exciting/sol-oasis>, including documentation for adopting it for other groups.

### 10.4 Building CE models with **exciting**, **CELL**, and **NOMAD**

Access to thermodynamic properties of materials with **exciting**, such as the ground states of alloys and order-disorder transitions, is made possible by building cluster expansion (CE) [376, 377] models based on training data computed with **exciting**. For this purpose, a workflow integrating **exciting** with **CELL** [40] and **NOMAD** has been implemented, which allows for creating training structures, computing them with **exciting**, uploading the data to the **NOMAD** Oasis (see Section 10.3), and finally creating accurate CE models for accessing various properties in a numerically efficient manner. The workflow is sketched in Fig. 24. First, an initial set of structures is created, as indicated by the red box in the top left. For all structures, DFT calculations are performed with **exciting** and the input and output files are uploaded to the **NOMAD** Oasis, where they are parsed and the computed properties are extracted. Using the **dbinterfaces** module of **CELL**, these results are then acquired from the Oasis and used as target values for the construction of a CE model with **CELL**. Then, derivative structures are sampled, *e.g.*, by generating all possible structures up to a certain supercell size, and their properties are predicted using the CE model. We then check for convergence. This typically involves evaluating if the model's cross validation score is below a target threshold (green box). Other criteria, as for instance verifying that no new ground state structures are found among the previously sampled structures (in the case that the total energy is the modeled property), may be relevant to determine convergence. If convergence is not achieved, we select additional derivative structures to increase the diversity and size of the training set. For this, we use different approaches that are discussed in more detail in Ref. [40]. For the new se-

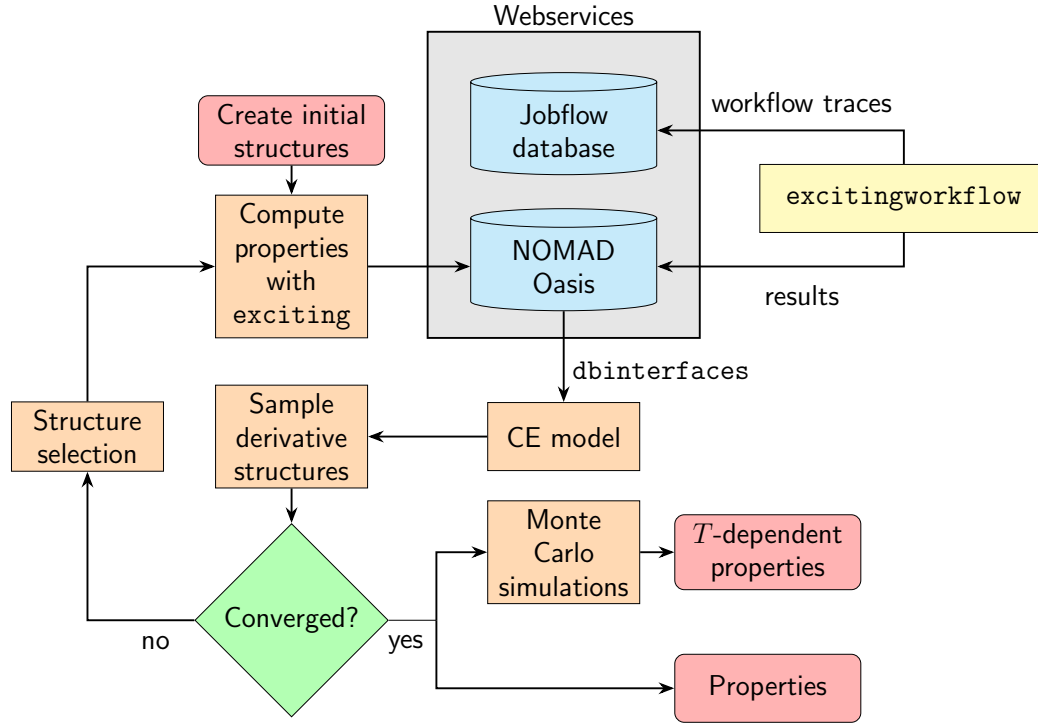


Figure 24: Integration of NOMAD infrastructure for different applications. Both a NOMAD Oasis and a Jobflow database (blue) are running as webservices (gray box). Top right: Interaction with workflows using the `excitingworkflow` framework (yellow box). Left: Workflow for building CE models with `exciting` data using an interface to the NOMAD Oasis. Individual workflow tasks are shown in orange, data are shown in red, and decision points are shown in green.

lected configurations, properties are again computed with `exciting` and uploaded to the Oasis. With the extended training set, we build a new CE model and the process is repeated until the model is converged. (We note that the same procedure also works with the public NOMAD instance.)

By modeling the total energy per particle, one can then perform statistical thermodynamics simulations on large supercells, *e.g.*, employing Metropolis Monte Carlo (MC) simulations with `CELL` [378]. This enables the prediction of temperature-dependent properties, such as the specific heat  $C_p$ . By modeling additional properties, as for instance the lattice parameters, one can calculate their MC average at different concentrations and temperatures. This workflow has been used to find the ground-state structures of the intermetallic clathrate alloy  $\text{Ba}_8\text{Al}_x\text{Si}_{46-x}$ , which is a promising material for thermoelectric applications. The so obtained models were used to describe its phase diagram [40]. Figure 25 shows the results of the workflow's iterative process. In the panel labeled "Iteration 1", starting from a set of random structures (black empty circles), a CE model was built. This model was used to sample derivative structures using simulated annealing (gray dots), yielding low-energy structures with predicted energies indicated by red dots. The latter were selected to enlarge the training set by computing their *ab initio* energies (red empty circles). In iteration 1, a significant disagreement between the computed and predicted energies indicates that convergence was not achieved. Therefore, following the workflow, the process was repeated in iterations 2 to 4, augmenting the training set in each iteration by adding lowest non-degenerate (LND) structures, resulting in a CE model with an accuracy of about 1 meV/atom. This workflow also allows for leveraging advanced ML techniques for the prediction of nonlinear properties, as demonstrated in Ref. [379], where non-linear CE models were used to predict, *e.g.*, the KS band gap of clathrates.

## 10.5 Visualizing Fermi surfaces: *FSvisual*

`exciting` can be used to calculate Fermi surfaces (FSs). The resulting data, *i.e.*, electronic band energies evaluated on a very dense  $\mathbf{k}$ -grid in the BZ, are stored in the human-readable `bxs` file format es-

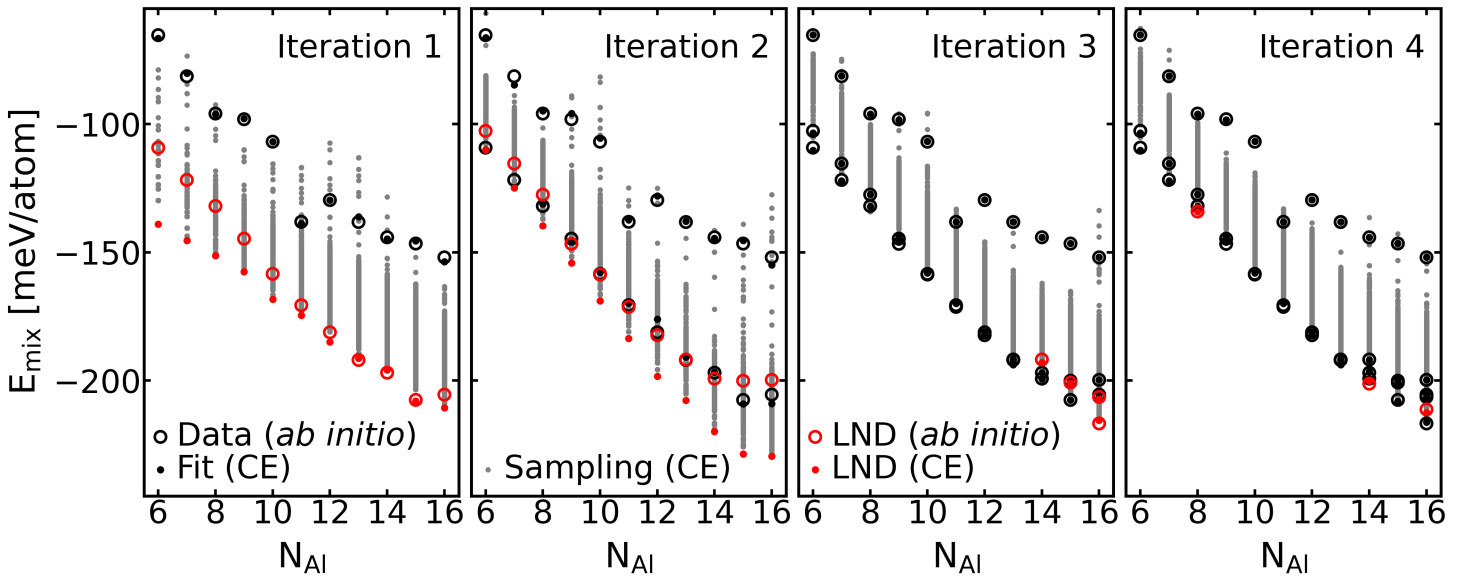


Figure 25: CE model construction with `exciting`, `CELL`, and `NOMAD` using the workflow of Fig. 24.  $N_{\text{Al}}$  is the number of Al substituents in the clathrate.

tablished by the XCrySDen software [380]. For visualization, we here introduce `FSvisual`, a Python-based, modular framework that offers interactive 3D viewing, allowing for rotation and zooming in. Unlike other, stand-alone, tools such as FermiSurfer [381] or XCrySDen, `FSvisual` generates HTML files for its visualizations by utilizing the capabilities of the Plotly [382] package. The resulting FS plots can be accessed easily, either directly or through any web browser, without the need for specialized software, and can be shared and embedded in websites as interactive widgets. As such, we plan to integrate `FSvisual` into `NOMAD` (see Section 10.1), to allow for interactive exploration of the uploaded data.

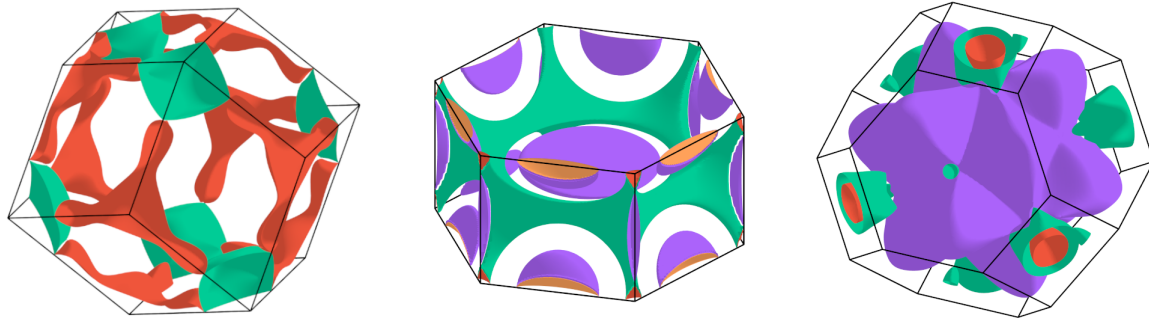


Figure 26: Fermi surfaces of Ba, Mg, and Ru (left to right), calculated using the PBEsol xc functional, inside the BZ (black lines) of the bcc, hcp, and fcc structures, respectively. The individual sheets of the FS can be distinguished by their color.

Figure 26 showcases the FSs of Ba, Mg, and Ru inside the respective BZs. Ba exhibits two open sheets (colored in red and green), while Mg shows four open sheets (colored in red, green, purple, and orange). Ru displays two open sheets (colored in red and green) alongside a closed sheet (colored in purple), as well as a closed sheet, hidden inside the purple one. Using `FSvisual`, each branch, and also the BZ, can be viewed individually. We used `FSvisual` to create interactive visualizations of the FSs of 37 elemental metals, which were computed using `exciting`. They can be explored at the `exciting` webpage, see [https://exciting-code.org/fermi\\_surfaces](https://exciting-code.org/fermi_surfaces). More details of the code and a detailed analysis of the data will be published elsewhere [383]. The source code is already available at <https://github.com/exciting/FSvisual>.

## 11 Outlook

**exciting** is always under active development, steadily extending its methodological scope and computational capabilities across ground state, excited state, and non-equilibrium simulations. Here, we list some topics that are currently under development and will be deployed in subsequent releases, or are on our wish list: For ground-state calculations, we are currently extending the hybrid-functional implementation to the spin-degrees of freedom, including consistent treatment of SOC. Also atomic forces and geometry optimization from hybrid functionals are in our focus. Our band-structure-unfolding code will be available soon. Current developments in the *GW* module include core-level *GW*. We aim at including lattice contributions to the polarizability for improved results for polar materials. Moreover, the effect of *GW* corrections to electron-phonon matrix elements will be evaluated. Future work may include the incorporation of vertex corrections within QSGW using xc kernels. Within the time-dependent DFT, developments in the RT-TDDFT module focuses on incorporating non-local, MBPT-derived self-energy operators and hybrid functionals to capture excitonic effects beyond the adiabatic approximation. Real-time simulations of pump-probe experiments involving core electrons will be implemented, along with an extension of real-time propagation to include SOC. Furthermore, the high accuracy of our full-potential all-electron LAPW+LO-based RT-TDDFT implementations will be leveraged to generate reliable benchmark-quality reference data. Continued developments of the BSE formalism will allow for extensions of the description of STEs in solids, including finite-temperature regimes. In addition, real-time exciton-phonon dynamics would aim at capturing the ultrafast formation and non-equilibrium evolution of STE states. Pump-probe spectroscopy will be extended towards photoexcited electron populations above the Fermi level, including Pauli-blocking effects on near-edge X-ray absorption. Furthermore, a non-equilibrium BSE-based pump-probe simulation framework will be integrated with nonadiabatic molecular dynamics. Finally, complementary efforts focus on improving and extending our workflows, enhancing usability of the code's functionality. Python interfaces and analysis tools will continue to be extended to support the latest developments. Verifying and understanding the convergence behavior of **exciting** will be supported by the creation and analysis of curated benchmark datasets, which will allow us to suggest input parameters for **exciting** calculations. With a focus on high-throughput calculations, we plan to further strengthen the integration of **excitingtools** and **excitingworkflow** with the NOMAD infrastructure. We will make use of **FSvisual** to visualize Fermi surfaces within the NOMAD framework. All developments are ideally accompanied by HPC-friendliness, making them highly parallelizable and computationally efficient. Collectively, these ongoing and planned developments reaffirm **exciting**'s position as a benchmark all-electron code, continuously expanding its portfolio of state-of-the-art theoretical spectroscopy features.

## Acknowledgement

Work supported by the European Union's Horizon 2020 research and innovation program under the grant agreement No. 951786 (NOMAD CoE), the German Science Foundation (DFG) through the Collaborative Research Center HIOS (SFB 951), Project No. 182087777, the Collaborative Research Center FONDA, Project No. 414984028, the priority program SPP2196 Perovskite Semiconductors, project No. 424709454, and the NFDI consortium FAIRmat Project No. 460197019. D. T. S. acknowledges support by the Max-Planck Graduate Center for Quantum Materials. N. F., D. T. and D. P.-G. acknowledge funding from the Volkswagen Foundation under Grant No. 96237. R. R. P. acknowledges computing time on the high-performance computer "Lise" at the NHR center NHR@ZIB. M.H. acknowledges the computing time provided on the high-performance computer Noctua 2 at the NHR Center PC<sup>2</sup>. The NHR center is jointly supported by the Federal Ministry of Education and Research and the state governments participating in the NHR, [www.nhr-verein.de](http://www.nhr-verein.de). We thank Alexander Buccheri, Maximilian Schebek, Ben Alex, Elisa Stephan, Fabian Nemitz, and Nora Sallas-Illanes for their valuable contributions to the **exciting** code.

## References

- [1] P. Hohenberg and W. Kohn, *Physical review* **136**, B864 (1964).
- [2] W. Kohn and L. J. Sham, *Physical review* **140**, A1133 (1965).
- [3] E. Runge and E. K. Gross, *Physical review letters* **52**, 997 (1984).
- [4] X. Cui, L. Wan, J. Liu, J. Yang, and W. Hu, *APL Computational Physics* **1** (2025), 10.1063/5.0292905.
- [5] D. Jacquemin, V. Wathélet, E. A. Perpète, and C. Adamo, *Journal of Chemical Theory and Computation* **5**, 2420 (2009).
- [6] C. Adamo and D. Jacquemin, *Chemical Society Reviews* **42**, 845 (2013).
- [7] M. E. Casida and M. Huix-Rotllant, *Annual review of physical chemistry* **63**, 287 (2012).
- [8] L. Hedin, *Phys. Rev.* **139**, A796 (1965).
- [9] E. E. Salpeter and H. A. Bethe, *Physical Review* **84**, 1232 (1951).
- [10] W. Hanke and L. J. Sham, *Physical Review B* **21**, 4656 (1980).
- [11] M. S. Hybertsen and S. G. Louie, *Physical Review B* **34**, 5390 (1986).
- [12] G. Strinati, *La Rivista del Nuovo Cimento* **11**, 1 (1988).
- [13] G. Onida, L. Reining, and A. Rubio, *Rev. Mod. Phys.* **74**, 601 (2002).
- [14] S. Albrecht, L. Reining, R. Del Sole, and G. Onida, *Phys. Rev. Lett.* **80**, 4510 (1998).
- [15] M. Rohlfing and S. G. Louie, *Physical Review B* **62**, 4927 (2000).
- [16] X. Gonze and C. Lee, *Physical Review B* **55**, 10355 (1997).
- [17] O. K. Andersen, *Physical Review B* **12**, 3060 (1975).
- [18] D. J. Singh and L. Nordström, *Planewaves, Pseudopotentials, and the LAPW Method*, 2nd ed. (Springer, Berlin, Heidelberg, 2006).
- [19] A. Gulans, A. Kozhevnikov, and C. Draxl, *Phys. Rev. B* **97**, 161105 (2018).
- [20] A. Gulans, S. Kontur, C. Meisenbichler, D. Nabok, P. Pavone, S. Rigamonti, S. Sagmeister, U. Werner, and C. Draxl, *Journal of Physics: Condensed Matter* **26**, 363202 (2014).
- [21] D. Nabok, A. Gulans, and C. Draxl, *Phys. Rev. B* **94**, 035118 (2016).
- [22] C. Vorwerk, B. Aurich, C. Cocchi, and C. Draxl, *Electronic Structure* **1** (2019), 10.1088/2516-1075/ab3123.
- [23] J. C. Slater, *Physical Review* **51**, 846 (1937).
- [24] O. Andersen, *Solid State Communications* **13**, 133 (1973).
- [25] D. J. Singh, *Physical Review B* **43**, 6388 (1991).
- [26] E. Sjöstedt, L. Nordström, and D. J. Singh, *Solid State Communications* **114**, 15 (2000).
- [27] H. Kleine, S. Lubeck, E. Stephan, A. Gulans, and C. Draxl, (2026), in preparation.
- [28] C. Carbogno, K. S. Thygesen, B. Bieniek, C. Draxl, L. M. Ghiringhelli, A. Gulans, O. T. Hofmann, K. W. Jacobsen, S. Lubeck, J. J. Mortensen, M. Strange, E. Wruss, and M. Scheffler, *npj Computational Materials* **8** (2022), 10.1038/s41524-022-00744-4.

- [29] C. Vona, S. Lubeck, H. Kleine, A. Gulans, and C. Draxl, Phys. Rev. B **108**, 235161 (2023).
- [30] S. Lehtola, C. Steigemann, M. J. T. Oliveira, and M. A. L. Marques, Software X **7**, 1 (2018).
- [31] T. Chachiyo and H. Chachiyo, Computational and Theoretical Chemistry **1172**, 112669 (2020).
- [32] “SIRIUS: Domain specific library for electronic structure calculations,” <https://github.com/electronic-structure/SIRIUS>, accessed: 07-01-2026.
- [33] N. Salas-Illanes, D. Nabok, and C. Draxl, Phys. Rev. B **106**, 045143 (2022).
- [34] R. R. Pela and C. Draxl, Electronic Structure **4**, 037001 (2022).
- [35] B. Maurer and C. Draxl, Journal of Open Source Software (2026), accepted for publication.
- [36] C. Vorwerk, F. Sottile, and C. Draxl, Physical Review Research **2** (2020), 10.1103/physrevresearch.2.042003.
- [37] C. W. Vorwerk, *Theoretical Spectroscopy of Ga<sub>2</sub>O<sub>3</sub>*, Ph.D. thesis, Humboldt-Universität zu Berlin, Mathematisch-Naturwissenschaftliche Fakultät (2021).
- [38] F. Hummel, A. Irmler, A. Gallo, K. Liao, T. Tsatsoulis, T. Schäfer, and A. Grüneis, “Cc4s,” .
- [39] N. H. Protik, C. Li, M. Pruneda, D. Broido, and P. Ordejón, npj Computational Materials **8**, 28 (2022).
- [40] S. Rigamonti, M. Troppenz, M. Kuban, A. Hübner, and C. Draxl, npj Computational Materials **10**, 195 (2024).
- [41] “Project jupyter <https://jupyter.org/>,” .
- [42] J. P. Perdew and K. Schmidt, AIP Conference Proceedings **577**, 1 (2001).
- [43] J. Sun, A. Ruzsinszky, and J. P. Perdew, Physical review letters **115**, 036402 (2015).
- [44] J. P. Perdew, W. Yang, K. Burke, Z. Yang, E. K. Gross, M. Scheffler, G. E. Scuseria, T. M. Henderson, I. Y. Zhang, A. Ruzsinszky, *et al.*, Proceedings of the national academy of sciences **114**, 2801 (2017).
- [45] R. Liu, D. Zheng, X. Liang, X. Ren, M. Chen, and W. Li, The Journal of Chemical Physics **159**, 074109 (2023).
- [46] A. H. Larsen, M. Kuisma, J. Löfgren, Y. Pouillon, P. Erhart, and P. Hyldgaard, Modelling and Simulation in Materials Science and Engineering **25**, 065004 (2017).
- [47] J. P. Perdew, M. Ernzerhof, and K. Burke, The Journal of Chemical Physics **105**, 9982 (1996), <https://doi.org/10.1063/1.472933> .
- [48] J. Heyd, G. E. Scuseria, and M. Ernzerhof, The Journal of chemical physics **118**, 8207 (2003).
- [49] J. Heyd, G. E. Scuseria, and M. Ernzerhof, J. Chem. Phys. **124**, 219906 (2006).
- [50] Z.-H. Cui, Y.-C. Wang, M.-Y. Zhang, X. Xu, and H. Jiang, The Journal of Physical Chemistry Letters **9**, 2338 (2018), pMID: 29669414, <https://doi.org/10.1021/acs.jpclett.8b00919> .
- [51] A. D. Becke, The Journal of chemical physics **98**, 5648 (1993).
- [52] F. Sagredo, M. Camarasa-Gómez, F. Ricci, A. Champagne, L. Kronik, and J. B. Neaton, Journal of Chemical Theory and Computation **21**, 5009 (2025), pMID: 40338203, <https://doi.org/10.1021/acs.jctc.5c00160> .
- [53] O. Gunnarsson and B. I. Lundqvist, Phys. Rev. B **13**, 4274 (1976).

[54] D. Langreth and J. Perdew, Solid State Communications **17**, 1425 (1975).

[55] I. Ying Zhang, R. Shi, and X. Ren, Electronic Structure **7**, 043002 (2025).

[56] O. K. Andersen, Physical Review B **12**, 3060 (1975).

[57] E. Sjöstedt, L. Nordström, and D. Singh, Solid state communications **114**, 15 (2000).

[58] D. J. Singh and L. Nordström, *Planewaves, pseudopotentials and the LAPW method* (Springer, 2006).

[59] K. Lejaeghere, G. Bihlmayer, T. Björkman, P. Blaha, S. Blügel, V. Blum, D. Caliste, I. E. Castelli, S. J. Clark, A. D. Corso, S. de Gironcoli, T. Deutsch, J. K. Dewhurst, I. D. Marco, C. Draxl, M. Dułak, O. Eriksson, J. A. Flores-Livas, K. F. Garrity, L. Genovese, P. Giannozzi, M. Giantomassi, S. Goedecker, X. Gonze, O. Gränäs, E. K. U. Gross, A. Gulans, F. Gygi, D. R. Hamann, P. J. Hasnip, N. A. W. Holzwarth, D. Iuşan, D. B. Jochym, F. Jollet, D. Jones, G. Kresse, K. Koepernik, E. Küçükbenli, Y. O. Kvashnin, I. L. M. Locht, S. Lubeck, M. Marsman, N. Marzari, U. Nitzsche, L. Nordström, T. Ozaki, L. Paulatto, C. J. Pickard, W. Poelmans, M. I. J. Probert, K. Refson, M. Richter, G.-M. Rignanese, S. Saha, M. Scheffler, M. Schlipf, K. Schwarz, S. Sharma, F. Tavazza, P. Thunström, A. Tkatchenko, M. Torrent, D. Vanderbilt, M. J. van Setten, V. V. Speybroeck, J. M. Wills, J. R. Yates, G.-X. Zhang, and S. Cottenier, Science **351**, aad3000 (2016), <https://www.science.org/doi/pdf/10.1126/science.aad3000> .

[60] A. Görling, Phys. Rev. B **53**, 7024 (1996).

[61] J. P. Perdew, K. Burke, and M. Ernzerhof, Phys. Rev. Lett. **77**, 3865 (1996).

[62] J. Doumont, F. Tran, and P. Blaha, Phys. Rev. B **105**, 195138 (2022).

[63] F. Tran, J. Doumont, P. Blaha, M. A. L. Marques, S. Botti, and A. P. Bartók, The Journal of Chemical Physics **151**, 161102 (2019).

[64] J. Uzulis, A. V. Sorokin, and A. Gulans, npj Computational Materials **11** (2025), 10.1038/s41524-025-01733-z.

[65] L. G. Ferreira, M. Marques, and L. K. Teles, Physical Review B **78**, 125116 (2008).

[66] R. R. Pela, M. Marques, and L. K. Teles, Journal of Physics: Condensed Matter **27**, 505502 (2015).

[67] R. R. Pelá, C. Caetano, M. Marques, L. G. Ferreira, J. Furthmüller, and L. K. Teles, Applied Physics Letters **98**, 151907 (2011).

[68] R. R. Pelá, M. Marques, L. G. Ferreira, J. Furthmüller, and L. K. Teles, Applied Physics Letters **100**, 202408 (2012).

[69] R. R. Pela, A. Gulans, and C. Draxl, Computer Physics Communications **220**, 263 (2017).

[70] L. G. Ferreira, R. R. Pelá, L. K. Teles, M. Marques, M. R. Jr., and J. Furthmüller, AIP Conference Proceedings **1566**, 27 (2013).

[71] R. R. Pela, A. Gulans, and C. Draxl, Journal of Chemical Theory and Computation (2018), 10.1021/acs.jctc.8b00518, 1805.09705 .

[72] R. Rodrigues Pela, U. Werner, D. Nabok, and C. Draxl, Phys. Rev. B **94**, 235141 (2016).

[73] R. R. Pela, C.-L. Hsiao, L. Hultman, J. Birch, and G. K. Gueorguiev, Physical Chemistry Chemical Physics (2024), 10.1039/d3cp05295h.

[74] C. Vona, D. Nabok, and C. Draxl, Advanced Theory and Simulations **5**, 2100496 (2022), <https://advanced.onlinelibrary.wiley.com/doi/pdf/10.1002/adts.202100496> .

[75] D. Zavickis, K. Kacars, J. Čimurs, and A. Gulans, *Phys. Rev. B* **106**, 165101 (2022).

[76] M. Betzinger, C. Friedrich, and S. Blügel, *Phys. Rev. B* **81**, 195117 (2010).

[77] L. Lin, *Journal of Chemical Theory and Computation* **12**, 2242 (2016), pMID: 27045571, <https://doi.org/10.1021/acs.jctc.6b00092> .

[78] F. Tran and P. Blaha, *Phys. Rev. B* **83**, 235118 (2011).

[79] J. Uzulis and A. Gulans, *Journal of Physics Communications* **6**, 085002 (2022).

[80] J. Uzulis and A. Gulans, “Hartree-fock limit for energies in solids,” (2026), in preparation.

[81] M. Weinert, *Journal of Mathematical Physics* **22**, 2433 (1981), <https://doi.org/10.1063/1.524800> .

[82] J. Kuneš, P. Novák, R. Schmid, P. Blaha, and K. Schwarz, *Physical Review B* **64**, 153102 (2001).

[83] J. Gavnholt, T. Olsen, M. Engelund, and J. Schiøtz, *Physical Review B* **78**, 075441 (2008).

[84] G. M. J. Barca, A. T. B. Gilbert, and P. M. W. Gill, *Journal of Chemical Theory and Computation* **14**, 1501 (2018).

[85] K. Carter-Fenk and J. M. Herbert, *Journal of Chemical Theory and Computation* **16**, 5067 (2020).

[86] T. Kowalczyk, S. R. Yost, and T. V. Voorhis, *The Journal of Chemical Physics* **134**, 054128 (2011).

[87] A. T. B. Gilbert, N. A. Besley, and P. M. W. Gill, *The Journal of Physical Chemistry A* **112**, 13164 (2008).

[88] J. Luo, X. Wang, S. Li, J. Liu, Y. Guo, G. Niu, L. Yao, Y. Fu, L. Gao, Q. Dong, C. Zhao, M. Leng, F. Ma, W. Liang, L. Wang, S. Jin, J. Han, L. Zhang, J. Etheridge, J. Wang, Y. Yan, E. H. Sargent, and J. Tang, *Nature* **563**, 541 (2018).

[89] T. C. Rossi, L. Qiao, C. P. Dykstra, R. Rodrigues Pela, R. Gnewkow, R. F. Wallick, J. H. Burke, E. Nicholas, A. M. March, G. Doumy, *et al.*, *Commun. Mater.* **6**, 191 (2025).

[90] L. Qiao, R. R. Pela, and C. Draxl, arXiv preprint arXiv:2509.07612 (2025).

[91] N. Marzari and D. Vanderbilt, **56**, 12847.

[92] I. Souza, N. Marzari, and D. Vanderbilt, **65**, 035109.

[93] A. Damle, A. Levitt, and L. Lin, **17**, 167.

[94] S. Tillack, A. Gulans, and C. Draxl, **101**, 235102.

[95] S. Tillack and C. Draxl, “Automatic Generation of Maximally Localized Wannier Functions via Optimized Projection Functions and Self-projections,” 2502.03213 .

[96] P. Blaha, K. Schwarz, F. Tran, R. Laskowski, G. K. Madsen, and L. D. Marks, *The Journal of chemical physics* **152** (2020).

[97] M. Zacharias, G. Volonakis, F. Giustino, and J. Even, **108**, 035155.

[98] S. Poncé and X. Gonze, “In search of the electron-phonon contribution to total energy,” 2512.04897 .

[99] S. Poncé, J.-M. Lihm, and C.-H. Park, **11**, 117.

[100] J.-M. Lihm and S. Poncé, “Beyond-quasiparticle transport with vertex correction: Self-consistent ladder formalism for electron-phonon interactions,” 2506.18139 .

[101] J. Lafuente-Bartolome, C. Lian, W. H. Sio, I. G. Gurtubay, A. Eiguren, and F. Giustino, **106**, 075119 () .

[102] J. Lafuente-Bartolome, C. Lian, W. H. Sio, I. G. Gurtubay, A. Eiguren, and F. Giustino, **129**, 076402 () .

[103] V. Vasilchenko, M. Giantomassi, S. Poncé, and X. Gonze, *Physical Review B* **112**, 014314 (2025).

[104] Y. Luo, J. Park, and M. Bernardi, *Nature Physics* **21**, 1275 (2025).

[105] Y. Luo, D. Desai, B. K. Chang, J. Park, and M. Bernardi, *Physical Review X* **14**, 021023 (2024).

[106] Y. Luo, *Physical Review Letters* **135** (2025), 10.1103/nmgj-yq1g.

[107] R. D. King-Smith and D. Vanderbilt, **47**, 1651.

[108] R. Resta and D. Vanderbilt, in *Physics of Ferroelectrics: A Modern Perspective* (Springer) pp. 31–68.

[109] S. Tillack, P. Pavone, and C. Draxl, “Density-functional perturbation theory within the (l)apw+lo method,” (2026), (in preparation).

[110] F. Giustino, M. L. Cohen, and S. G. Louie, **76**, 165108.

[111] C. Verdi and F. Giustino, **115**, 176401.

[112] H. J. Choi, M. L. Cohen, and S. G. Louie, **385**, 66.

[113] M. Lüders, A. Ernst, W. M. Temmerman, Z. Szotek, and P. J. Durham, *Journal of Physics: Condensed Matter* **13**, 8587 (2001).

[114] P. Mori-Sánchez, A. J. Cohen, and W. Yang, *Phys. Rev. Lett.* **100**, 146401 (2008).

[115] J. Sun, A. Ruzsinszky, and J. P. Perdew, *Phys. Rev. Lett.* **115**, 036402 (2015).

[116] L. Reining, *WIREs Computational Molecular Science* **8**, e1344 (2018), <https://wires.onlinelibrary.wiley.com/doi/pdf/10.1002/wcms.1344> .

[117] T. Aschebrock and S. Kümmel, *Phys. Rev. Res.* **1**, 033082 (2019).

[118] X. Gonze, F. Jollet, F. Abreu Araujo, D. Adams, B. Amadon, T. Applencourt, C. Audouze, J.-M. Beuken, J. Bieder, A. Bokhanchuk, E. Bousquet, F. Bruneval, D. Caliste, M. Côté, F. Dahm, F. Da Pieve, M. Delaveau, M. Di Gennaro, B. Dorado, C. Espejo, G. Geneste, L. Genovese, A. Gerossier, M. Giantomassi, Y. Gillet, D. Hamann, L. He, G. Jomard, J. Laflamme Janssen, S. Le Roux, A. Levitt, A. Lherbier, F. Liu, I. Lukačević, A. Martin, C. Martins, M. Oliveira, S. Poncé, Y. Pouillon, T. Rangel, G.-M. Rignanese, A. Romero, B. Rousseau, O. Rubel, A. Shukri, M. Stankovski, M. Torrent, M. Van Setten, B. Van Troeye, M. Verstraete, D. Waroquiers, J. Wiktor, B. Xu, A. Zhou, and J. Zwanziger, *Computer Physics Communications* **205**, 106 (2016).

[119] M. J. Verstraete, J. Abreu, G. E. Allemand, B. Amadon, G. Antonius, M. Azizi, L. Baguet, C. Barat, L. Bastogne, R. Béjaud, J.-M. Beuken, J. Bieder, A. Blanchet, F. Bottin, J. Bouchet, J. Bouquiaux, E. Bousquet, J. Boust, F. Brieuc, V. Brousseau-Couture, N. Brouwer, F. Bruneval, A. Castellano, E. Castiel, J.-B. Charraud, J. Clérouin, M. Côté, C. Duval, A. Gallo, F. Gendron, G. Geneste, P. Ghosez, M. Giantomassi, O. Gingras, F. Gómez-Ortiz, X. Gonze, F. A. Goudreault, A. Grüneis, R. Gupta, B. Guster, D. R. Hamann, X. He, O. Hellman, N. Holzwarth, F. Jollet, P. Kestener, I.-M. Lygatsika, O. Nadeau, L. MacEnulty, E. Marazzi, M. Mignolet, D. D. O'Regan, R. Outerovitch, C. Paillard, G. Petretto, S. Poncé, F. Ricci, G.-M. Rignanese, M. Rodriguez-Mayorga, A. H. Romero, S. Rostami, M. Royo, M. Sarraute, A. Sasani, F. Soubiran, M. Stengel, C. Tantardini, M. Torrent, V. Trinquet, V. Vasilchenko, D. Waroquiers, A. Zabalo, A. Zadoks, H. Zhang, and J. Zwanziger, *The Journal of Chemical Physics* **163**, 164126 (2025).

[120] M. Shishkin and G. Kresse, Phys. Rev. B **74**, 035101 (2006).

[121] M. Shishkin and G. Kresse, Phys. Rev. B **75**, 235102 (2007).

[122] F. Fuchs, J. Furthmüller, F. Bechstedt, M. Shishkin, and G. Kresse, Phys. Rev. B **76**, 115109 (2007).

[123] F. Hüser, T. Olsen, and K. S. Thygesen, Phys. Rev. B **87**, 235132 (2013).

[124] A. Kutepov, S. Y. Savrasov, and G. Kotliar, Phys. Rev. B **80**, 041103 (2009).

[125] A. Marini, C. Hogan, M. Grüning, and D. Varsano, Computer Physics Communications **180**, 1392 (2009).

[126] D. Sangalli, A. Ferretti, H. Miranda, C. Attaccalite, I. Marri, E. Cannuccia, P. Melo, M. Marsili, F. Paleari, A. Marrazzo, G. Prandini, P. Bonfà, M. O. Atambo, F. Affinito, M. Palummo, A. Molina Sanchez, C. Hogan, M. Grüning, D. Varsano, and A. Marini, Journal of Physics: Condensed Matter **31**, 325902 (2019).

[127] J. Deslippe, G. Samsonidze, D. A. Strubbe, M. Jain, M. L. Cohen, and S. G. Louie, Computer Physics Communications **183**, 1269 (2012).

[128] J. Wilhelm, M. Del Ben, and J. Hutter, Journal of Chemical Theory and Computation **12**, 3623 (2016).

[129] M. Graml, K. Zollner, D. Hernangómez-Pérez, P. E. Faria Junior, and J. Wilhelm, Journal of Chemical Theory and Computation **20**, 2202 (2024), pMID: 38353944, <https://doi.org/10.1021/acs.jctc.3c01230> .

[130] V. Blum, R. Gehrke, F. Hanke, P. Havu, V. Havu, X. Ren, K. Reuter, and M. Scheffler, Computer Physics Communications **180**, 2175 (2009).

[131] M. Azizi, F. A. Delesma, M. Giantomassi, D. Zavickis, M. Kuisma, K. Thygesen, D. Golze, A. Buccheri, M.-Y. Zhang, P. Rinke, C. Draxl, A. Gulans, and X. Gonze, Comput. Mater. Sci. **250**, 113655 (2025).

[132] F. Bruneval, F. Sottile, V. Olevano, R. Del Sole, and L. Reining, Phys. Rev. Lett. **94**, 186402 (2005).

[133] M. Gatti, F. Bruneval, V. Olevano, and L. Reining, Phys. Rev. Lett. **99**, 266402 (2007).

[134] J. Vidal, F. Trani, F. Bruneval, M. A. L. Marques, and S. Botti, Phys. Rev. Lett. **104**, 136401 (2010).

[135] M. J. van Setten, F. Caruso, S. Sharifzadeh, X. Ren, M. Scheffler, F. Liu, J. Lischner, L. Lin, J. R. Deslippe, S. G. Louie, C. Yang, F. Weigend, J. B. Neaton, F. Evers, and P. Rinke, Journal of Chemical Theory and Computation **11**, 5665 (2015).

[136] R. Rodrigues Pela, C. Vona, S. Lubeck, B. Alex, I. Gonzalez Oliva, and C. Draxl, npj Computational Materials **10**, 77 (2024).

[137] A. Tal, T. Bischoff, and A. Pasquarello, Proceedings of the National Academy of Sciences **121**, e2311472121 (2024), <https://www.pnas.org/doi/pdf/10.1073/pnas.2311472121> .

[138] M. Wen, V. Abraham, G. Harsha, A. Shee, K. B. Whaley, and D. Zgid, Journal of Chemical Theory and Computation **20**, 3109 (2024).

[139] F. Bruneval, N. Vast, and L. Reining, Phys. Rev. B **74**, 045102 (2006).

[140] M. van Schilfgaarde, T. Kotani, and S. Faleev, Phys. Rev. Lett. **96**, 226402 (2006).

[141] T. Kotani, M. van Schilfgaarde, and S. V. Faleev, Phys. Rev. B **76**, 165106 (2007).

[142] A. Kuteпов, K. Haule, S. Y. Savrasov, and G. Kotliar, Phys. Rev. B **85**, 155129 (2012).

[143] M. Grumet, P. Liu, M. Kaltak, J. c. v. Klimeš, and G. Kresse, Phys. Rev. B **98**, 155143 (2018).

[144] K. Haule and S. Mandal, Computer Physics Communications **295**, 108986 (2024).

[145] J. Lischner, D. Vigil-Fowler, and S. G. Louie, Phys. Rev. Lett. **110**, 146801 (2013).

[146] F. Caruso, H. Lambert, and F. Giustino, Phys. Rev. Lett. **114**, 146404 (2015).

[147] B. Gumhalter, V. Kovač, F. Caruso, H. Lambert, and F. Giustino, Phys. Rev. B **94**, 035103 (2016).

[148] P.-F. Loos, A. Marie, and A. Ammar, Faraday Discuss. **254**, 240 (2024).

[149] C. Mejuto-Zaera, G. Weng, M. Romanova, S. J. Cotton, K. B. Whaley, N. M. Tubman, and V. Vlček, The Journal of Chemical Physics **154**, 121101 (2021).

[150] A. L. Kuteпов, Phys. Rev. B **94**, 155101 (2016).

[151] A. L. Kuteпов, Phys. Rev. B **105**, 045124 (2022).

[152] P. S. Schmidt, C. E. Patrick, and K. S. Thygesen, Phys. Rev. B **96**, 205206 (2017).

[153] T. Olsen, C. E. Patrick, J. E. Bates, A. Ruzsinszky, and K. S. Thygesen, npj Computational Materials **5**, 106 (2019).

[154] Y.-H. Kim and A. Görling, Phys. Rev. Lett. **89**, 096402 (2002).

[155] M. Shishkin, M. Marsman, and G. Kresse, Phys. Rev. Lett. **99**, 246403 (2007).

[156] W. Chen and A. Pasquarello, Phys. Rev. B **92**, 041115 (2015).

[157] J. A. Berger, Phys. Rev. Lett. **115**, 137402 (2015).

[158] S. Rigamonti, S. Botti, V. Veniard, C. Draxl, L. Reining, and F. Sottile, Physical Review Letters **114**, 146402 (2015).

[159] A. Tal, W. Chen, and A. Pasquarello, Phys. Rev. B **103**, L161104 (2021).

[160] A. Grüneis, G. Kresse, Y. Hinuma, and F. Oba, Phys. Rev. Lett. **112**, 096401 (2014).

[161] P. B. Allen and M. Cardona, Phys. Rev. B **23**, 1495 (1981).

[162] F. Giustino, Rev. Mod. Phys. **89**, 015003 (2017).

[163] F. Bechstedt, K. Seino, P. H. Hahn, and W. G. Schmidt, Phys. Rev. B **72**, 245114 (2005).

[164] S. Botti and M. A. L. Marques, Phys. Rev. Lett. **110**, 226404 (2013).

[165] C. Friedrich, M. C. Müller, and S. Blügel, Phys. Rev. B **83**, 081101 (2011).

[166] M. Betzinger, C. Friedrich, A. Görling, and S. Blügel, Phys. Rev. B **92**, 245101 (2015).

[167] C. Freysoldt, P. Eggert, P. Rinke, A. Schindlmayr, R. Godby, and M. Scheffler, Computer Physics Communications **176**, 1 (2007).

[168] F. A. Rasmussen, P. S. Schmidt, K. T. Winther, and K. S. Thygesen, Phys. Rev. B **94**, 155406 (2016).

[169] “Greenx library,” <https://github.com/nomad-coe/greenX> (2024), accessed: 17-12-2025.

[170] “Idiel: Inverse dielectric library,” [https://github.com/mrm24/inverse\\_dielectric](https://github.com/mrm24/inverse_dielectric), accessed: 17-12-2025.

[171] H. N. Rojas, R. W. Godby, and R. J. Needs, Phys. Rev. Lett. **74**, 1827 (1995).

[172] P. Liu, M. Kaltak, J. c. v. Klimeš, and G. Kresse, Phys. Rev. B **94**, 165109 (2016).

[173] A. Kutepov, V. Oudovenko, and G. Kotliar, Computer Physics Communications **219**, 407 (2017).

[174] M. Azizi, J. Wilhelm, D. Golze, F. A. Delesma, R. L. Panadés-Barrueta, P. Rinke, M. Giantomassi, and X. Gonze, Phys. Rev. B **109**, 245101 (2024).

[175] D. Neuhauser, Y. Gao, C. Arntsen, C. Karshenas, E. Rabani, and R. Baer, Phys. Rev. Lett. **113**, 076402 (2014).

[176] V. c. v. Vlček, W. Li, R. Baer, E. Rabani, and D. Neuhauser, Phys. Rev. B **98**, 075107 (2018).

[177] F. Xuan, Y. Chen, and S. Y. Quek, Journal of Chemical Theory and Computation **15**, 3824 (2019).

[178] Z.-F. Liu, F. H. da Jornada, S. G. Louie, and J. B. Neaton, Journal of Chemical Theory and Computation **15**, 4218 (2019).

[179] M. Schebek, I. Gonzalez Oliva, and C. Draxl, Physical Review B **112**, 165130 (2025).

[180] H. Jiang, R. I. Gómez-Abal, X.-Z. Li, C. Meisenbichler, C. Ambrosch-Draxl, and M. Scheffler, Computer Physics Communications **184**, 348 (2013).

[181] M. Raya-Moreno, H. Kleine, S. Lubeck, B. Maurer, K. Sinha, M. Hossain, C. Draxl, and R. R. Pela, “Hpc-optimized, fully modular *gw* implementation in the all-electron full-potential code *exciting*,” (2026), (in preparation).

[182] F. Aryasetiawan and O. Gunnarsson, Phys. Rev. B **49**, 16214 (1994).

[183] P. Carrier, S. Rohra, and A. Görling, Phys. Rev. B **75**, 205126 (2007).

[184] F. H. da Jornada, D. Y. Qiu, and S. G. Louie, Phys. Rev. B **95**, 035109 (2017).

[185] X. Ren, F. Merz, H. Jiang, Y. Yao, M. Rampp, H. Lederer, V. Blum, and M. Scheffler, Phys. Rev. Mater. **5**, 013807 (2021).

[186] J. Spencer and A. Alavi, Phys. Rev. B **77**, 193110 (2008).

[187] S. Baroni and R. Resta, Phys. Rev. B **33**, 7017 (1986).

[188] C. Ambrosch-Draxl and J. O. Sofo, Computer Physics Communications **175**, 1 (2006).

[189] B. Alex, *Efficient Screening in Many-Body Calculations for Low-Dimensional Materials*, Master’s thesis, Humboldt-Universität zu Berlin (2023).

[190] R. Gómez-Abal, X. Li, M. Scheffler, and C. Ambrosch-Draxl, Phys. Rev. Lett. **101**, 106404 (2008).

[191] X.-Z. Li, R. Gómez-Abal, H. Jiang, C. Ambrosch-Draxl, and M. Scheffler, New Journal of Physics **14**, 023006 (2012).

[192] I. Gonzalez Oliva, F. Caruso, P. Pavone, and C. Draxl, Physical Review Materials **6**, 054004 (2022).

[193] I. Gonzalez Oliva, B. Maurer, B. Alex, S. Tillack, M. Schebek, and C. Draxl, physica status solidi (a) **221**, 2300170 (2024).

[194] W. Bennecke, I. Gonzalez Oliva, J. P. Bange, P. Werner, D. Schmitt, M. Merboldt, A. M. Seiler, K. Watanabe, T. Taniguchi, D. Steil, R. T. Weitz, P. Puschnig, C. Draxl, G. S. M. Jansen, M. Reutzel, and S. Mathias, *Nature Physics* (2025), 10.1038/s41567-025-03075-5.

[195] F. Henneke, L. Lin, C. Vorwerk, C. Draxl, R. Klein, and C. Yang, *Communications in Applied Mathematics and Computational Science* **15**, 89 (2020).

[196] A. M. Alvertis, A. Champagne, M. Del Ben, F. H. da Jornada, D. Y. Qiu, M. R. Filip, and J. B. Neaton, *Phys. Rev. B* **108**, 235117 (2023).

[197] M. Shao, F. H. da Jornada, L. Lin, C. Yang, J. Deslippe, and S. G. Louie, *SIAM Journal on Matrix Analysis and Applications* **39**, 683 (2018).

[198] W. Hu, M. Shao, A. Cepellotti, F. H. da Jornada, L. Lin, K. Thicke, C. Yang, and S. G. Louie, in *Computational Science – ICCS 2018*, edited by Y. Shi, H. Fu, Y. Tian, V. V. Krzhizhanovskaya, M. H. Lees, J. Dongarra, and P. M. A. Sloot (Springer International Publishing, 2018) pp. 604–617.

[199] P.-F. Loos and X. Blase, *The Journal of Chemical Physics* **153**, 114120 (2020).

[200] X. Zhang, J. A. Leveillee, and A. Schleife, *Physical Review B* **107**, 235205 (2023).

[201] T. Olsen, *Physical Review Letters* **127**, 166402 (2021).

[202] E. Perfetto, D. Sangalli, A. Marini, and G. Stefanucci, *Physical Review B* **92**, 205304 (2015).

[203] D. Sangalli, S. Dal Conte, C. Manzoni, G. Cerullo, and A. Marini, *Physical Review B* **93**, 195205 (2016).

[204] N. Farahani and D. Popova-Gorelova, *Phys. Rev. B* **110**, 235126 (2024).

[205] J. Vinson, T. Jach, M. Müller, R. Unterumsberger, and B. Beckhoff, *Phys. Rev. B* **96**, 205116 (2017).

[206] C. Vorwerk, F. Sottile, and C. Draxl, *Physical Chemistry Chemical Physics* **24**, 17439–17448 (2022).

[207] A. Marini, *Physical Review Letters* **101**, 106405 (2008).

[208] M. R. Filip, J. B. Haber, and J. B. Neaton, *Phys. Rev. Lett.* **127**, 067401 (2021).

[209] Y.-h. Chan, J. B. Haber, M. H. Naik, J. B. Neaton, D. Y. Qiu, F. H. da Jornada, and S. G. Louie, *Nano Letters* **23**, 3971 (2023).

[210] A. M. Alvertis, J. B. Haber, Z. Li, C. J. N. Coveney, S. G. Louie, M. R. Filip, and J. B. Neaton, *Proceedings of the National Academy of Sciences* **121**, e2403434121 (2024).

[211] M. Schebek, P. Pavone, C. Draxl, and F. Caruso, *Journal of Physics: Materials* **8**, 025006 (2025).

[212] M. Yang and C. Draxl, “Novel approach to structural relaxation of materials in optically excited states,” (2022), arXiv:2212.13645 [physics.comp-ph].

[213] Y. Bai, Y. Wang, and S. Meng, *133*, 046903 (2024).

[214] Z. Dai, C. Lian, J. Lafuente-Bartolome, and F. Giustino, *132*, 036902 (2024).

[215] Z. Dai, C. Lian, J. Lafuente-Bartolome, and F. Giustino, *109*, 045202 (2024).

[216] H. Ehrenreich and M. H. Cohen, *Physical Review* **115**, 786 (1959).

[217] K. Dong, W. Hu, and L. Lin, *Journal of Chemical Theory and Computation* **14**, 1311 (2018).

[218] E. Richter, B. Maurer, and C. Draxl, (2026), in preparation.

[219] C. Vorwerk, “BRIXS,” <https://github.com/exciting/BRIXS/> (2021).

[220] C. Vorwerk, “BRIXS,” <https://github.com/exciting/pyBRIXS/> (2021).

[221] P. Giannozzi, S. de Gironcoli, P. Pavone, and S. Baroni, Phys. Rev. B **43**, 7231 (1991).

[222] F. Bechstedt and J. Furthmüller, Applied Physics Letters **114**, 122101 (2019).

[223] A. Schleife, M. D. Neumann, N. Esser, Z. Galazka, A. Gottwald, J. Nixdorf, R. Goldhahn, and M. Feneberg, New Journal of Physics **20**, 053016 (2018).

[224] P. Umari, E. Mosconi, and F. De Angelis, The Journal of Physical Chemistry Letters **9**, 620 (2018).

[225] F. Fuchs, C. Rödl, A. Schleife, and F. Bechstedt, Phys. Rev. B **78**, 085103 (2008).

[226] L. Adamska and P. Umari, Phys. Rev. B **103**, 075201 (2021).

[227] M. Bokdam, T. Sander, A. Stroppa, S. Picozzi, D. D. Sarma, C. Franchini, and G. Kresse, Scientific Reports **6**, 28618 (2016).

[228] H.-Y. Chen, D. Sangalli, and M. Bernardi, **125**, 107401 (2020).

[229] N. Ferré, M. Filatov, and M. Huix-Rotllant, eds., *Density-Functional Methods for Excited States* (Springer, 2015).

[230] C. A. Ullrich, APL Computational Physics **1** (2025), 10.1063/5.0297117.

[231] R. R. Pela and C. Draxl, Electronic Structure **3**, 037001 (2021).

[232] C. Pemmaraju, New Journal of Physics **22**, 083063 (2020).

[233] N. T. Maitra, The Journal of Chemical Physics **144** (2016), 10.1063/1.4953039.

[234] C. A. Ullrich and Z.-h. Yang, Brazilian Journal of Physics **44**, 154 (2014).

[235] Z. A. Moldabekov, S. Schwalbe, T. Grawne, T. R. Preston, J. Vorberger, and T. Dornheim, Matter and Radiation at Extremes **10**, 047601 (2025), 2502.04921 .

[236] T. Skovhus, T. Olsen, and H. M. Rønnow, Physical Review Materials **6**, 054402 (2022).

[237] X. Xu and R. Long, ACS nano (2025), 10.1021/acs.nano.5c13647.

[238] J. T. Taylor, D. J. Tozer, and B. F. E. Curchod, The Journal of Physical Chemistry A **128**, 5314 (2024).

[239] S. Tussupbayev, N. Govind, K. Lopata, and C. J. Cramer, Journal of Chemical Theory and Computation **11**, 1102 (2015).

[240] H. Zhao and L. He, Journal of Chemical Theory and Computation **21**, 3335 (2025).

[241] S. A. Sato, H. Hübener, U. D. Giovannini, and A. Rubio, npj Computational Materials **11**, 233 (2025).

[242] J. I. Fuks, K. Luo, E. D. Sandoval, and N. T. Maitra, Physical Review Letters **114**, 183002 (2015), 1412.0586 .

[243] B. Buades, A. Picón, E. Berger, I. León, N. D. Palo, S. L. Cousin, C. Cocchi, E. Pellegrin, J. H. Martin, S. Mañas-Valero, E. Coronado, T. Danz, C. Draxl, M. Uemoto, K. Yabana, M. Schultze, S. Wall, M. Zürch, and J. Biegert, Applied Physics Reviews **8**, 011408 (2021), 1808.06493 .

[244] J. Simoni, X. Andrade, W. Fang, A. C. Grieder, A. A. Correa, T. Ogitsu, and Y. Ping, *APL Computational Physics* **1** (2025), 10.1063/5.0290737.

[245] F. Caruso, M. A. Sentef, C. Attaccalite, M. Bonitz, C. Draxl, U. D. Giovannini, M. Eckstein, R. Ernstorfer, M. Fechner, M. Grüning, H. Hübener, J.-P. Joost, D. M. Juraschek, C. Karrasch, D. M. Kennes, S. Latini, I.-T. Lu, O. Neufeld, E. Perfetto, L. Rettig, R. R. Pela, A. Rubio, J. F. Rudzinski, M. Ruggenthaler, D. Sangalli, M. Schüler, S. Shallcross, S. Sharma, G. Stefanucci, and P. Werner, *Journal of Physics: Materials* **9**, 012501 (2026).

[246] C. Shepard, R. Zhou, D. C. Yost, Y. Yao, and Y. Kanai, *The Journal of Chemical Physics* **155**, 100901 (2021).

[247] Y. Shinohara, S. Sato, K. Yabana, J.-I. Iwata, T. Otobe, and G. Bertsch, *The Journal of Chemical Physics* **137** (2012), 10.1063/1.4739844.

[248] C. Andrea Rozzi, S. Maria Falke, N. Spallanzani, A. Rubio, E. Molinari, D. Brida, M. Maiuri, G. Cerullo, H. Schramm, J. Christoffers, *et al.*, *Nature communications* **4**, 1602 (2013).

[249] A. V. Krasheninnikov, Y. Miyamoto, and D. Tománek, *Physical review letters* **99**, 016104 (2007).

[250] S. Andermatt, J. Cha, F. Schiffmann, and J. VandeVondele, *Journal of chemical theory and computation* **12**, 3214 (2016).

[251] R. Long and O. V. Prezhdo, *Journal of the American Chemical Society* **133**, 19240 (2011).

[252] V. Blum, R. Asahi, J. Autschbach, C. Bannwarth, G. Bihlmayer, S. Blügel, L. A. Burns, T. D. Crawford, W. Dawson, W. A. d. Jong, C. Draxl, C. Filippi, L. Genovese, P. Giannozzi, N. Govind, S. Hammes-Schiffer, J. R. Hammond, B. Hourahine, A. Jain, Y. Kanai, P. R. C. Kent, A. H. Larsen, S. Lehtola, X. Li, R. Lindh, S. Maeda, N. Makri, J. Moussa, T. Nakajima, J. A. Nash, M. J. T. Oliveira, P. D. Patel, G. Pizzi, G. Pourtois, B. P. Pritchard, E. Rabani, M. Reiher, L. Reining, X. Ren, M. Rossi, H. B. Schlegel, N. Seriani, L. V. Slipchenko, A. Thom, E. F. Valeev, B. V. Troeye, L. Visscher, V. Vlček, H.-J. Werner, D. B. Williams-Young, and T. L. Windus, *Electronic Structure* **6**, 042501 (2024).

[253] J. Lloyd-Hughes, P. M. Oppeneer, T. P. d. Santos, A. Schleife, S. Meng, M. A. Sentef, M. Ruggenthaler, A. Rubio, I. Radu, M. Murnane, X. Shi, H. Kapteyn, B. Stadtmüller, K. M. Dani, F. H. d. Jornada, E. Prinz, M. Aeschlimann, R. L. Milot, M. Buranova, J. Boland, T. Cocker, and F. Hegmann, *Journal of Physics: Condensed Matter* **33**, 353001 (2021).

[254] S. Kümmel, *Advanced Energy Materials* **7**, 1700440 (2017).

[255] J. Authier and P.-F. Loos, *The Journal of Chemical Physics* **153**, 184105 (2020), 2008.13143 .

[256] N. T. Maitra, *Journal of Physics: Condensed Matter* **29**, 423001 (2017).

[257] A. K. Manna, S. Refaelly-Abramson, A. M. Reilly, A. Tkatchenko, J. B. Neaton, and L. Kronik, *Journal of Chemical Theory and Computation* **14**, 2919 (2018).

[258] S. Refaelly-Abramson, M. Jain, S. Sharifzadeh, J. B. Neaton, and L. Kronik, *Physical Review B* **92**, 081204 (2015).

[259] A. Mahler, J. Williams, N. Q. Su, and W. Yang, *Physical Review B* **106**, 035147 (2022), 2202.01870 .

[260] C. Pemmaraju, *Computational Condensed Matter* **18**, e00348 (2019).

[261] Y.-M. Byun, J. Sun, and C. A. Ullrich, *Electronic Structure* **2**, 023002 (2020).

[262] A. Gomez Pueyo, M. A. Marques, A. Rubio, and A. Castro, *Journal of chemical theory and computation* **14**, 3040 (2018).

[263] L. Reining, V. Olevano, A. Rubio, and G. Onida, *Physical review letters* **88**, 066404 (2002).

[264] S. Botti, A. Fourreau, F. Nguyen, Y.-O. Renault, F. Sottile, and L. Reining, *Physical Review B—Condensed Matter and Materials Physics* **72**, 125203 (2005).

[265] S. Sharma, J. K. Dewhurst, A. Sanna, and E. K. U. Gross, *Phys. Rev. Lett.* **107**, 186401 (2011).

[266] A. Marini, R. Del Sole, and A. Rubio, *Physical review letters* **91**, 256402 (2003).

[267] F.-R. Fan, H. Wu, D. Nabok, S. Hu, W. Ren, C. Draxl, and A. Stroppa, *Journal of the American Chemical Society* **139**, 12883 (2017).

[268] S. Sagmeister, *Excitonic Effects in Solids: Time-Dependent Density Functional Theory versus the Bethe-Salpeter Equation*, Ph.D. thesis (2009).

[269] S. Sagmeister and C. Ambrosch-Draxl, *Physical Chemistry Chemical Physics* **11**, 4451 (2009).

[270] R. R. Pela and C. Draxl, *Computer Physics Communications* **304**, 109292 (2024).

[271] A. Scherrer, F. Agostini, D. Sebastiani, E. Gross, and R. Vuilleumier, *Physical Review X* **7**, 031035 (2017).

[272] B. F. E. Curchod, U. Rothlisberger, and I. Tavernelli, *ChemPhysChem* **14**, 1314 (2013).

[273] R. Crespo-Otero and M. Barbatti, *Chemical Reviews* **118**, 7026 (2018).

[274] P. You, D. Chen, C. Lian, C. Zhang, and S. Meng, *Wiley Interdisciplinary Reviews: Computational Molecular Science* **11** (2021), 10.1002/wcms.1492.

[275] T. R. Nelson, A. J. White, J. A. Bjorgaard, A. E. Sifain, Y. Zhang, B. Nebgen, S. Fernandez-Alberti, D. Mozyrsky, A. E. Roitberg, and S. Tretiak, *Chemical reviews* **120**, 2215 (2020).

[276] J. C. Tully, *The Journal of Chemical Physics* **93**, 1061 (1990).

[277] A. Ojanperä, V. Havu, L. Lehtovaara, and M. Puska, *The Journal of Chemical Physics* **136**, 144103 (2012).

[278] F. Wang, C. Y. Yam, L. Hu, and G. Chen, *The Journal of Chemical Physics* **135**, 044126 (2011).

[279] C. Aversa and J. E. Sipe, *Phys. Rev. B* **52**, 14636 (1995).

[280] K. S. Virk and J. E. Sipe, *Phys. Rev. B* **76**, 035213 (2007).

[281] G. F. Bertsch, J.-I. Iwata, A. Rubio, and K. Yabana, *Phys. Rev. B* **62**, 7998 (2000).

[282] C. D. Pemmaraju, F. D. Vila, J. J. Kas, S. A. Sato, J. J. Rehr, K. Yabana, and D. Prendergast, *Computer Physics Communications* **226**, 30 (2018).

[283] R. Del Sole and R. Girlanda, *Phys. Rev. B* **48**, 11789 (1993).

[284] D. Sangalli, J. A. Berger, C. Attaccalite, M. Grüning, and P. Romaniello, *Phys. Rev. B* **95**, 155203 (2017).

[285] I. Souza, J. Íñiguez, and D. Vanderbilt, *Physical Review B* **69**, 085106 (2004).

[286] C. Attaccalite and M. Grüning, *Physical Review B—Condensed Matter and Materials Physics* **88**, 235113 (2013).

[287] G. A. Baraff and M. Schlüter, *Phys. Rev. B* **30**, 3460 (1984).

[288] D. Tumakov and D. Popova-Gorelova, (2026), in preparation.

[289] R. King-Smith and D. Vanderbilt, *Physical Review B* **47**, 1651 (1993).

[290] R. Resta, *Reviews of modern physics* **66**, 899 (1994).

[291] F. Paleari, T. Galvani, H. Amara, F. Ducastelle, A. Molina-Sánchez, and L. Wirtz, *2D Materials* **5**, 045017 (2018).

[292] A. Ashoka, R. R. Tamming, A. V. Girija, H. Bretscher, S. D. Verma, S.-D. Yang, C.-H. Lu, J. M. Hodgkiss, D. Ritchie, C. Chen, *et al.*, *Nat. Commun.* **13**, 1437 (2022).

[293] A. Montanaro, F. Giusti, M. Colja, G. Brajnik, A. Marciniak, R. Sergo, D. De Angelis, F. Glerean, G. Sparapassi, G. Jarc, *et al.*, *Rev. Sci. Instrum.* **91** (2020).

[294] M. Rebholz, T. Ding, V. Despré, L. Aufleger, M. Hartmann, K. Meyer, V. Stooß, A. Magunia, D. Wachs, P. Birk, *et al.*, *Phys. Rev. X* **11**, 031001 (2021).

[295] R. Geneaux, H. J. Marroux, A. Guggenmos, D. M. Neumark, and S. R. Leone, *Philos. Trans. R. Soc., A* **377**, 20170463 (2019).

[296] D. Garratt, L. Misiekis, D. Wood, E. Witting-Larsen, M. Matthews, O. Alexander, P. Ye, S. Jarosch, A. Bakulin, T. Penfold, and J. Marangos, *2021 Conference on Lasers and Electro-Optics Europe and European Quantum Electronics Conference*, 2021 Conference on Lasers and Electro-Optics Europe and European Quantum Electronics Conference , jsiii\_2\_4 (2021).

[297] D. Garratt, L. Misiekis, D. Wood, E. W. Larsen, M. Matthews, O. Alexander, P. Ye, S. Jarosch, C. Ferchaud, C. Strüber, A. S. Johnson, A. A. Bakulin, and J. P. Penfold, T. J. Marangos, *Nature Communications* **13**, 3414 (2022).

[298] P. Hillyard, S. Kuchibhatla, T. Glover, M. Hertlein, N. Huse, P. Nachimuthu, L. Saraf, S. Thevuthasan, and K. Gaffney, *Physical Review B* **80**, 125210 (2009).

[299] T. Palmieri, E. Baldini, A. Steinhoff, A. Akrap, M. Kollár, E. Horváth, L. Forró, F. Jahnke, and M. Chergui, *Nature communications* **11**, 850 (2020).

[300] M. Zürch, H.-T. Chang, L. J. Borja, P. M. Kraus, S. K. Cushing, A. Gandman, C. J. Kaplan, M. H. Oh, J. S. Prell, D. Prendergast, C. D. Pemmaraju, D. M. Neumark, and S. R. Leone, *Nature Communications* **8**, 15734 (2017).

[301] D. Garratt, M. Matthews, and J. Marangos, *Structural Dynamics* **11**, 010901 (2024).

[302] A. Picón, L. Plaja, and J. Biegert, *New Journal of Physics* **21**, 043029 (2019).

[303] G. Cistaro, M. Malakhov, J. J. Esteve-Paredes, A. J. Uría-Álvarez, R. E. F. Silva, F. Martín, J. J. Palacios, and A. Picón, *Journal of Chemical Theory and Computation* **19**, 333 (2023).

[304] M. Malakhov, G. Cistaro, F. Martín, and A. Picón, *Communications Physics* **7**, 196 (2024).

[305] T. Hansen, T. Bezriadina, and D. Popova-Gorelova, *Molecules* **28**, 4502 (2023).

[306] S. Pabst, A. Sytcheva, A. Moulet, A. Wirth, E. Goulielmakis, and R. Santra, *Phys. Rev. A: At., Mol., Opt. Phys.* **86**, 063411 (2012).

[307] A. S. Skeidsvoll, A. Balbi, and H. Koch, *Phys. Rev. A* **102**, 023115 (2020).

[308] D. Sangalli, M. D'Alessandro, and C. Attaccalite, *Physical Review B* **107**, 205203 (2023).

[309] J. Vinson, *Physical Chemistry Chemical Physics* **24**, 12787 (2022).

[310] I. M. Klein, A. Krotz, W. Lee, J. M. Michelsen, and S. K. Cushing, *The Journal of Physical Chemistry C* **127** (2023).

[311] I. M. Klein, H. Liu, D. Nimlos, A. Krotz, and S. K. Cushing, *Journal of the American Chemical Society* **144**, 12834 (2022).

[312] N. Farahani, “PreXAS-Exciton,” <https://github.com/nasrinfarahan/PreXAS-Exciton> (2024).

[313] M. Poul, L. Huber, and J. Neugebauer, *npj Computational Materials* **11** (2025), 10.1038/s41524-025-01669-4.

[314] M. Bonacci, J. Qiao, N. Spallanzani, A. Marrazzo, G. Pizzi, E. Molinari, D. Varsano, A. Ferretti, and D. Prezzi, *npj Computational Materials* **9** (2023), 10.1038/s41524-023-01027-2.

[315] D. Speckhard, M. Kuban, C. Koch, J. Rudzinzki, and C. Draxl, in *Workflow Systems for Large-Scale Scientific Data Analysis*, edited by U. Leser, M. Hilbrich, S. Wilkinson, and R. Ferreira da Silva (Berlin University Press, 2025).

[316] X. Gonze, B. Amadon, G. Antonius, F. Arnardi, L. Baguet, J.-M. Beuken, J. Bieder, F. Bottin, J. Bouchet, E. Bousquet, N. Brouwer, F. Bruneval, G. Brunin, T. Cavignac, J.-B. Charraud, W. Chen, M. Côté, S. Cottenier, J. Denier, G. Geneste, P. Ghosez, M. Giantomassi, Y. Gillet, O. Gingras, D. R. Hamann, G. Hautier, X. He, N. Helbig, N. Holzwarth, Y. Jia, F. Jollet, W. Lafargue-Dit-Hauret, K. Lejaeghere, M. A. Marques, A. Martin, C. Martins, H. P. Miranda, F. Naccarato, K. Persson, G. Petretto, V. Planes, Y. Pouillon, S. Prokhorenko, F. Ricci, G.-M. Rignanese, A. H. Romero, M. M. Schmitt, M. Torrent, M. J. van Setten, B. Van Troeye, M. J. Verstraete, G. Zérah, and J. W. Zwanziger, *Computer Physics Communications* **248**, 107042 (2020).

[317] “The vienna ab initio simulation package <https://www.vasp.at/>,” .

[318] A. Buccheri, F. Peschel, B. Maurer, M. Voiculescu, D. T. Speckhard, H. Kleine, E. Stephan, M. Kuban, and C. Draxl, *Journal of Open Source Software* **8**, 5148 (2023).

[319] A. H. Larsen, J. J. Mortensen, J. Blomqvist, I. E. Castelli, R. Christensen, M. Dułak, J. Friis, M. N. Groves, B. Hammer, C. Hargus, E. D. Hermes, P. C. Jennings, P. B. Jensen, J. Kermode, J. R. Kitchin, E. L. Kolsbjer, J. Kubal, K. Kaasbjer, S. Lysgaard, J. B. Maronsson, T. Maxson, T. Olsen, L. Pastewka, A. Peterson, C. Rostgaard, J. Schiøtz, O. Schütt, M. Strange, K. S. Thygesen, T. Vegge, L. Vilhelmsen, M. Walter, Z. Zeng, and K. W. Jacobsen, *Journal of Physics: Condensed Matter* **29**, 273002 (2017).

[320] P. Giannozzi, O. Andreussi, T. Brumme, O. Bunau, M. Buongiorno Nardelli, M. Calandra, R. Car, C. Cavazzoni, D. Ceresoli, M. Cococcioni, N. Colonna, I. Carnimeo, A. Dal Corso, S. de Gironcoli, P. Delugas, R. A. DiStasio, A. Ferretti, A. Floris, G. Fratesi, G. Fugallo, R. Gebauer, U. Gerstmann, F. Giustino, T. Gorni, J. Jia, M. Kawamura, H.-Y. Ko, A. Kokalj, E. Küçükbenli, M. Lazzeri, M. Marsili, N. Marzari, F. Mauri, N. L. Nguyen, H.-V. Nguyen, A. Otero-de-la Roza, L. Paulatto, S. Poncé, D. Rocca, R. Sabatini, B. Santra, M. Schlipf, A. P. Seitsonen, A. Smogunov, I. Timrov, T. Thonhauser, P. Umari, N. Vast, X. Wu, and S. Baroni, *Journal of Physics: Condensed Matter* **29**, 465901 (2017).

[321] J. Enkovaara, C. Rostgaard, J. J. Mortensen, J. Chen, M. Dułak, L. Ferrighi, J. Gavnholt, C. Glinsvad, V. Haikola, H. A. Hansen, H. H. Kristoffersen, M. Kuisma, A. H. Larsen, L. Lehtovaara, M. Ljungberg, O. Lopez-Acevedo, P. G. Moses, J. Ojanen, T. Olsen, V. Petzold, N. A. Romero, J. Stausholm-Møller, M. Strange, G. A. Tritsaris, M. Vanin, M. Walter, B. Hammer, H. Häkkinen, G. K. H. Madsen, R. M. Nieminen, J. K. Nørskov, M. Puska, T. T. Rantala, J. Schiøtz, K. S. Thygesen, and K. W. Jacobsen, *J. Phys.: Condens. Matter* **22**, 253202 (2010).

[322] S. Steensen, T. Thakur, M. Dillenz, J. Carlsson, C. Rêgo, E. Flores, H. Hajiyani, F. Hanke, J. Lastra, W. Wenzel, N. Marzari, T. Vegge, G. Pizzi, and I. Castelli, (2025), 10.48550/arXiv.2511.11524.

[323] M. Gjerding, T. Skovhus, A. Rasmussen, F. Bertoldo, A. H. Larsen, J. J. Mortensen, and K. S. Thygesen, *Computational Materials Science* **199**, 110731 (2021).

[324] J. J. Mortensen, M. Gjerding, and K. S. Thygesen, *Journal of Open Source Software* **5**, 1844 (2020).

[325] A. Jain, S. P. Ong, G. Hautier, W. Chen, W. D. Richards, S. Dacek, S. Cholia, D. Gunter, D. Skinner, G. Ceder, and K. A. Persson, *APL Materials* **1** (2013), 10.1063/1.4812323.

[326] S. P. Ong, W. D. Richards, A. Jain, G. Hautier, M. Kocher, S. Cholia, D. Gunter, V. L. Chevrier, K. A. Persson, and G. Ceder, *Computational Materials Science* **68**, 314 (2013).

[327] A. S. Rosen, M. Gallant, J. George, J. Riebesell, H. Sahasrabuddhe, J.-X. Shen, M. Wen, M. L. Evans, G. Petretto, D. Waroquiers, G.-M. Rignanese, K. A. Persson, A. Jain, and A. M. Ganose, *Journal of Open Source Software* **9**, 5995 (2024).

[328] A. M. Ganose, H. Sahasrabuddhe, M. Asta, K. Beck, T. Biswas, A. Bonkowski, J. Bustamante, X. Chen, Y. Chiang, D. C. Chrzan, J. Clary, O. A. Cohen, C. Ertural, M. C. Gallant, J. George, S. Gerits, R. E. A. Goodall, R. D. Guha, G. Hautier, M. Horton, T. J. Inizan, A. D. Kaplan, R. S. Kingsbury, M. C. Kuner, B. Li, X. Linn, M. J. McDermott, R. S. Mohanakrishnan, A. N. Naik, J. B. Neaton, S. M. Parmar, K. A. Persson, G. Petretto, T. A. R. Purcell, F. Ricci, B. Rich, J. Riebesell, G.-M. Rignanese, A. S. Rosen, M. Scheffler, J. Schmidt, J.-X. Shen, A. Sobolev, R. Sundararaman, C. Tezak, V. Trinquet, J. B. Varley, D. Vigil-Fowler, D. Wang, D. Waroquiers, M. Wen, H. Yang, H. Zheng, Z. Zhu, and A. Jain, *Digital Discovery* **4**, 1944 (2025).

[329] S. P. Huber, S. Zoupanos, M. Uhrin, L. Talirz, L. Kahle, R. Häuselmann, D. Gresch, T. Müller, A. V. Yakutovich, C. W. Andersen, F. F. Ramirez, C. S. Adorf, F. Gargiulo, S. Kumbhar, E. Pas-  
saro, C. Johnston, A. Merkys, A. Cepellotti, N. Mounet, N. Marzari, B. Kozinsky, and G. Pizzi, *Scientific Data* **7** (2020), 10.1038/s41597-020-00638-4.

[330] “Excitingtools pypi <https://pypi.org/project/excitingtools/>,” .

[331] R. Golesorkhtabar, P. Pavone, J. Spitaler, P. Puschnig, and C. Draxl, *Computer Physics Communications* **184**, 1861 (2013).

[332] K. Lion, P. Pavone, and C. Draxl, *Physical Review Materials* **6**, 013601 (2022).

[333] D. F. Urban, O. Ambacher, and C. Elsässer, *Phys. Rev. B* **103**, 115204 (2021).

[334] C.-J. Yu, I.-C. Ri, H.-M. Ri, J.-H. Jang, Y.-S. Kim, and U.-G. Jong, *RSC Adv.* **13**, 16012 (2023).

[335] E. Jin, I. S. Lee, D. C. Yang, D. Moon, J. Nam, H. Cho, E. Kang, J. Lee, H.-J. Noh, S. K. Min, and W. Choe, *Nature Communications* **14**, 7938 (2021).

[336] D. T. Speckhard, P. Pavone, S. Bächli, and C. Draxl, “ElaStic2: Automating the calculation of second- and third-order elastic coefficients from first principles,” (2026), in preparation.

[337] A. Togo, K. Shinohara, and I. Tanaka, *Science and Technology of Advanced Materials: Methods* **4**, 2384822 (2024).

[338] C. Møller and M. S. Plesset, *Phys. Rev.* **46**, 618 (1934).

[339] R. J. Bartlett and M. Musiał, *Rev. Mod. Phys.* **79**, 291 (2007).

[340] F. Furche, *The Journal of Chemical Physics* **129**, 114105 (2008).

[341] T. Gruber, K. Liao, T. Tsatsoulis, F. Hummel, and A. Grüneis, *Phys. Rev. X* **8**, 021043 (2018).

[342] A. Grüneis, K. Kacars, A. Gulans, A. Gallo, A. Irmler, F. Hummel, E. Moerman, M. Scheffler, B. Maurer, H. Kleine, C. Draxl, F. Bruneval, M. Giantomassi, and P. R. Nagy, “Cc4s interfaces,” (2026), in preparation.

[343] H. J. Kulik, T. Hammerschmidt, J. Schmidt, S. Botti, M. A. Marques, M. Boley, M. Scheffler, M. Todorović, P. Rinke, C. Oses, *et al.*, *Electronic Structure* **4**, 023004 (2022).

[344] D. Speckhard, T. Bechtel, L. M. Ghiringhelli, M. Kuban, S. Rigamonti, and C. Draxl, *Faraday Discussions* **256**, 483 (2025).

[345] S. Curtarolo, W. Setyawan, S. Wang, J. Xue, K. Yang, R. H. Taylor, L. J. Nelson, G. L. Hart, S. Sanvito, M. Buongiorno-Nardelli, N. Mingo, and O. Levy, *Computational Materials Science* **58**, 227 (2012).

[346] S. Kirklin, J. E. Saal, B. Meredig, A. Thompson, J. W. Doak, M. Aykol, S. Rühl, and C. Wolverton, *npj Computational Materials* **1** (2015), 10.1038/npjcompumats.2015.10.

[347] J. Schmidt, T. F. Cerqueira, A. H. Romero, A. Loew, F. Jäger, H.-C. Wang, S. Botti, and M. A. Marques, *Materials Today Physics* **48**, 101560 (2024).

[348] C. Draxl and M. Scheffler, *MRS Bulletin* **43**, 676 (2018).

[349] M. Scheidgen, L. Himanen, A. N. Ladines, D. Sikter, M. Nakhaee, Á. Fekete, T. Chang, A. Golparvar, J. A. Márquez, S. Brockhauser, S. Brückner, L. M. Ghiringhelli, F. Dietrich, D. Lehmberg, T. Denell, A. Albino, H. Nästrom, S. Shabih, F. Dobener, M. Kühbach, R. Mozumder, J. F. Rudzinski, N. Daelman, J. M. Pizarro, M. Kuban, C. Salazar, P. Ondračka, H.-J. Bungartz, and C. Draxl, *Journal of Open Source Software* **8**, 5388 (2023).

[350] F. Meng, B. Maurer, F. Peschel, S. Selcuk, M. Hybertsen, X. Qu, C. Vorwerk, C. Draxl, J. Vinson, and D. Lu, *Phys. Rev. Mater.* **8**, 013801 (2024).

[351] L. M. Antunes, K. T. Butler, and R. Grau-Crespo, *Nature Communications* **15** (2024), 10.1038/s41467-024-54639-7.

[352] J. Riebesell, R. E. A. Goodall, P. Benner, Y. Chiang, B. Deng, G. Ceder, M. Asta, A. A. Lee, A. Jain, and K. A. Persson, *Nature Machine Intelligence* **7**, 836 (2025).

[353] T. Xie and J. C. Grossman, *Physical Review Letters* **120**, 145301 (2018).

[354] T. Bechtel, D. T. Speckhard, J. Godwin, and C. Draxl, *Chemistry of Materials* **37**, 1358 (2025).

[355] L. M. Ghiringhelli, J. Vybiral, S. V. Levchenko, C. Draxl, and M. Scheffler, *Physical Review Letters* **114**, 105503 (2015).

[356] V. Stanev, C. Oses, A. G. Kusne, E. Rodriguez, J. Paglione, S. Curtarolo, and I. Takeuchi, *npj Computational Materials* **4** (2018), 10.1038/s41524-018-0085-8.

[357] H. Hayashi, A. Seko, and I. Tanaka, *npj Computational Materials* **8** (2022), 10.1038/s41524-022-00899-0.

[358] S. D. Griesemer, B. Baldassarri, R. Zhu, J. Shen, K. Pal, C. W. Park, and C. Wolverton, *Science Advances* **11** (2025), 10.1126/sciadv.adq1431.

[359] P.-P. De Breuck, H.-C. Wang, G.-M. Rignanese, S. Botti, and M. A. L. Marques, *npj Computational Materials* **11** (2025), 10.1038/s41524-025-01881-2.

[360] J. Schmidt, M. R. G. Marques, S. Botti, and M. A. L. Marques, *npj Computational Materials* **5** (2019), 10.1038/s41524-019-0221-0.

[361] K. Choudhary, B. DeCost, C. Chen, A. Jain, F. Tavazza, R. Cohn, C. W. Park, A. Choudhary, A. Agrawal, S. J. L. Billinge, E. Holm, S. P. Ong, and C. Wolverton, *npj Computational Materials* **8** (2022), 10.1038/s41524-022-00734-6.

[362] M. Cheng, C.-L. Fu, R. Okabe, A. Chotrattanapituk, A. Boonkird, N. T. Hung, and M. Li, *Nature Materials* (2026), 10.1038/s41563-025-02403-7.

[363] N. R. Knøsgaard and K. S. Thygesen, *Nature Communications* **13** (2022), 10.1038/s41467-022-28122-0.

[364] M. Kuban, S. Rigamonti, M. Scheidgen, and C. Draxl, *Scientific Data* **9** (2022), 10.1038/s41597-022-01754-z.

[365] M. Kuban, Š. Gabaj, W. Aggoune, C. Vona, S. Rigamonti, and C. Draxl, *MRS Bulletin* **47**, 991 (2022).

[366] D. T. Speckhard, C. Carbogno, L. M. Ghiringhelli, S. Lubeck, M. Scheffler, and C. Draxl, *Physical Review Materials* **9**, 013801 (2025).

[367] L. M. Ghiringhelli, C. Carbogno, S. Levchenko, F. Mohamed, G. Huhs, M. Lüders, M. Oliveira, and M. Scheffler, *npj Computational Materials* **3** (2017), 10.1038/s41524-017-0048-5.

[368] P. Kraus, *Journal of Chemical Theory and Computation* **17**, 5651 (2021).

[369] R. Ouyang, S. Curtarolo, E. Ahmetcik, M. Scheffler, and L. M. Ghiringhelli, *Physical Review Materials* **2**, 083802 (2018).

[370] T. A. Purcell, M. Scheffler, and L. M. Ghiringhelli, *The Journal of Chemical Physics* **159** (2023).

[371] D. Speckhard, *Uncertainty quantification and  $\Delta$ -learning via statistical and geometric learning with density functional theory data*, Ph.D. thesis, Humboldt-Universität zu Berlin (2026), (in preparation).

[372] L. Pardini, “Nomad repository entry,” (2018).

[373] O. Isayev, D. Fourches, E. N. Muratov, C. Osse, K. Rasch, A. Tropsha, and S. Curtarolo, *Chemistry of Materials* **27**, 735 (2015).

[374] M. Kuban, S. Rigamonti, and C. Draxl, *Digital Discovery* **3**, 2448 (2024).

[375] P. Willett, J. M. Barnard, and G. M. Downs, *Journal of Chemical Information and Computer Sciences* **38**, 983 (1998).

[376] J. Sanchez, F. Ducastelle, and D. Gratias, *Physica A* **128**, 334 (1984).

[377] J. W. D. Connolly and A. R. Williams, *Phys. Rev. B* **27**, 5169 (1983).

[378] M. Troppenz, S. Rigamonti, J. O. Sofo, and C. Draxl, *Phys. Rev. Lett.* **130**, 166402 (2023).

[379] A. Stroth, C. Draxl, and S. Rigamonti, *Phys. Rev. Res.* **7**, 033091 (2025).

[380] A. Kokalj, *Journal of Molecular Graphics and Modelling* **17**, 176 (1999).

[381] M. Kawamura, *Computer Physics Communications* **239** (2019), 10.1016/j.cpc.2019.01.017.

[382] P. T. Inc., “Collaborative data science,” (2015).

[383] J. Stutz, M. Kuban, P. Pavone, and C. Draxl, “Fsvisual,” (2026), (in preparation).